

The Effect of Stability Conditions on Offshore Wind Farm Wakes – an Investigation through Mesoscale Modelling

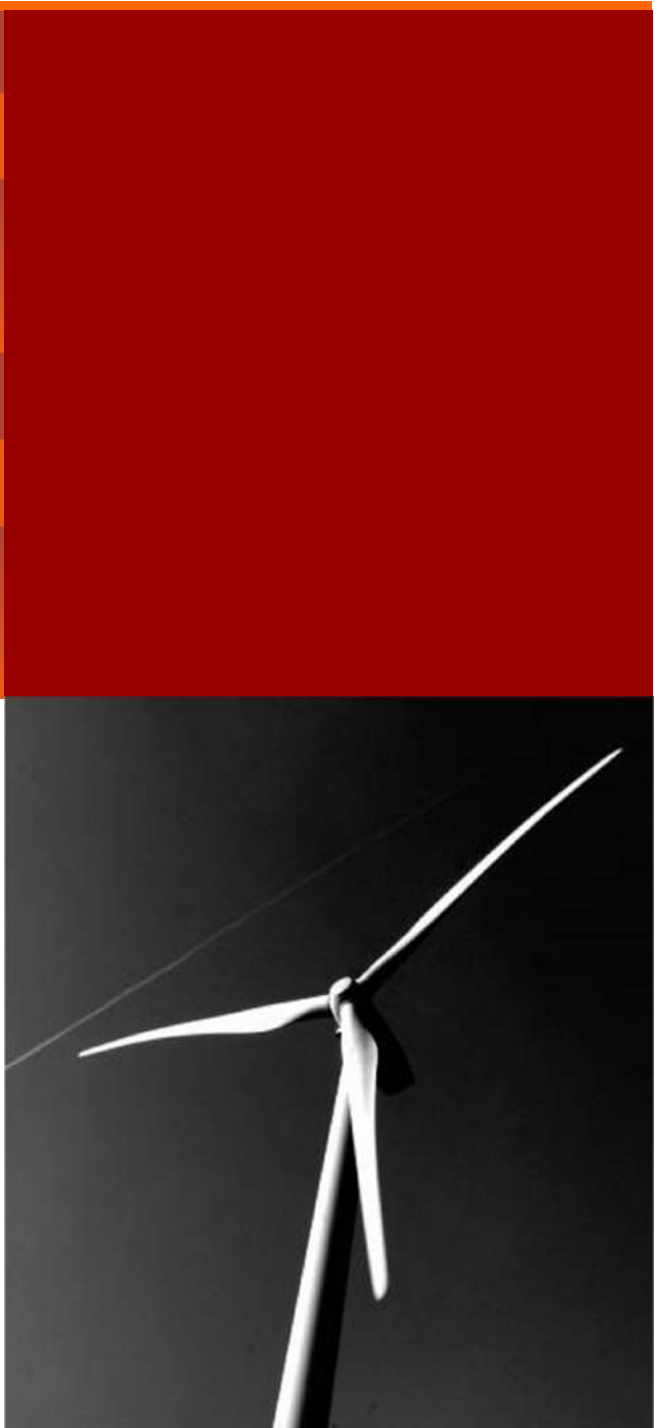
Department of
Wind Energy
Master Report

Adit Nand Kishore

DTU Wind Energy-M-0258

January 2019

DTU Wind Energy
Department of Wind Energy



Author: Adit Nand Kishore

Title: The Effect of Stability Conditions on Offshore Wind Farm Wakes –
an Investigation through Mesoscale Modelling

DTU Wind Energy-M-02588

January 2019

Project period:

August 2018 – January 2019

ECTS: 30

Education: Master of Science

Supervisors:

Xiaoli Guo Larsen

Patrick Volker

DTU Wind Energy

Remarks:

This report is submitted as partial
fulfillment of the requirements for
graduation in the above education at the
Technical University of Denmark.

DTU Wind Energy is a department of the Technical University of Denmark with a unique integration of research, education, innovation and public/private sector consulting in the field of wind energy. Our activities develop new opportunities and technology for the global and Danish exploitation of wind energy. Research focuses on key technical-scientific fields, which are central for the development, innovation and use of wind energy and provides the basis for advanced education at the education.

We have more than 240 staff members of which approximately 60 are PhD students. Research is conducted within nine research programmes organized into three main topics: Wind energy systems, Wind turbine technology and Basics for wind energy.

Technical University of Denmark

Department of Wind Energy

Frederiksborgvej 399

2800 Kgs. Lyngby

Denmark

www.vindenergi.dtu.dk

Acknowledgements

Many people have contributed to this master thesis through knowledge, data, guidance, proof reading, and moral support.

At Risø: Firstly, I would like to express my gratitude to my supervisors Xiaoli Guo Larsén and Patrick Volker for their constant guidance, knowledge, and time. Xiaoli for continuously encouraging me to achieve more.

Andrea N. Hahmann for her time and help with issues encountered while running WRF simulations, Bjarke Tobias Olsen, Marc Imberger, Neil Davis, Paul van der Laan, Tobias Torben Ahsbahs, and Tuhfe Göçmen.

I would like to thank the EUDP/ForskEL OffshoreWake project (64017-0017/12521), under which this thesis is performed. To Mr. Samuel Hawkins from Vattenfall for providing the wind farm measurement data for SandBank and DanTysk.

To Mr. Markus Kreklau for providing the access to the FINO3 data base provided by BMWi (Bundesministerium für Wirtschaft und Energie) and PTJ (Projektträger Jülich) as the owner of FINO data base.

Nieves Burillo Esteban at Siemens and Niels Gylling Mortensen at Risø for providing turbine power curves.

At ConWX: All my colleagues for their help and support during this thesis. Specially Erik Østergaard Madsen, Iben Holfort Voxen, and Mares Radomir for their constant moral support, encouragement, and thesis-related thought provoking questions.

To my parents and sister for their unconditional support and understanding, and all my friends here in Denmark, India, and the USA.

Many thanks to all of you.

Abstract

YET TO DO

Contents

Acknowledgements	iii
Abstract	iv
List of Figures	vii
List of Tables	xii
Nomenclature	xiii
1 Introduction	1
1.1 Background Information	1
1.2 Motivation and Objectives	1
1.3 Literature Review	3
2 Methodology	5
2.1 Wind Farms and Meteorological (MET) Mast	5
2.2 Satellite Synthetic Aperture Radar (SAR) Images	6
2.3 Theoretical Background - Stability	9
3 Weather Research and Forecast (WRF) Model	12
3.1 WRF Environment	12
3.2 Wind Farm Parametrisation in WRF	13
3.2.1 Fitch Scheme	14
3.2.2 Explicit Wake Parametrisation (EWP) Scheme	16
3.3 WRF Model Setup in the Current Study	17
3.4 Flow Region Affected by Wind Farms in WRF	19
4 Analysis of Measurements	21
4.1 Wind Farm Measurements	21
4.2 Fino3 Meteorological (MET) Mast	23
5 Simulation Results and Analysis	28
5.1 Modelled Wind Speed Field vs. Satellite Images	29
5.1.1 EWP Scheme	30
5.1.2 Fitch Scheme	33
5.1.3 Summary and Conclusions	35
5.2 Wind Speed, Wake and TKE Field	36
5.2.1 EWP scheme	38
5.2.2 Fitch scheme	50
5.2.3 Summary	61
5.3 Effect of Stability on Wakes	62
5.4 Effect of Stability on Power Production	72

6 Discussion and Conclusions	82
7 Future Work	85
A Wind Speed, Wake and TKE field for Cases 4 and 5	86
A.1 EWP scheme	86
A.1.1 Case 4	86
A.1.2 Case 5	90
A.2 Fitch scheme	94
A.2.1 Case 4	94
A.2.2 Case 5	98
B Spatial Distribution of Temperature Difference	102
References	104

List of Figures

2.1	Position of SandBank (WF1), DanTysk (WF2), and Fino3 MET mast. <i>Source: 4coffshore.com/</i>	6
2.2	2017-05-11 17:17:35 - Position of SandBank (WF1) in red, DanTysk (WF2) in black.	7
2.3	2018-04-24 17:17:55 - Position of SandBank (WF1) in red, DanTysk (WF2) in black.	8
2.4	2018-04-27 05:40:26 - Position of SandBank (WF1) in red, DanTysk (WF2) in black.	8
3.1	WRF model system overview, a modified version of the flowchart in [WRF_modelling_system_overview].	13
3.2	Vertical cross section of the mean difference over the wind farm and wake region of TKE as taken from Fitch et al. (2012) [12]	15
3.3	WRF model domain configurations and terrain elevation (m) maps. (a): 9 km × 9 km domain (D1), (b): 3 km × 3 km domain (D2), and (c): 1 km × 1 km domain (D3). The inner lines show the positions of the nested-domains.	18
4.1	Median power curve from turbine measured power and wind speed in different colours against the manufacturer power curve indicated in black for WF1 (a) and WF2 (b).	22
4.2	Wind rose (% frequency along circular axes) from Fino3 MET mast data between 2013-01-01 and 2018-08-31.	23
4.3	Wind rose (% frequency along circular axes) from Fino3 wind speed measurements at 90 m height for (a) pre-construction: 2013-01-01 up to 2015-01-01, and (b) post-construction: 2015-01-01 up to 2018-09-01.	25
4.4	90 m Wind speed histograms with normalised frequencies for the Pre-construction: 2013-01-01 up to 2015-01-01, and Post-construction: 2015-01-01 up to 2018-09-01.	26
4.5	Bulk Richardson Number distribution at Fino3 between 2014-09-01 00:10 and 2018-05-31 23:30	27
5.1	Case 3 (2017-05-11 17:20): WRF-EWP wind speed field (a); Variation of WRF-EWP wind direction with time at an upstream undisturbed location - both at 10m above surface.	30
5.2	Case 4 (2018-04-24 17:20): WRF-EWP wind speed field (a); Variation of WRF-EWP wind direction with time at an upstream undisturbed location - both at 10m above surface.	31
5.3	Case 5 (2018-04-27 05:40): WRF-EWP wind speed field (a); Variation of WRF-EWP wind direction with time at an upstream undisturbed location - both at 10m above surface.	32

5.4	Case 3 (2017-05-11 17:20): WRF-Fitch wind speed field (a); Variation of WRF-EWP wind direction with time at an upstream undisturbed location - both at 10m above surface.	33
5.5	Case 4 (2018-04-24 17:20): WRF-Fitch wind speed field (a); Variation of WRF-EWP wind direction with time at an upstream undisturbed location - both at 10m above surface.	34
5.6	Case 5 (2018-04-27 05:40): WRF-Fitch wind speed field (a); Variation of WRF-EWP wind direction with time at an upstream undisturbed location - both at 10m above surface.	35
5.7	Analysis Points used to analyse disturbed wind speed and TKE flow fields, and obtain free stream parameter values.	36
5.8	Case 1 (2016-09-13 16:20) : WRF-EWP modelled wind speeds at 90 m with wind farms.	38
5.9	Case 1: WRF-EWP modelled wind speed difference at 90 m - with and without wind farms.	39
5.10	Case 1: Profile of WRF-EWP modelled wind speed difference with and without wind farms along wake length points of WF1 (a) and WF2 (b).	40
5.11	Case 1: Profile of WRF-EWP modelled TKE difference with and without wind farms along wake length points of WF1 (a) and WF2 (b).	41
5.12	Case 2 (2016-11-02 08:20) : WRF-EWP modelled wind speeds at 90 m with wind farms.	42
5.13	Case 2: WRF-EWP modelled wind speed difference at 90 m - with and without wind farms.	43
5.14	Case 2: Profile of WRF-EWP modelled wind speed difference with and without wind farms along wake length points of WF1 (a) and WF2 (b).	44
5.15	Case 2: Profile of WRF-EWP modelled TKE difference with and without wind farms along wake length points of WF1 (a) and WF2 (b).	45
5.16	Case 3 (2017-11-05 17:20) : Wind speeds at 90 m with wind farms.	46
5.17	Case 3: Wind speed difference at 90 m - with and without wind farms.	46
5.18	Case 3: Profile of wind speed difference with and without wind farms along wake length points of WF1 (a) and WF2 (b).	47
5.19	Case 3: Profile of TKE difference with and without wind farms along wake length points of WF1 (a) and WF2 (b).	48
5.20	Case 1 (2016-09-13 16:20) : WRF-Fitch modelled wind speeds at 90 m with wind farms.	50
5.21	Case 1: WRF-Fitch modelled wind speeds difference at 90 m - with and without wind farms.	51
5.22	Case 1: Profile of WRF-Fitch modelled wind speed difference with and without wind farms along wake length points of WF1 (a) and WF2 (b).	52
5.23	Case 1: Profile of WRF-Fitch modelled TKE difference with and without wind farms along wake length points of WF1 (a) and WF2 (b).	53
5.24	Case 2 (2016-11-02 08:20) : WRF-Fitch modelled wind speeds at 90 m with wind farms.	54
5.25	Case 2: WRF-Fitch modelled wind speeds difference at 90 m - with and without wind farms.	55

5.26 Case 2: Profile of WRF-Fitch modelled wind speed difference with and without wind farms along wake length points of WF1 (a) and WF2 (b).	56
5.27 Case 2: Profile of WRF-Fitch modelled TKE difference with and without wind farms along wake length points of WF1 (a) and WF2 (b).	57
5.28 Case 3 (2017-11-05 17:20) : WRF-Fitch modelled wind speeds at 90 m with wind farms.	58
5.29 Case 3: WRF-Fitch modelled wind speed difference at 90 m - with and without wind farms.	58
5.30 Case 3: Profile of WRF-Fitch modelled wind speed difference with and without wind farms along wake length points of WF1 (a) and WF2 (b).	59
5.31 Case 3: Profile of WRF-Fitch modelled TKE difference with and without wind farms along wake length points of WF1 (a) and WF2 (b).	60
5.32 Variation of stability conditions with time for the EWP and Fitch scheme from the five simulations.	64
5.33 Wind rose of the total 720 instances distributed based on the wind direction for the EWP scheme (a) and Fitch scheme (b) from the five simulations.	65
5.34 Mean wake lengths [km] of WF1 and WF2 as a function of wind speed intervals for EWP scheme (a) and Fitch scheme (b).	66
5.35 Mean wake lengths [km] of WF1 and WF2 as a function of wind direction bins for EWP scheme (a) and Fitch scheme (b).	67
5.36 Stability rose of the total 720 instances distributed based on the wind direction for the EWP scheme (a) and Fitch scheme (b) from the five simulations.	68
5.37 Wind speed distributions of the total 720 instances distributed based on the stability conditions for the EWP scheme (a) and Fitch scheme (b).	69
5.38 Mean wake lengths [km] of WF1 and WF2 as a function of atmospheric stability condition for EWP (a) and Fitch (b) from the five simulations.	70
5.39 Total power losses (MW) as a function of atmospheric stability condition, and corresponding frequency of occurrences for EWP (a) and Fitch (b).	72
5.40 Total power losses (MW) as a function of wind direction bins, and corresponding frequency of occurrences for EWP (a) and Fitch (b).	74
5.41 Comparison of measured and WRF-modelled power (MW) using EWP and Fitch schemes for simulation 3 (a), simulation 4 (b), and simulation 5 (c).	75
5.42 10-min Power Losses [MW] due to the wake interaction as seen in WRF using the Fitch and EWP scheme as a function of corresponding atmospheric stability, wind direction, and wind speed for the five simulations.	77
5.43 Comparison of 10-min measured and WRF-modelled power (MW) using EWP and Fitch schemes for the 9 day simulation as a function of corresponding atmospheric stability, wind direction, and wind speed for the five simulations.	78

5.44 Bias between 10-min measured and WRF-modelled power (MW) using EWP and Fitch schemes for the 9 day simulation as a function of corresponding atmospheric stability, wind direction, and wind speed for the five simulations.	80
A.1 Case 4 (2018-04-24 17:20) : WRF-EWP modelled wind speeds at 90 m with wind farms.	86
A.2 Case 4: WRF-EWP modelled wind speed difference at 90 m - with and without wind farms.	87
A.3 Case 4: Profile of WRF-EWP modelled wind speed difference with and without wind farms along wake length points of WF1 (a) and WF2 (b).	88
A.4 Case 4: Profile of WRF-EWP modelled TKE difference with and without wind farms along wake length points of WF1 (a) and WF2 (b).	89
A.5 Case 5 (2018-04-27 05:40) : WRF-EWP modelled wind speeds at 90 m with wind farms.	90
A.6 Case 5: WRF-EWP modelled wind speed difference at 90 m - with and without wind farms.	91
A.7 Case 5: Profile of WRF-EWP modelled wind speed difference with and without wind farms along wake length points of WF1 (a) and WF2 (b).	92
A.8 Case 5: Profile of WRF-EWP modelled TKE difference with and without wind farms along wake length points of WF1 (a) and WF2 (b).	93
A.9 Case 4 (2018-04-24 17:20) : WRF-Fitch modelled wind speeds at 90 m with wind farms.	94
A.10 Case 4: WRF-Fitch modelled wind speeds difference at 90 m - with and without wind farms.	95
A.11 Case 4: Profile of WRF-Fitch modelled wind speed difference with and without wind farms along wake length points of WF1 (a) and WF2 (b).	96
A.12 Case 4: Profile of WRF-Fitch modelled TKE difference with and without wind farms along wake length points of WF1 (a) and WF2 (b).	97
A.13 Case 5 (2018-04-27 05:40) : WRF-Fitch modelled wind speeds at 90 m with wind farms.	98
A.14 Case 5: WRF-Fitch modelled wind speed difference at 90 m - with and without wind farms.	98
A.15 Case 5: Profile of WRF-Fitch modelled wind speed difference with and without wind farms along wake length points of WF1 (a) and WF2 (b).	99
A.16 Case 5: Profile of WRF-Fitch modelled TKE difference with and without wind farms along wake length points of WF1 (a) and WF2 (b).	101
B.1 Case 1 (2016-09-13 16:20): Temperature difference between 20 m height and sea surface.	102
B.2 Case 2 (2016-11-02 08:20): Temperature difference between 20 m height and sea surface.	102
B.3 Case 3 (2017-05-11 17:20): Temperature difference between 20 m height and sea surface.	103

B.4 Case 4 (2018-04-24 17:20): Temperature difference between 20 m height and sea surface.	103
B.5 Case 5 (2018-04-27 05:40): Temperature difference between 20 m height and sea surface.	103

List of Tables

2.1	Information about identified wind farms	6
2.2	Atmospheric stratification or stability classes according to intervals of the Obukhov length.	11
4.1	Mean wind speeds (ms^{-1}) for the total period and the three identified phases.	24
5.1	Identified cases to be modelled, along with the case name with which they are referred to hereafter.	28
5.2	Initialisation time, run hours, end of simulation, and spin-up hours for the identified cases.	29
5.3	WRF-EWP modelled upstream stability values, and total wake length for WF2 and WF1 using a wake-length threshold of 10%.	63
5.4	WRF-Fitch modelled upstream stability values, and total wake length for WF2 and WF1 using a wake-length threshold of 10%.	63
5.5	Stability distribution (Frequency %) over simulations 1, 2, 3, 4, and 5 combined from the EWP and Fitch scheme respectively.	64
5.6	Average bias of 10-min measured and modelled power (MW) over simulations 3, 4, and 5 using the WRF-EWP and WRF-Fitch schemes.	76
5.7	MAE of 10-min measured and modelled power (MW) over simulations 3, 4, and 5 using the WRF-EWP and WRF-Fitch schemes.	76
5.8	RMSE of 10-min measured and modelled power (MW) over simulations 3, 4, and 5 using the WRF-EWP and WRF-Fitch schemes.	76
5.9	Average bias, MAE, and RMSE of 10-min measured and modelled power (MW) over the 9-day simulation using the WRF-EWP and WRF-Fitch schemes.	79
5.10	Average bias and MAE of 10-min measured and modelled power (MW) for each day over the 9-day simulation from 2018-04-13 to up to 2018-04-23 using the WRF-EWP and WRF-Fitch schemes.	81

Nomenclature

YET TO DO LAH	List Abbreviations Here
WSF	What (it) Stands For

Chapter 1

Introduction

1.1 Background Information

In the last decade, there has been a significant increase in the global installed wind power capacity, with more than a threefold increase in the global cumulative offshore wind capacity from 5.4 GW in 2012 to 18.8 GW in 2017 [1]. In Europe alone, the capacity addition of both onshore and offshore wind power in 2017 stood at 16.8 GW, with offshore wind power accounting for 3.15 GW of capacity addition [2].

Wind power capacity in the North Sea accounts for more than 70% of the offshore wind power capacity in Europe, followed by the Irish Sea, Baltic Sea, and the Atlantic Ocean, with a lot of wind farms being grouped closer together in clusters [1]. With global installed offshore wind power capacity forecasts for 2030 standing at a staggering 120 GW, and falling fixed-bottom offshore wind power LCOE, it is likely that more offshore wind farms will be installed in clusters - utilizing the wind resources of a region optimally, and reducing extra costs of grid connection infrastructure [1] [3].

1.2 Motivation and Objectives

Extraction of kinetic energy from wind by turbine blades produces wind power, creating wakes - regions downstream of wind turbines characterized by reduced wind speed and an increased turbulence intensity. The flow due to grouping of multiple turbines in wind farms becomes more complex, due the interaction of wakes between turbines, thereby affecting the overall performance of wind turbines due to reduced wind speeds and increased turbulence [4] [5] [6].

Studies suggest that wind farms also affect the turbulence transport in the atmospheric boundary layer (ABL) [7] [8] [9] [10] [11] [12]. The presence of gravity waves in wind farm regions under certain atmospheric conditions is suggested have an affect on wind farm performance [13] [14] [15]. Studies using satellite images show that the velocity deficit can extend long enough to affect a downstream wind farm [16] [17]. All of these are ways in which the wind farms and the atmosphere interact and affect each other.

Due to this interaction between wind farms and the atmosphere, understanding the impact of wind farms on each other and the local wind climate becomes imperative - to accurately assess the expected energy production, to maximize turbine lifetime

during the operational lifetime of the wind farm, and to assist in development of optimal wind farm clusters to utilize optimally the wind resources of the most convenient areas.

Turbine or local wake models (such as the Park Wake Model based on the N.O.Jensen model) to calculate wind speed reduction due to turbine wakes, and LES simulations over a domain containing several wind farms would be expensive [18] [19] [20] [21] [22]. There aren't many reports quantifying the effect of wind farms on one another and the local wind climate.

Numerical Weather Prediction (NWP) or mesoscale models such as Weather Research and Forecasting (WRF) are run with much coarser spatial resolutions as compared to local wake models, but are expected to provide realistic large scale flow, which is relevant for wind farm wake interaction studies [23] [24]. Operational forecasting use NWP's, but normally do not include the physical effect of wind turbines directly, which may cause discrepancies in realized values of wind speed/power forecasts, future wind resource assessments, operation and maintenance (O&M) service window forecasts, etc. This is because the grid resolution of NWP models are large and do not capture wind farm effects occurring at smaller scales. Hence, the effects of wind turbines are parametrised in WRF using two schemes:

1. (Local) Actuator disk model with additional TKE source term: **Fitch scheme**, which is included in the wind farm parametrisation option in WRF [12].
2. Non-local wake parametrisation: **Explicit Wake Parametrisation (EWP) scheme** [11].

This project aims to model real cases using the two parametrisation schemes in Advanced Research - WRF (AR-WRF v3.8.1). The modelling is performed using two wind farms relatively close to each other. The identified wind farms are Sandbank and DanTysk, or also as hereafter referred to as WF1 and WF2 respectively, and are located in the North Sea. Special cases where wakes are present and represent different stability conditions are identified and modelled - three from satellite data and two from meteorological (MET) mast measurements. These modelled results are analysed to answer the following research questions:

1. How well do the modelled wind fields and wakes obtained using the two wind farm parametrisation schemes in WRF compare with the satellite images?
2. What is the quantitative effect of atmospheric stability on the wakes as seen in WRF? How do they differ between the Fitch scheme and EWP scheme? Are characteristics of the wake regions in agreement with other studies?
3. Similarly, what is the effect of atmospheric stability on power production of the two wind farms as seen in WRF? How does the modelled power production compare to measurements?
4. How does the behaviour of the two schemes differ from the analysis of the simulations?

A study of the effect of stability on offshore wind farm wakes for the two selected wind farms using both parametrisation schemes in WRF (v3.8.1) in a real case setup has not been found in previous literature.

1.3 Literature Review

To study and quantify wakes for a wind farm using measurements, setting up multiple MET towers offshore to study the velocity deficit for different wind directions at different distances can be expensive. The wakes from wind farms behave differently, based on the turbine types, the layout of the wind farm, the geographical conditions, etc. Hence, generalizing the effect of wakes from wind farms can be complicated. Frandsen et al. [25] studied the wakes with measurements at a fixed and relatively short distances of up to 1.4 km from the turbines. Volker et al. [11] modelled the Horns Rev I wind farm in an idealised WRF simulation using the two wind farm parametrisation schemes, and validated the wind speeds downstream of Horns Rev I against two MET mast measurements at 2 km and 6 km from the turbines.

Not all wind farms have such placement of MET masts to study downstream flow in different directions and at varying distances. Therefore, studies have also made use of satellite Synthetic Aperture Radar (SAR) images and data, to identify and study wakes, and also to quantify wind resources [26]. Hasager et al. [16] found velocity deficits of 2% up to 20 km downstream of the Horns Rev I wind farm for near-neutral stable atmospheric conditions, and up to 5 km for unstable conditions from case studies using SAR wind speed maps. Further, these results were found to be consistent with results from wake models and in situ measurements.

A study by Hansen et al. [27] found a general tendency in the relationship between power deficits, wind speed, turbulence, and stability conditions for the Horns Rev 1 wind farm based on measurements, wherein Bulk-Richardson was used to classify the stability conditions. In another study by Wagner et al. [28], wind speed shear (which is affected by the stability condition) was found to have an impact on the power output of a wind turbine using aerodynamics simulations.

Platis et al. [29] made use of the research aircraft Dornier DO-128 to collect in situ measurements up to 45 km length downstream of the wind farm cluster comprising of Amrumbank West, Nordsee Ost and Meerwind Süd/Ost [29]. Using these in situ measurements, the zone of reduced wind speed behind a wind farm cluster was found to extend at least 45 km with a maximum velocity deficit of 3 ms^{-1} and 1 ms^{-1} at 5 km and 45 km downstream respectively. It was found that the wind speed deficits downstream of offshore wind farms are larger in stable conditions than in unstable conditions, and similarly the length of wakes are longer under stable conditions than in unstable conditions. This is also the first study to provide in situ measurements confirming the existence of farm wakes extending at least 45 km downstream of wind farms, which also confirms the ability of SAR satellite images and numerical simulations in WRF using the Fitch parametrisation scheme in capturing the wind fields of wind farm wakes.

Djath et al. [30] quantified and characterized wakes based on wind speed, wind direction, and atmospheric stability, using SAR images for a wind farm in a cluster the North Sea.

Lundquist et al. [31] evaluated the modelled power production for the CWEX-13 onshore wind farm in WRF in comparison with the actual power-production measurements over a 4-day period. It also found the modelled power to be in better agreement with the power-production measurements for a finer vertical resolution of 12 m as compared to 22 m. The use of the Fitch scheme resulted in more accurate power prediction as compared to simulations without the wind farm scheme, which over-predicted power production. Volker et al. [11] found the performance of the EWP scheme to be independent of vertical resolution, and the velocity deficits at hub height were similar when using 40 vertical levels and 80 vertical levels in an idealised WRF setup. As the flow in offshore conditions is expected to not be as complex as onshore, a coarser vertical resolution is used in this project.

Recently, Lunquist et al [32] quantified the effect of power losses due to wake interaction between two onshore wind farms in Texas, USA, which resulted in economic losses of several million dollars over a period of six years. This study made use of the Fitch parametrisation scheme in WRF, with spacing between some turbines of the two wind farms being lesser than 300 m. Wind speed deficits of 0.5 ms^{-1} were found at 50 km downstream under stable conditions. They also quantified hourly total power losses as a function of wind speed, wind direction, and sensible heat flux - with losses being highest in sectors representing flow-interaction between the wind farms, and under stable conditions.

Since SAR images are limited in sample by availability only when there is a satellite pass over the wind farms under study, SAR images have only been used as a starting point - to identify the initial cases with visible wakes to be modelled in WRF with the wind farm parametrisation schemes to qualitatively assess how well the simulations capture the wind field patterns. After simulating the initial cases in WRF, measurements from the offshore MET mast, Fino3 have been used to guide to cases of different stabilities to be modelled in WRF. The Fino3 MET mast is located on the outer boundary of the WF2 wind farm, but between WF1 and WF2, hence the measurements are affected by both the wind farms. However, the cases from Fino3 data are identified based on stability conditions, wind speed and wind direction criteria. On successful simulation of these cases, a qualitative analysis of the modelled wind field is carried out. Further, these simulations are analysed in greater detail to understand and quantify the effect of stability on the structure of velocity deficit regions or wakes.

Chapter 2

Methodology

This chapter provides a description of the methods used within the scope of this thesis. Chapter 2.1 provides an overview of the wind farms selected for this project, and the meteorological (MET) mast tower data close to the wind farms. Chapter 2.2 describes the basis on which the cases used within this thesis are identified from satellite imagery. Chapter 2.3 gives the theoretical background of stability, and how stability is estimated and the classification method used in this project.

2.1 Wind Farms and Meteorological (MET) Mast

Two wind farms in the North Sea are identified for this project:

1. SandBank - WF1
2. DanTysk - WF2

The two wind farms are chosen for this project, as no such previous study has been carried out with them based on the literature found, and availing wind farm data would be relatively easier as this Master thesis is a part the project "OffshoreWake" which is a collaboration between Vattenfall and DTU Wind Energy - which aims to understand how offshore wind farms should be positioned so that they do not steal the wind from each other due to the wake or shadow effects from one wind farm to another.

Table 2.1 shows details of the two wind farms¹.

¹Source: 4coffshore.com

Table 2.1: Information about identified wind farms

	WF1	WF2
Owner	Vattenfall	Vattenfall
Number of wind turbines	72	80
Wind turbine model	Siemens SWT-4.0-130	Siemens SWT-3.6-120
Wind Turbine Capacity	4.0 MW	3.6 MW
Wind Turbine Hub Height	94.75 m	88 m
Wind Turbine Rotor Diameter	130 m	120 m
Total Turbine Height	159.8 m	148 m
Project capacity	288 MW	288 MW
Centre latitude	55.2°	55.138°
Centre longitude	6.852°	7.20°
Distance between wind farm centres	$\approx 23 \text{ km}$	

Measurements from the Fino3 Meteorological (MET) mast² have been used to identify additional cases of different stabilities to be modelled. The Fino3 MET mast is located on the outer part of WF2, but between WF2 and WF1. Figure 2.1 shows the positions of the wind farms WF1 and WF2, and the Fino3 MET mast.



Figure 2.1: Position of SandBank (WF1), DanTysk (WF2), and Fino3 MET mast. Source: 4coffshore.com/

2.2 Satellite Synthetic Aperture Radar (SAR) Images

SAR is an active microwave sensor that transmits a signal directed towards a target area . It receives the back-scattered signal per unit area or normalized radar cross section off of the ocean surface, which is sensitive to small-scale ocean waves. The wind over the ocean surface causes centimetre-scale waves to form on the ocean surface, off of which these signals are back-scattered. The wind speed at 10 m height

²Provided by BMWi (Bundesministerium für Wirtschaft und Energie) and PTJ (Projektträger Jülich)

is then retrieved from these SAR observations using an empirical geophysical model function.

The extensive use of satellite SAR images in the study of flow around wind farms has already been highlighted in Section 1.2. SAR images and data have been validated, and hence the use of such satellite SAR wind field images developed at DTU Wind Energy have been used in this study [33] [34]. From the catalogue of limited Satellite SAR wind field images available for the region of the North Sea where WF1 and WF2 are located, the following three SAR images have been identified to simulate as the initial cases in WRF. These SAR images have been selected because of visible wakes³ in the wind fields of WF1 and WF2, which possibly indicate neutral to stable and stable atmospheric conditions. On successfully simulating these time-stamps in WRF using the two wind farm parametrisation schemes (EWP and Fitch), a qualitative analysis of the wind field is carried out.

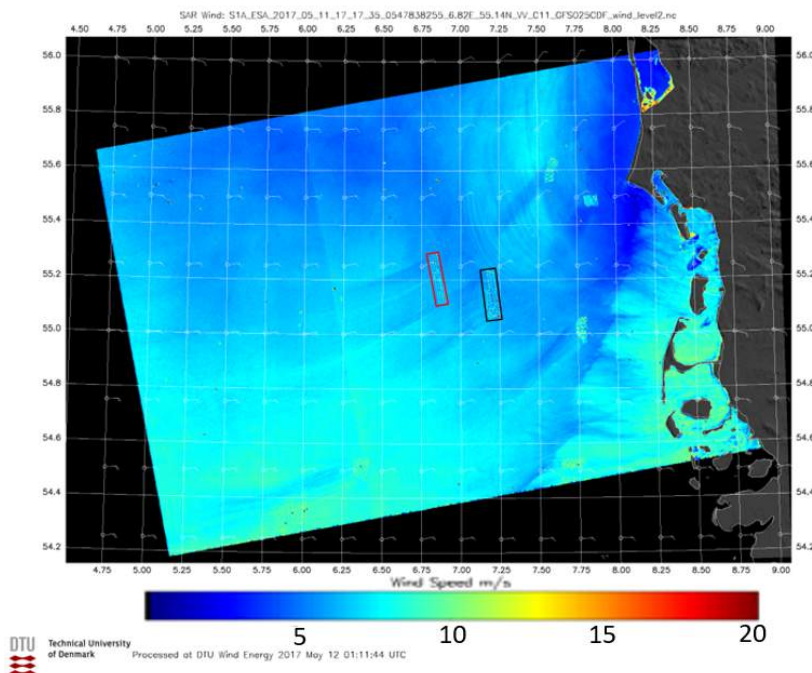


Figure 2.2: 2017-05-11 17:17:35 - Position of SandBank (WF1) in red, DanTysk (WF2) in black.

³If the wakes are not visible in the printed version due to printing errors, I request you to refer to the electronic copy or

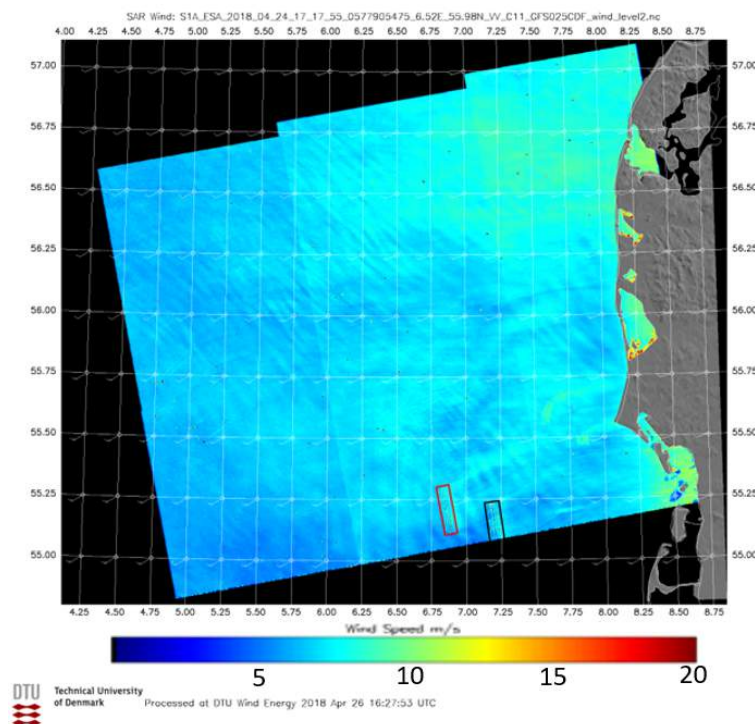


Figure 2.3: 2018-04-24 17:17:55 - Position of SandBank (WF1) in red, DanTysk (WF2) in black.

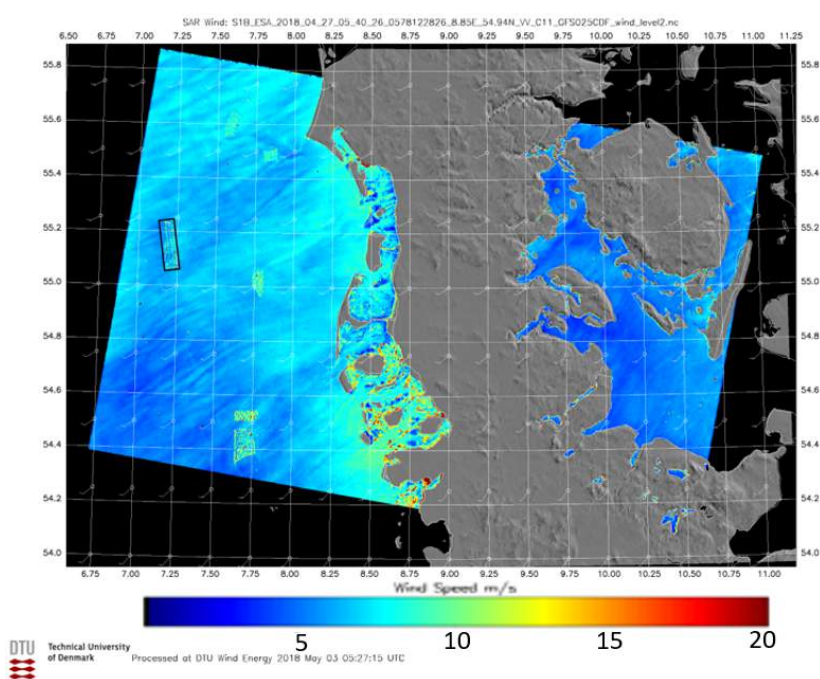


Figure 2.4: 2018-04-27 05:40:26 - Position of SandBank (WF1) in red, DanTysk (WF2) in black.

2.3 Theoretical Background - Stability

The stratification of the atmosphere has a significant influence on the wind shear. Under stable conditions the wind shear is higher due to lack of mixing in the vertical layers in the atmosphere and wind shear is lower in unstable conditions [35]. These stratification conditions of the atmosphere have a direct impact on the power production and structural properties of wind turbines.

Under favourable stratification conditions, increased turbulence has a direct effect on the structure of wind turbines, which can increase maintenance and repair costs, but also decrease turbine lifetime. Barthelmie et al. [36] found that between 8 ms^{-1} - 9 ms^{-1} , wind farm efficiency in the Nysted wind farm in the Baltic Sea were around 7.2% lower in stable conditions than in neutral conditions, and 1% higher in unstable conditions than in neutral conditions. Studies have shown that power production losses are higher under stable conditions when compared to unstable conditions, as convection in the vertical layers under stable conditions is suppressed. Hence, winds that have been slowed down due to the presence of a turbine do not recover as fast as in unstable conditions, due to lower mixing. This is also the reason that wakes with a longer fetch are observed under stable conditions and near-neutral stable conditions, and wakes with a shorter fetch are encountered in unstable conditions [30].

The measurement of parameters to obtain the state of atmospheric stratification is rather complicated and expensive, more-so offshore. In this case study, the estimation of atmospheric stratification is further complicated due to the position of the Fino3 MET mast being located between the two wind farms. With measurements being influenced by the flow between the wind farms, directly obtaining free stream measurements from Fino3 in certain wind directions is not possible. Roy et al. [37] found that with a larger turbulence generated in the wake behind wind turbine rotors, a stronger impact on near-surface air temperature is more likely, which could affect the stability characterisation. Pena et al. [38] validated bulk estimate predictions from NWP models against observations from sonic and bulk estimates, and also found that bulk estimates from WRF are in good agreement with measurements at Horns Rev in the North Sea, but for sites closer to the coast.

Some of the most common parameters used to classify atmospheric stratification are presented below-

1. Heat flux (H)

It is the amount of heat that is going into or coming out of the surface per unit area, a direct cause of temperature differences between the atmosphere and the surface. The heat flux is considered negative when heat goes from the atmosphere into the surface of the Earth, and positive when heat comes out of the surface of the Earth into the atmosphere. Stability conditions can be defined using heat flux in the following way:

- $H > 0 \rightarrow$ Unstable
- $H = 0 \rightarrow$ Neutral
- $H < 0 \rightarrow$ Stable

2. Monin-Obukhov Length (L)

A direct approach to estimating the atmospheric stratification is the calculation of the Monin-Obukhov length L , a length scale parameter that expresses the ratio of shear induced turbulent kinetic energy (TKE) change to buoyancy induced TKE change. L can be estimated using turbulent fluxes using Equation 2

$$L = -\frac{T \cdot u_*^3}{g \cdot \kappa \cdot \overline{w' \cdot \theta'_v}}$$

where T is the absolute air temperature, u_* is friction velocity, g is the Earth's gravitation acceleration, κ is 0.4 (von Kármán constant), and $\overline{w' \cdot \theta'_v}$ is the kinematic virtual heat flux.

However, the difficulty in estimating momentum and heat fluxes in WRF introduces a high uncertainty and difficulty in using the direct calculations of the Monin-Obukhov length to estimate the atmospheric stratification.

3. Bulk Richardson Number (Ri_B)

The Bulk Richardson Number is the most frequently used Richardson number (Ri) to classify stability conditions [39]. The Bulk Richardson number is easy to estimate using commonly available observations, and is given by the following equation 2.1 [16] [27] [40].

$$Ri_B = \frac{g^{\frac{T_2-T_1}{z_2-z_1}}}{\left(\frac{T_1+T_2}{2} + 273.15\right) \left(\frac{U_2-U_1}{z_2-z_1}\right)^2} \quad (2.1)$$

where g is the acceleration due to gravity, $T_2 - T_1$ is the difference between the absolute temperatures at the two levels z_2 and z_1 with corresponding wind speeds U_2 and U_1 respectively. The lower level z_1 used is the sea surface, where wind speed U_1 is considered to be 0 ms^{-1} .

A critical Bulk Richardson number Ri_{Bc} is used to distinguish between the atmospheric stability classes. Studies have shown the estimate of the Ri_{Bc} to vary a lot, showing a considerable uncertainty in the choice of an appropriate value. As an example, Fay et al. [41] estimated the value of Ri_{Bc} to be 0.38, whereas Gryning and Batchvarova [42] found the values between 0.03 to 0.05 to perform the best over sea. Larsén et al. [40] calculated Bulk Richardson number values using measurements from the water surface and lowest wind measurement level, and the used the following classification regimes:

- $Ri_B > 0.015 \rightarrow \text{Stable}$
- $0 \leq Ri_B \leq 0.015 \rightarrow \text{Neutral to Stable or Near Neutral Stable}$
- $Ri_B < 0 \rightarrow \text{Unstable}$

Due to this uncertainty in the Ri_{Bc} value, the stability conditions are estimated using a relationship between the Monin-Obukhov length (L) and the Ri_B as shown in Equations 2.2 and 2.3 [30] [43] [39] [36].

$$\frac{z}{L} = 10Ri_B \quad \text{when } Ri_B \leq 0 \quad (2.2)$$

$$\frac{z}{L} = \frac{10Ri_B}{1 - 5Ri_B} \quad \text{when } Ri_B > 0 \quad (2.3)$$

Classification of the atmospheric stability is performed based on the regime that the value of L belongs to as shown in Table 2.2.

Obukhov length L (m)	Atmospheric Stratification
-500 \leq L < 0	Unstable
500 < L	Neutral
200 < L \leq 500	Near Neutral Stable
0 \leq L \leq 200	Stable

Table 2.2: Atmospheric stratification or stability classes according to intervals of the Obukhov length.

In this project, the Bulk Richardson number Ri_B has been calculated. The relationship between Ri_B and Obukhov length L as shown in Equations 2.2 and 2.3 are used in combination with the stability classification method as presented in Table 2.2.

Chapter 3

Weather Research and Forecast (WRF) Model

This chapter provides a description of the Numerical Weather Prediction (NWP) model, wind farm parametrisations and model setup used within the scope of this thesis. Chapter 3.1 provides an overview of the WRF v 3.8.1 environment. Chapter 3.2 describes the need for wind farm parametrisation in WRF, followed with an insight into the Fitch scheme scheme and the Explicit Wake Parametrisation (EWP). Chapter 3.3 outlines the WRF model setup used in this thesis. Chapter 3.4 provides an understanding of how the wind farm affected flow regions as seen in WRF are obtained.

3.1 WRF Environment

This project uses the following publicly available mesoscale Numerical Weather Prediction (NWP) model - Advanced Research Weather Research and Forecast Model (ARW-WRF) version 3.8.1. The WRF modelling system is a state-of-the-art atmospheric simulation tool used in a wide range of applications within atmospheric research and operational forecasting [23]. WRF can be run at different spatial resolutions, ranging from $\geq 1\text{km}$ to global scales. As an example of the range of options available, WRF v 3.8.1 has 17 schemes for micro-physics, and 13 for atmospheric boundary layer (ABL) [44].

Some major features of the ARW system (version 3) [23]:

- Fully compressible, Euler non-hydrostatic (with hydrostatic option) form of the Reynolds-averaged Navier-Stokes (RANS) equation.
- 3rd-order Runge-Kutta time integration scheme with variable time step option.
- Turbulent kinetic energy (TKE) prediction possible in the planetary boundary layer (PBL) physics schemes.
- Complete Coriolis, curvature and mapping terms included.
- One-way interactive, two-way interactive and moving nesting possibility.
- Grid and observation nudging possible.
- Mass-based terrain following eta coordinates (η).

- Arakawa C-grid staggering in horizontal grid.
- Velocity components u and v are solved in the Cartesian coordinate system.

Two different types of simulations can be run in WRF: ideal initialization and real data [45]. An ideal case uses artificially generated initial conditions, whereas a real case uses assimilated observation data which requires the WRF Pre-Processing System (WPS).

Figure 3.1 gives an overview of the WRF modelling system, which consists of the WPS and WRF system. The WPS prepares the required input data for real simulations. The geogrid program defines the model domains and static geographical data is interpolated to the grids, based on which the ungrid program extracts meteorological observation or reanalysis data from the grib format. The metgrid program interpolates this data horizontally to the model domain and grid specifications, to create the metgrid files. The vertical extrapolation of this data to the specific model eta levels occurs in the real program in WRF.

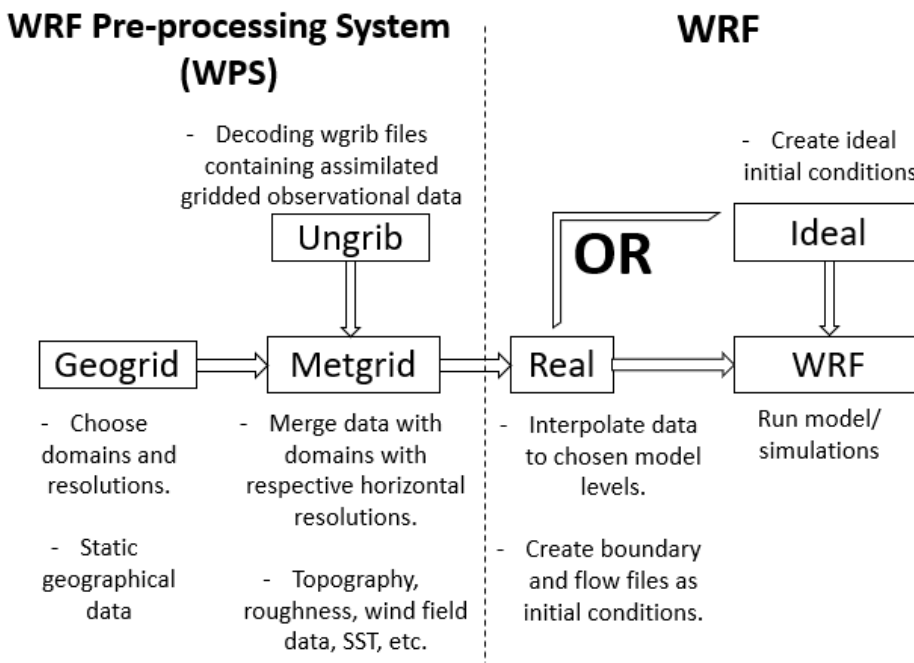


Figure 3.1: WRF model system overview, a modified version of the flowchart in [WRF_modelling_system_overview].

Using the initial and boundary conditions, the relevant equations are solved in space and time to give the output.

3.2 Wind Farm Parametrisation in WRF

The grid resolution in the vertical direction in mesoscale models is of the order of tens of metres, whereas the horizontal grid resolution of mesoscale models ranges upwards of 1 km. Due to this the turbine-induced velocity deficit in the vertical

direction can be captured to a satisfactory extent, but not in the horizontal direction, because of which the effect of wind turbines must be parametrised in WRF.

The following two schemes of wind turbine parametrisation have been explored in this project:

1. Fitch scheme
2. Explicit Wake Parametrisation (EWP) scheme

Some key points about the wind farm parametrisation:

- All turbines are assumed to be perpendicular to the flow in both the parametrisation schemes.
- Turbine allocation to grid cells in WRF are defined by turbine latitude and longitude, or by selecting turbine placement in i and j cells manually. In this project, the turbine latitudes and longitudes are used to allocate turbines to grid cells. Hence, more than 1 turbine might be in a given grid cell if the grid spacing is greater than the distance between the turbines.
- Therefore, wake effects between turbines in the same cell are not accounted for, but wake effects between turbines in different cells are.
- All turbines within a grid cell are assumed to be positioned at the grid cell centre.

3.2.1 Fitch Scheme

The Fitch scheme is already included in WRF v3.8.1 as a wind turbine parametrisation option [12]. It models the wind turbine drag as a function of the extracted kinetic energy (KE) by the turbines, which is dependent on the thrust coefficient of the turbine obtained from the thrust curve of the turbine. This also implies that this extracted KE from the atmosphere is a function of wind speed.

The Fitch scheme models the effects of turbines on the atmosphere by representing turbines as a momentum sink, transferring some of the KE to electricity, and the remaining to Turbulent kinetic energy (TKE). This shows up as a large and sharp increase in TKE at the wind farm turbine locations in WRF. Fitch et al. [12] observed that the generation of TKE is restricted to the wind farm area, and downstream of the wind farm it decays relatively fast as seen Figure 3.2. The turbine generated TKE which is concentrated in the wind farm area, is transported in the vertical, and this accounts for the largest source of TKE outside the turbine rotor area apart from shear production.

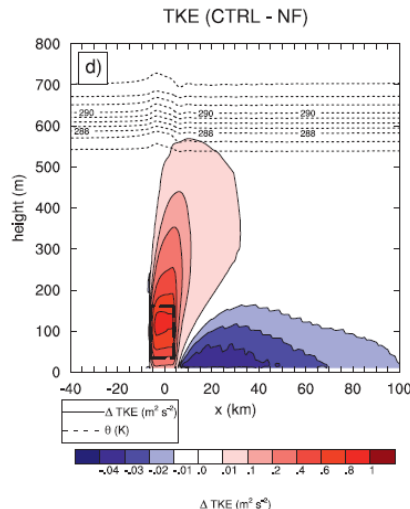


Figure 3.2: Vertical cross section of the mean difference over the wind farm and wake region of TKE as taken from Fitch et al. (2012) [12]

The drag force induced on the flow by a wind turbine is given by the following equation.

$$F_{drag} = \frac{1}{2} c_T(|V|) \rho |V| V A$$

where c_T is the turbine thrust coefficient which is obtained from the turbine thrust curve, $V = (u, v)$ is the horizontal velocity, and ρ is the air density.

As mentioned, TKE is all the non-productive drag produced by the rotor. Hence, the rate of loss of KE caused by the turbine rotor on the atmosphere due to the variation of horizontal winds in the vertical, is obtained by integrating these losses over the rotor area as shown in the following equation.

$$\frac{\partial KE_{drag}}{\partial t} = -\frac{1}{2} \int_{A_r} c_T(|V|) \rho |V|^3 dA$$

where A_r is the rotor cross-sectional area.

As earlier mentioned, the grid spacing may be larger than the spacing between two turbines, which leads to more than one wind turbine located in a single grid cell. This density of turbines is described by N_t^{ij} , where i and j are the model grid cell indices in the x (zonal) and y (meridional) directions respectively. The electrical energy produced by a turbine is given by the following equation.

$$\frac{\partial P_{ijk}}{\partial t} = \frac{\frac{1}{2} N_t^{ij} c_P(|V|_{ijk}) |V|_{ijk}^3 A_{ijk}}{z_{k+1} - z_k}$$

where z is the height at the model level k .

Similarly, the TKE which is the turbine extracted KE which is not converted to electricity is given by the following equation.

$$\frac{\partial TKE_{ijk}}{\partial t} = \frac{\frac{1}{2} N_t^{ij} c_{TKE} (|V|_{ijk}) |V|_{ijk}^3 A_{ijk}}{\Delta z}$$

To generalize, the Fitch scheme parametrises the additional TKE source term as shown in the following equation.

$$\langle \bar{p}_{t,Fitch} \rangle = \frac{\rho A_r (c_T - c_P) \langle |\bar{u}| \rangle^3}{2}$$

where $\langle |\bar{u}| \rangle$ is the absolute value of the grid-cell velocity.

3.2.2 Explicit Wake Parametrisation (EWP) Scheme

The EWP scheme is a more recent parametrisation scheme developed by Volker et al. (2016) at DTU Wind Energy, Risø [11]. Similar to the Fitch scheme, the EWP scheme models wind turbines as a drag device causing the wind speed to slow down by extracting KE from the wind. The EWP scheme, expressions for the volume-averaged drag force $\langle \bar{f}_d \rangle$, and volume-averaged turbulence induced by the turbine $\langle \bar{p}_t \rangle$ are obtained, with the volume average denoted by the angle brackets. This turbulence term depends on the velocity perturbation. This scheme defines the turbulence fluctuations around the ensemble mean by including only random motion in the TKE, and this TKE is derived from shear. The EWP scheme defines the volume-averaged turbulence induced by the turbine $\langle \bar{p}_t \rangle$ as shown in the following equation.

$$\langle \bar{p}_t \rangle = -\rho A_r c_T \langle \bar{u}_{i,h} \bar{u}'_{i,h}^2 \rangle$$

The magnitude of this term which represents a sink of TKE due to momentum extracted is much smaller in comparison to the additional term in the Fitch scheme, hence this term is neglected in the EWP scheme. Therefore, as mentioned above the TKE generated in this scheme is derived from the dominant mechanism in the grid-cell average - the shear production. The EWP scheme also accounts for the velocity deficit expansion in the vertical direction due to the wake decay-coefficient, which causes a perturbed flow regions beyond the rotor-swept area. This vertical velocity deficit profile is obtained by equating the momentum loss due to the wind turbine to the total thrust produced which is obtained from the thrust curve as shown in the following equation.

$$\frac{1}{2} \rho c_T \pi r_o^2 \bar{u}_o^2 = \rho \bar{u}_o \bar{u}_s 2 \pi \sigma^2$$

where the l.h.s terms represent the rotor swept area local forces, and the r.h.s represents the equivalent distributed force at any distance x in the expanded wake region. Here, \bar{u}_o represents the advection velocity at hub height, \bar{u}_s the maximum velocity deficit, σ is the length scale that determines wake expansion, and r_o is the rotor radius. By averaging the velocity deficit over the cross-stream direction y and over a

downstream distance L that the wake travels within the grid cell, the effect velocity profile is obtained.

The grid-cell-averaged acceleration components for every vertical layer in the model k are obtained, and added to the numerical approximation of the Reynolds-averaged Navier-Stokes (RANS) equations described in the following equation.

$$\frac{\partial \bar{u}_i}{\partial t} + \bar{u}_j \frac{\partial \bar{u}_i}{\partial x_j} = \frac{-1}{\rho} \frac{\partial \bar{p}}{\partial x_i} - 2\epsilon_{ijk} \Omega_j \bar{u}_k - \delta_{i3} g + \bar{f}_{d_i}$$

3.3 WRF Model Setup in the Current Study

As earlier mentioned, the simulations described in this study use the model - Advanced Research WRF version 3.8.1. The simulations that have been carried out cover a large area of Northern Europe. The first 24 hours of all simulations have been discarded, as these first 24 hours are considered to be the spin-up period. The simulations consist of three domains with horizontal resolutions 9 km, 3 km, and 1 km respectively, and two of domains are one-way nested. The model is configured with 41 vertical levels, with the first 10 levels within 400 m of the surface, with the first level located approximately at 15 m above surface level. The domain configurations are shown in Figure 3.3.

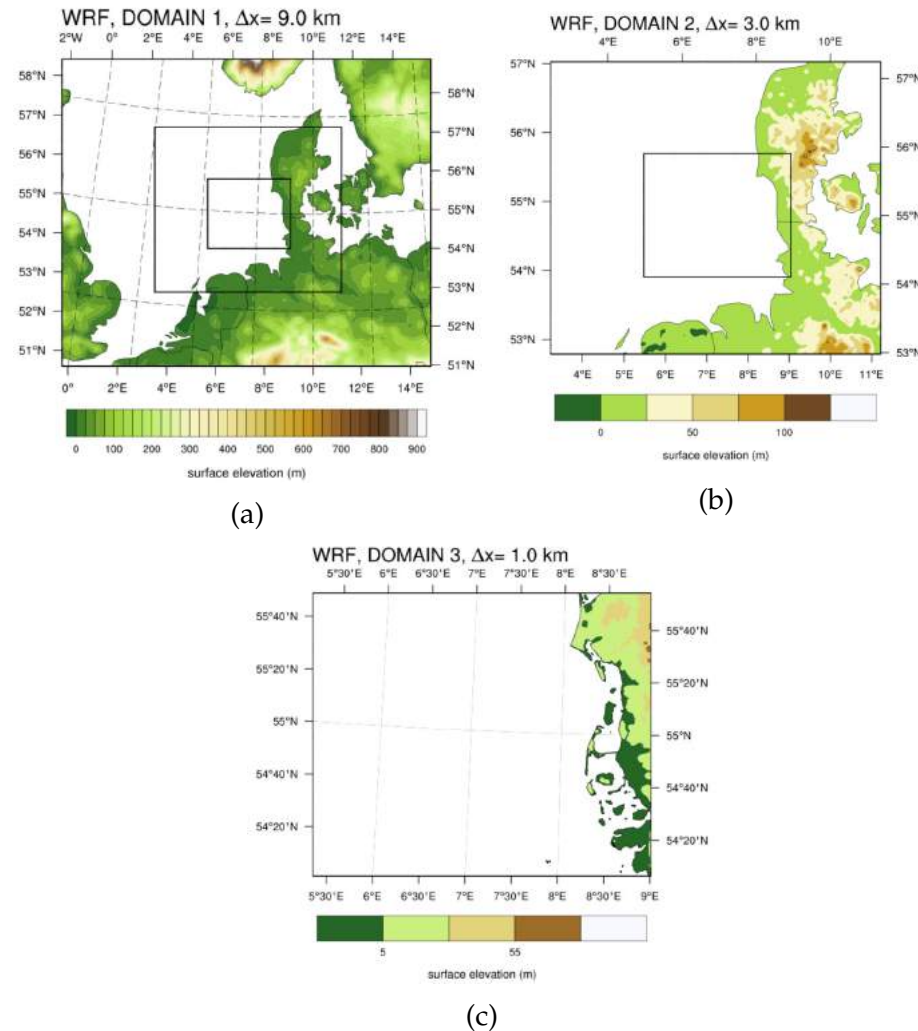


Figure 3.3: WRF model domain configurations and terrain elevation (m) maps. (a): $9 \text{ km} \times 9 \text{ km}$ domain (D1), (b): $3 \text{ km} \times 3 \text{ km}$ domain (D2), and (c): $1 \text{ km} \times 1 \text{ km}$ domain (D3). The inner lines show the positions of the nested-domains.

The details of the WRF v3.8.1 model and system setup, with the physical parametrisations used in the simulations are presented below.

Model setup:

- Lambert projection with 3 domains - Mother domain (D1: 120×100 grid points) with 9 km grid spacing; 2 one-way nested domains: D2 (181×160 grid points) with 3 km grid spacing, and D3 (241×202 grid points) with 1 km grid spacing.
- 41 vertical levels with model top at 50 hPa; with 10 of the levels within 400 m from the surface, with first six levels located at approximately: 16, 50, 83, 117, 150, and 184 m respectively.
- Corine land-cover classification used.

Simulation setup:

- Initial and boundary conditions, Sea Surface Temperature (SST) data, and fields for grid nudging are obtained from the European Centre for Medium Range Forecast (ECMWF) ERA5 Reanalysis data.
- Runs are started at 00:00 UTC for every simulation and outputs are stored 10 minutes for D3.
- Spectral nudging only on D1; wavenumber 15 and 11 in the zonal and meridional direction. Nudging coefficient value used is VALUE 0.0003s^{-1} .

Physical parametrisations:

- Microphysics option = WSM 5-class scheme.
- Radiation: RRTM scheme for longwave (option 1); Dudhia scheme for short-wave (option 1).
- Boundary layer PBL: MYNN 2.5 level TKE scheme (option 5) as recommended in Volker et al. (2012) [11].
- Surface-layer scheme: MYNN surface layer (option 5).
- Unified Noah Land Surface Model (option 2).
- Boundary layer MYNN tke advection (bl_mynn_tkeaddvect) is on.
- Kain-Fritsch cumulus parametrisation (option 1) only on D1.
- Wind farm parametrisation options: Fitch scheme and EWP scheme only on the innermost domain (D3).

The WRF modelled outputs are then post-processed: interpolation, destaggering, etc., and the first 24 hours of each simulation are treated as spin-up time and disregarded.

3.4 Flow Region Affected by Wind Farms in WRF

Using the above mentioned setup configuration, WRF simulations are run for the simulations around each identified case in four different ways:

- With the wind farm scheme on in D3 with both wind farms WF1 and WF2.
- Without the wind farm scheme on in D3 without any wind farms.
- With the wind farm scheme on in D3 but only with WF1.
- With the wind farm scheme on in D3 but only with WF2.

By taking the difference between setup 1 with both the wind farms WF1 and WF2, and setup 2 without both wind farms, analysis of the flow region affected by the wind turbines is done.

As the wakes from one wind farm are seen to interact with the other from SAR images, it is expected that the wakes from one wind farm affect the power production of the other. To understand what the power production of each wind farm would

be if the wind farm wakes do no interact with one another, the simulations are run with setup 3 and 4 separately.

The modelled power production obtained from setup 3 and 4 are combined to obtain the total theoretical power production - the sum of the power productions of each wind farm if the other had not been there. In this manner, the difference in power predictions from setup 1 and the combination of setup 3 and 4 is calculated to estimate the power losses due to inter-farm wake interaction. It must be remembered that inter-turbine wake interaction within a single grid-cell is not calculated, but the inter-turbine wake interaction between grid-cells is. This is done in order to quantify the inter-farm interaction and the effect on power production.

On obtaining the difference in the wind field between with the wind farm schemes and without, the velocity and TKE deficit region can be further analysed. A horizontal-cross section at a height of 90 m of the horizontal wind speeds field is used to do this. The height of 90 m is arbitrarily selected as it is the closest value near the tenth metre between the hub heights of the turbines used in the two wind farms i.e. WF1 at 94.75 m and WF2 at 88 m. Further, a line perpendicular to the upstream wind direction identified at a fixed location is drawn through the wind farms from control points. These control points are also based on this upstream wind direction. As an example, if the wind direction is westerly, an individual point on the eastern edges of each of the wind farms is identified as the control point. Lines that pass through these control points are then drawn at the corresponding wind direction, and flow field values at points along these lines are obtained to analyse the flow through the velocity deficit regions.

Chapter 4

Analysis of Measurements

Meteorological (MET) mast measurements have been used to analyse the atmospheric conditions and wind flow characteristics within the wind farm region. Further, the measurements have been used to identify two additional cases to be modelled - one belonging to the unstable condition category, and the other to stable condition.

Wind farm measurements from SandBank (WF1) and DanTysk (WF2) have been used to evaluate the quality of the WRF-modelled power production, and to analyse the performance of the two parametrisation schemes - the Fitch scheme and EWP scheme, under different conditions.

4.1 Wind Farm Measurements

The two wind farms SandBank (WF1) and DanTysk (WF2), along with the Fino3 MET mast are located offshore in the North Sea as shown in Figure 2.1. Under the "OffshoreWake Project" [46], Vattenfall has made the data for the wind farms available for use in this project.

The following measurements have been used in this project:

- Turbine level active power and nacelle measured wind speed measurements for WF2 (DanTysk) from 2014-12-01 to 2018-12-04.
- Turbine level active power and nacelle measured wind speed measurements for WF1 (SandBank) from 2016-12-06 to 2018-12-04, with missing data from 2017-05-05 to 2018-01-01.
- Grid measured power measurements for WF1 from 2017-01-01 to 2018-10-31.
- WF2 power observations have been scaled up using the available park curtailment set-point and rated power/turbine availability values for WF2, and using the provided park curtailment set-point values for WF1.

Suitable combinations of the power measurements (either grid measured or turbine measured for WF1) have been used for different periods of time, as the data sets have missing and invalid data. Periods of low availability, curtailment, and construction phase which are visible in the power time series, have been treated wherever possible, provided curtailment or rated power data for those time stamps are available.

Using the valid data and discarding the commissioning phase, the following starting dates are identified for valid production data:

- DanTysk (WF2) → 2015-01-01
- SandBank (WF1) → 2017-01-01

Using the turbine level active power measurements and nacelle measured wind speeds, the operational median power curves for every turbine (in various colours) are calculated and compared against the manufacturer's power curves (indicated in black) as shown in Figure 4.1. It can be seen, the median power curves for WF1 (a) and WF2 (b) turbines agree well with the manufacturer power curve, with minor deviations towards the tail (right-end) of the power curve which are expected due to possible curtailment at high wind speeds, which lowers the median power production value in the respective bins.

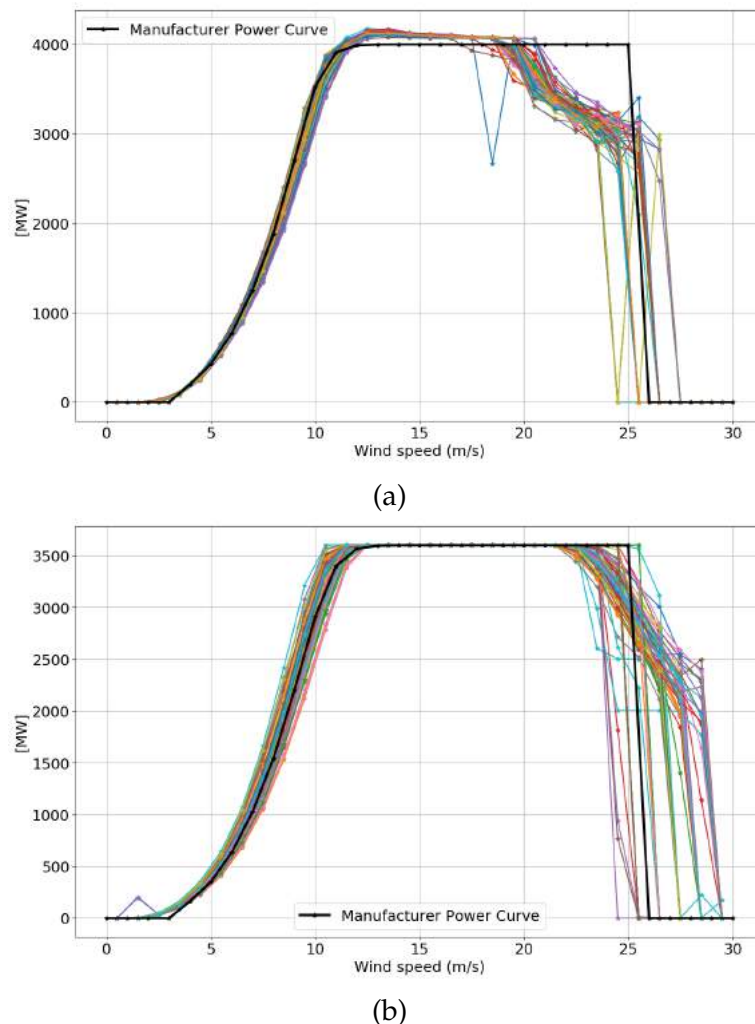


Figure 4.1: Median power curve from turbine measured power and wind speed in different colours against the manufacturer power curve indicated in black for WF1 (a) and WF2 (b).

This deviation in the median power curves of the turbines from WF1 (a) during high wind speeds and in the region around rated-power where it produces marginally

higher power than the rated capacity, may result in introducing a bias when comparing modelled power from WRF using the wind farm parametrisation schemes, as the WRF modelled power uses the manufacturer power curve without any deviations. The median power value in each bin is used as the median does not penalise as much as the mean would in the presence of lower values than expected in bins - due to reasons such as curtailment.

4.2 Fino3 Meteorological (MET) Mast

The Fino3 MET mast measurements have been provided by BMWi (Bundesministerium für Wirtschaft und Energie) and PTJ (Projectträger Jülich). Wind speed, wind direction, and temperature measurements between 2013-01-01 and 2018-09-01 have been used within the scope of this project.

Figure 4.2 shows the wind rose for the wind speed measurements from the cup anemometer at 90 m mounted at 345° ; wind direction measurements from the wind vane at 100 m mounted at 105° . However, no cleaning or removal of measurements influenced by the wind farms has been performed. The circular axis is in percentages. It can be seen that majority of the wind speeds are from the Western, South-Western, and North-Western directions. The duration of measurements shown is from 2013-01-01 00:00 to 2018-08-31 23:50.

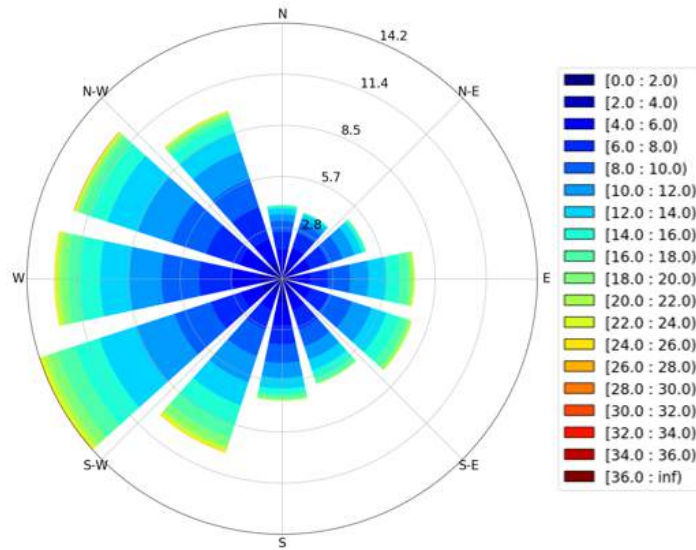


Figure 4.2: Wind rose (% frequency along circular axes) from Fino3 MET mast data between 2013-01-01 and 2018-08-31.

Since the valid power production data available for WF2 starts from 2015-01-01, and that for WF1 from 2017-01-01, three phases have been identified for use with Fino3 data:

- Pre-construction → from 2013-01-01 up to 2015-01-01.
- Post-construction → from 2015-01-01 up to 2018-09-01 00:00.

- WF1+WF2 (when both are producing power) → from 2017-01-01 up to 2018-09-01 00:00.

Table 4.1 presents the mean wind speeds for the three identified phases. It can be seen that there is a difference of 1.08 ms^{-1} in the mean wind speed before construction and after the construction of both wind farms (WF1+WF2). This is indicative of either reduced wind speeds resulting from the influence of the wind farms on the Fino3 measurements or inter-annual variability.

	Total	Pre-construction	Post-construction	WF1+WF2
Start date	2013-01-01	2013-01-01	2015-01-01	2017-01-01
End date	2018-09-01	2015-01-01	2018-09-01	2018-09-01
Mean Wind Speed (ms^{-1})	9.51	10.02	9.26	8.94

Table 4.1: Mean wind speeds (ms^{-1}) for the total period and the three identified phases.

Figure 4.3a shows the wind roses using the same measuring instruments where: (a) for the pre-construction period, and (b) for the post-construction period. The values are normalised due to the difference in the duration and number of observations used for each period.

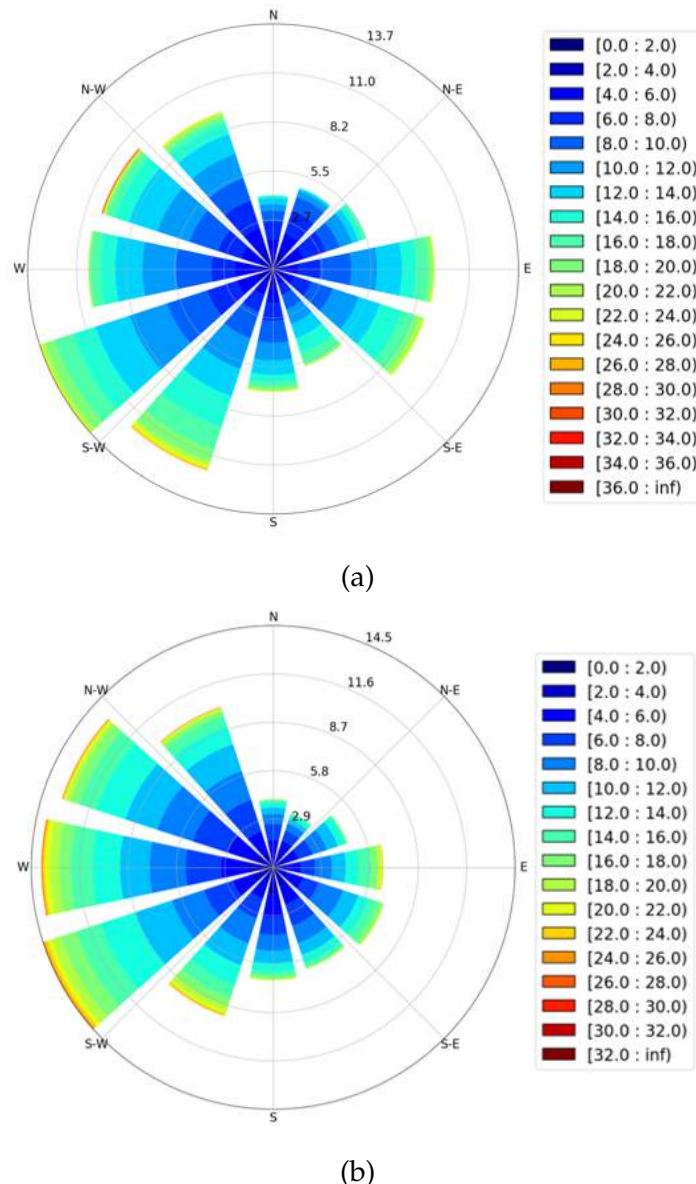


Figure 4.3: Wind rose (% frequency along circular axes) from Fino3 wind speed measurements at 90 m height for (a) pre-construction: 2013-01-01 up to 2015-01-01, and (b) post-construction: 2015-01-01 up to 2018-09-01.

It can be seen that there are greater percentages of wind observations from the W, WNW and WSW directions for the post-construction (b) period when compared to the pre-construction (a) period. It can also be seen that there are smaller percentages of wind observations from the E, ESE, and ENE directions, which could be indicative of the influence of WF2 on the measurements - as Fino3 is on the eastern edge of WF2.

Figure 4.4 shows the comparison of wind speeds and the respective normalised frequencies using the same measuring instruments, for the pre-construction period and post-construction period.

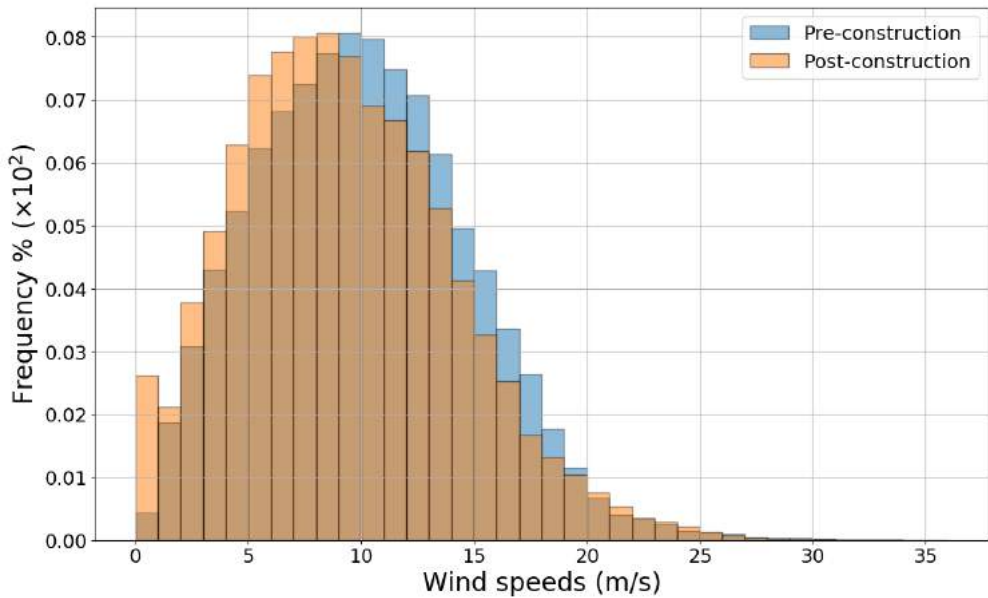


Figure 4.4: 90 m Wind speed histograms with normalised frequencies for the Pre-construction: 2013-01-01 up to 2015-01-01, and Post-construction: 2015-01-01 up to 2018-09-01.

It can be seen that there is a shift in the wind speeds, with the wind speed distribution indicating higher wind speeds pre-construction of the wind farm. This could also reflect inter-annual variability. However, there is a considerable increase in the frequency in the wind speed bin 0ms^{-1} - 1ms^{-1} , with a frequency of around 0.4 % of the total time period of pre-construction, to around 2.6 % of the total time period of post-construction, which indicates the influence of the wind farms on the wind speeds measured at Fino3.

Figure 4.5 shows the Bulk-Richardson number (Ri_B) distribution at Fino3, which is estimated using Equation 2.1. The following parameters have been used to estimate the Ri_B : wind speeds from the cup anemometer 30 m and sea surface (assumed to be zero); temperature measurements at 29 m height and the buoy for sea surface temperature; with the heights (z_2 and z_1) used at the two levels are 29 m and 0 m respectively.

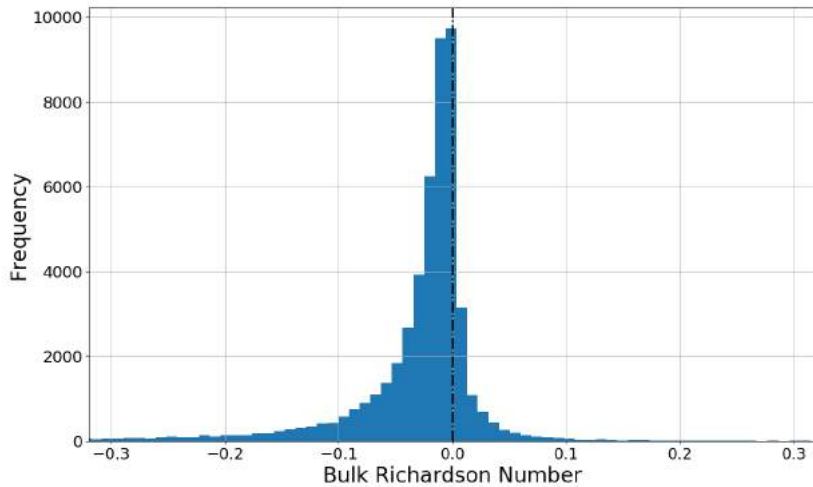


Figure 4.5: Bulk Richardson Number distribution at Fino3 between 2014-09-01 00:10 and 2018-05-31 23:30

It can be seen, that the highest frequency is for Ri_B values around 0 and to the negative side of the distribution, indicating a neutral to near-neutral unstable atmosphere dominating the location of measurements. Based on the Bulk-Richardson number distribution as shown in Figure 4.5, two more cases - one under stable condition and the other under unstable condition have been identified to be modelled. The following conditions have been applied to the data set find these two cases to be modelled:

1. $0^\circ \leq \text{Wind Direction} < 140^\circ$ and $190^\circ \leq \text{Wind Direction} < 360^\circ$. As the wind speed measuring instrument is mounted at an angle of 345° from True north, measurements between 140° and 190° have been ignored.
2. $6ms^{-1} \leq \text{Wind Speed} \leq 15ms^{-1}$.

As most of the visible wind speed deficits are expected to be within this range.

Chapter 5

Simulation Results and Analysis

Using the WRF model setup as shown in Chapter 3.3, the identified cases have been modelled in WRF v3.8.1. The WRF model is initialized 24 hours before the start date of each respective case, to allow for spin-up time as presented in Chapter 3.3. This chapter details the analysis of the WRF simulations for the two wind farm parametrisation schemes.

Chapter 5.1 presents an overview of the snapshots of the WRF modelled wind field at 10 m for the corresponding satellite SAR images presented in Chapter 2. Chapter 5.2 presents the analyses of the snapshots - wind speed deficit and TKE difference fields using simulations run with and without the wind farm parametrisations. Finally, analyses of the effect of stability on wakes and power production are presented in Chapter 5.3 and Chapter 5.4 respectively.

Table 5.1 outlines the cases (snapshots) as identified in Chapter 2.2 (Satellite SAR images) and Chapter 4 (Fino3 MET mast data), with the temperature difference measured between 29 m height and sea surface temperature from a buoy.

Table 5.1: Identified cases to be modelled, along with the case name with which they are referred to hereafter.

Source	Case Name	Time stamp (UTC)	Fino3 Δtemp ($T_{\text{air}} - T_{\text{water}}$)
Fino3	Case 1	2016-09-13 16:20	6.82
	Case 2	2016-11-02 08:20	-4.69
Satellite SAR image	Case 3	2017-05-11 17:20	NA
	Case 4	2018-04-24 17:20	NA
	Case 5	2018-04-27 05:40	NA

Case 1 is estimated to fall under stable condition, and Case 2 to fall under the unstable condition category based on the temperature difference of air at 28 m and the sea surface from the Fino3 MET mast measurements. However, no valid measurements from Fino3 are available for or around the time instances of Cases 3, 4, and 5. The assumption made here is that a neutral condition time instant will be present in at least one of the 5 simulations of 24 hours, and this is verified by estimating the stability conditions from the WRF simulation in Chapter 5.3.

In addition to the 5 simulations corresponding to these 5 cases, an additional simulation covering a period of 10 days (including spin-up time) is run using the same WRF model setup. This is because power measurements are only available covering 3 out of the 5 initial simulations, which results in a relatively small sample of power

measurements to validate WRF-modelled power against. Therefore, this 10 day period is selected by identifying valid and representative power measurements from both wind farms. This simulation covering a period of 10 days is hereby referred to as *9-day Sim.* (9 days excluding spin-up time of 24 hours). However, this simulation is only run for one configuration, with the wind farm scheme on with both wind farms are present in the innermost domain (D3). Therefore, wake lengths or power losses are not estimated for this simulation period, and it is used solely for evaluating the WRF-modelled power production.

The 5 simulations are run for a period of 48 hours, with the first 24 hours being discarded as they are considered as spin-up time. As an example for Simulation 1, the time instant identified is 2016-09-13 16:20. The simulation is then set up to run from 2016-09-12 00:00 to 2016-09-14 00:00, and only the period from 2016-09-13 00:00 to 2016-09-14 00:00 is considered. Complete details of this for all simulations are presented in Table 5.2.

Table 5.2: Initialisation time, run hours, end of simulation, and spin-up hours for the identified cases.

Name	Initialisation (UTC)	Run time (hours)	End of simulation (UTC)	Spin-up time (hours)
Simulation 1	2016-09-12 00:00	48	2016-09-13 23:50	24
Simulation 2	2016-11-01 00:00	48	2016-11-02 23:50	24
Simulation 3	2017-05-10 00:00	48	2017-05-11 23:50	24
Simulation 4	2018-04-23 00:00	48	2018-04-24 23:50	24
Simulation 5	2018-04-26 00:00	48	2018-04-27 23:50	24
9 day Sim.	2018-04-13 00:00	240	2018-04-22 23:50	24

5.1 Modelled Wind Speed Field vs. Satellite Images

On running the simulations, the 10 m wind speed fields for the innermost domain D3 for the identified time instances are inspected to compare against the Satellite SAR images (10 m). Since the grid spacing or resolution of D3 is $1 \text{ km} \times 1\text{km}$, the WRF 10 m wind speed field plot is made against the domain i and j values for a clearer visualisation of scale of flow effects occurring. Chapter 5.1.1 presents the modelled 10 m wind speed field using the EWP scheme for snapshots from Case 3, 4, and 5, and the Variation of WRF-EWP wind direction with time from an upstream undisturbed flow location from about 4 hours before to 4 hours after the time instant in the snapshot. The wind direction does not change much over the period of about 8 hours, except by about 45° in Case 3 (2017-05-11 17:20) for both EWP scheme and Fitch scheme. Chapter 5.1.2 presents the same but for the Fitch scheme.

5.1.1 EWP Scheme

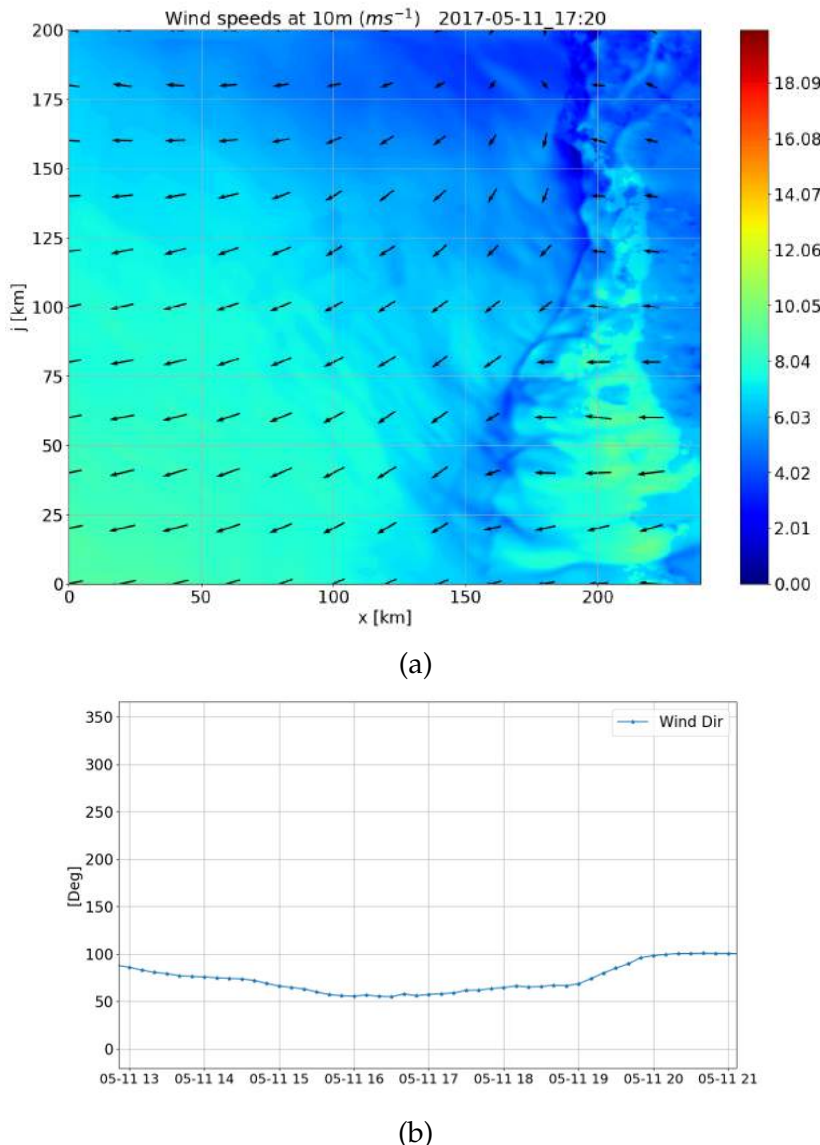


Figure 5.1: Case 3 (2017-05-11 17:20): WRF-EWP wind speed field (a); Variation of WRF-EWP wind direction with time at an upstream undisturbed location - both at 10m above surface.

In Figure 5.1, it can be seen that the simulation shows a good agreement with the satellite SAR image (see Figure 2.2). The simulation is able to capture the overall wind speed range, wind direction, presence of the wakes, and the complex-looking high-wind speed structure to the east of the images. The different ranges of wind speeds across the different parts of the image are also visible. Though some physical structures may differ in appearance, it must be remembered that these are mesoscale model results and not microscale simulations, and also that the satellite SAR images are retrieved 10 m wind speeds based on measurements of the sea surface and not true measurements. Also, wakes from neighbouring wind farms of WF1 and WF2 are seen in the SAR image, but are not present in the WRF-EWP simulation as these

wind farms have not been parametrised in the simulation. But in general, the simulations capture adequately the wind speed field.

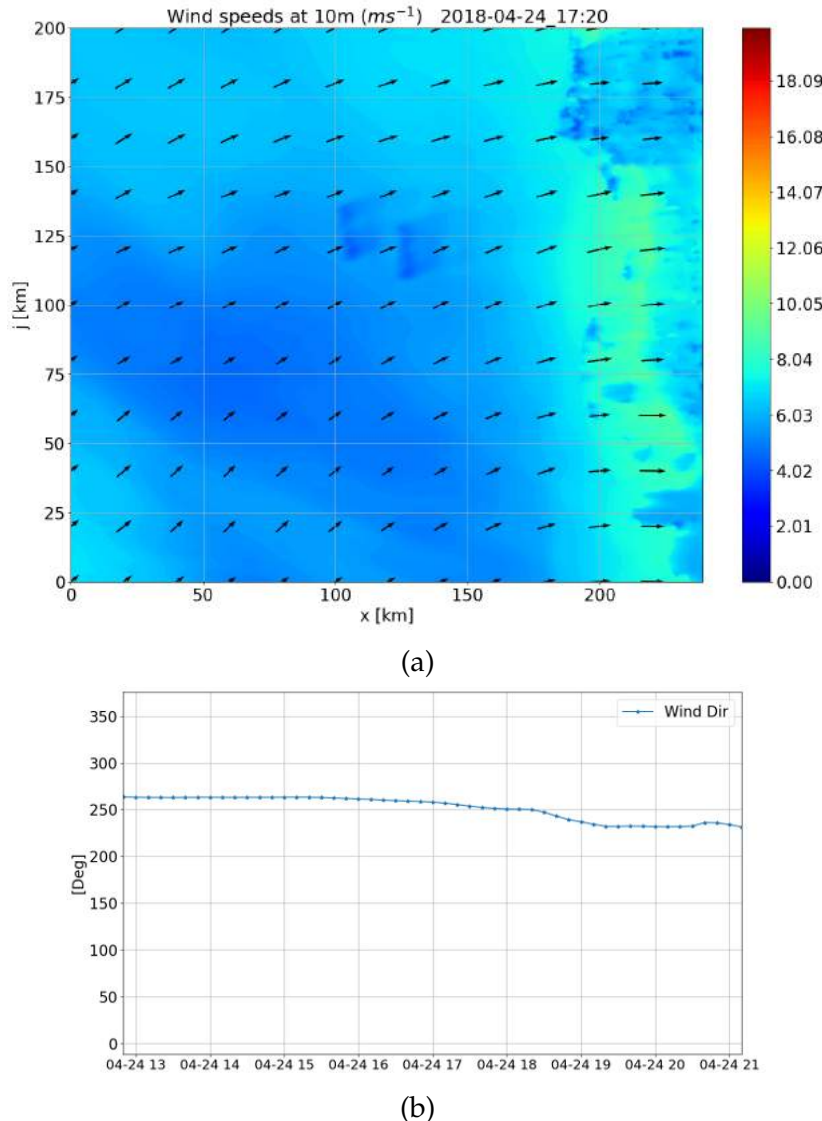


Figure 5.2: Case 4 (2018-04-24 17:20): WRF-EWP wind speed field (a); Variation of WRF-EWP wind direction with time at an upstream undisturbed location - both at 10m above surface.

In Figure 5.2, it can be seen that the simulation shows a reasonable agreement with the satellite SAR image. The simulation is able to capture the wind direction, presence of the wakes, though a part of WF2 is not visible in the SAR image. Though, the gravity-wave like structures present in the SAR retrieved wind field do not show up in the WRF-EWP simulation. The downstream flow presented in the SAR image, show regions of increased wind speed in comparison to the upstream and free stream flow. This is not the case in the EWP simulation, which presents the wake as a region of reduced wind speeds. However, the WRF-EWP simulation captures very well the wake region, the length and slight turning or meandering of the wake from WF1 (red).

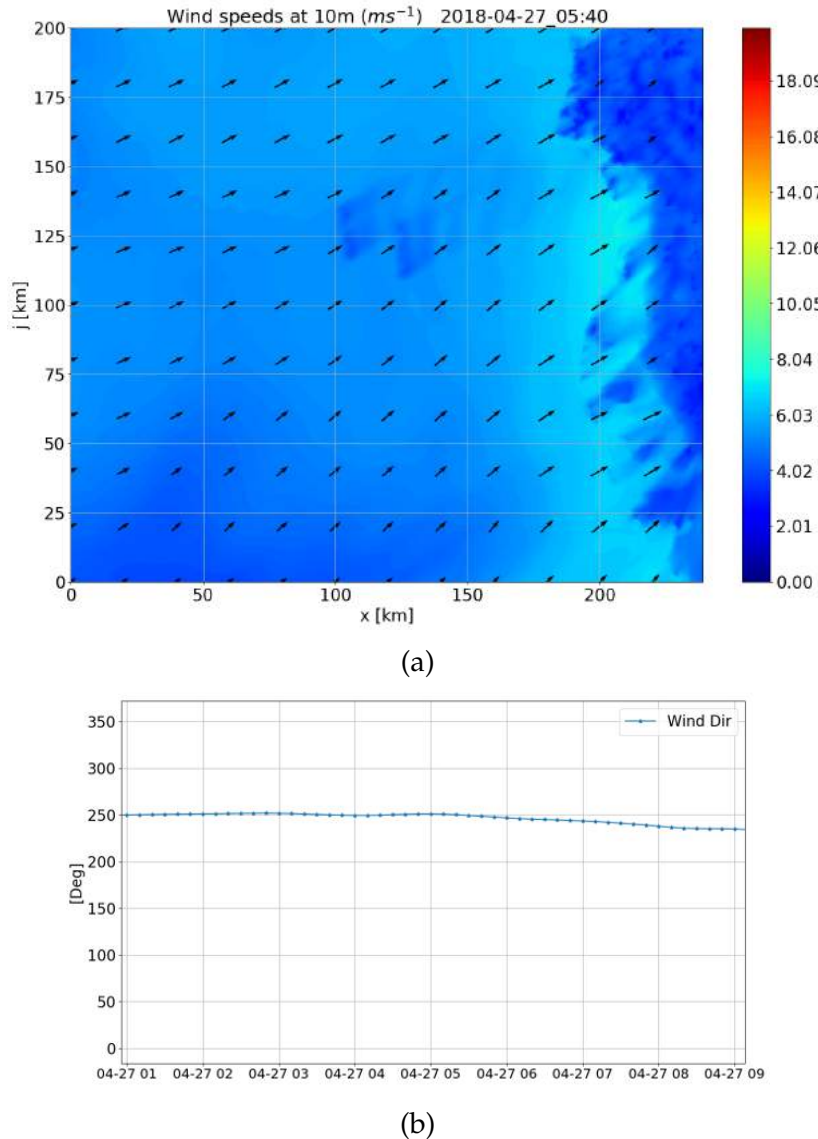


Figure 5.3: Case 5 (2018-04-27 05:40): WRF-EWP wind speed field (a); Variation of WRF-EWP wind direction with time at an upstream undisturbed location - both at 10m above surface.

In Figure 5.3, it can be seen that the simulation shows a decent level of agreement with the satellite SAR image. The simulation is able to capture the wind direction, presence of the wakes, though only WF2 is visible in the SAR image. The region of high wind speeds across most of the western coast of Denmark is captured well. However, the streak-like-looking physical structures do not show up in the WRF-EWP simulation, and also the wind speed range in the high wind speed region along the west coast differ - with the SAR image indicating a higher wind speed range than in the WRF-EWP simulation. The downstream flow presented in this SAR image too, show regions of increased wind speed in comparison to the upstream and free stream flow. This is not the case in the WRF-EWP simulation, which presents the downstream flow as a region of reduced wind speeds. The WRF-EWP simulations show indications of gravity waves downstream of the wind farms, which suggest a stable stratification of the atmosphere.

5.1.2 Fitch Scheme

From Figure 5.4, it can be seen that the simulation shows a good agreement with the satellite SAR image, and the differences with Figure 5.1 for the EWP scheme cannot be identified without a detailed analysis. The wind speed range and wind flow characteristics appear to be very similar as seen in EWP scheme. Also, wakes from neighbouring wind farms of WF1 and WF2 are not present in the WRF-Fitch simulation similar to the WRF-EWP simulation as these neighbouring wind farms have not been parametrised in WRF.

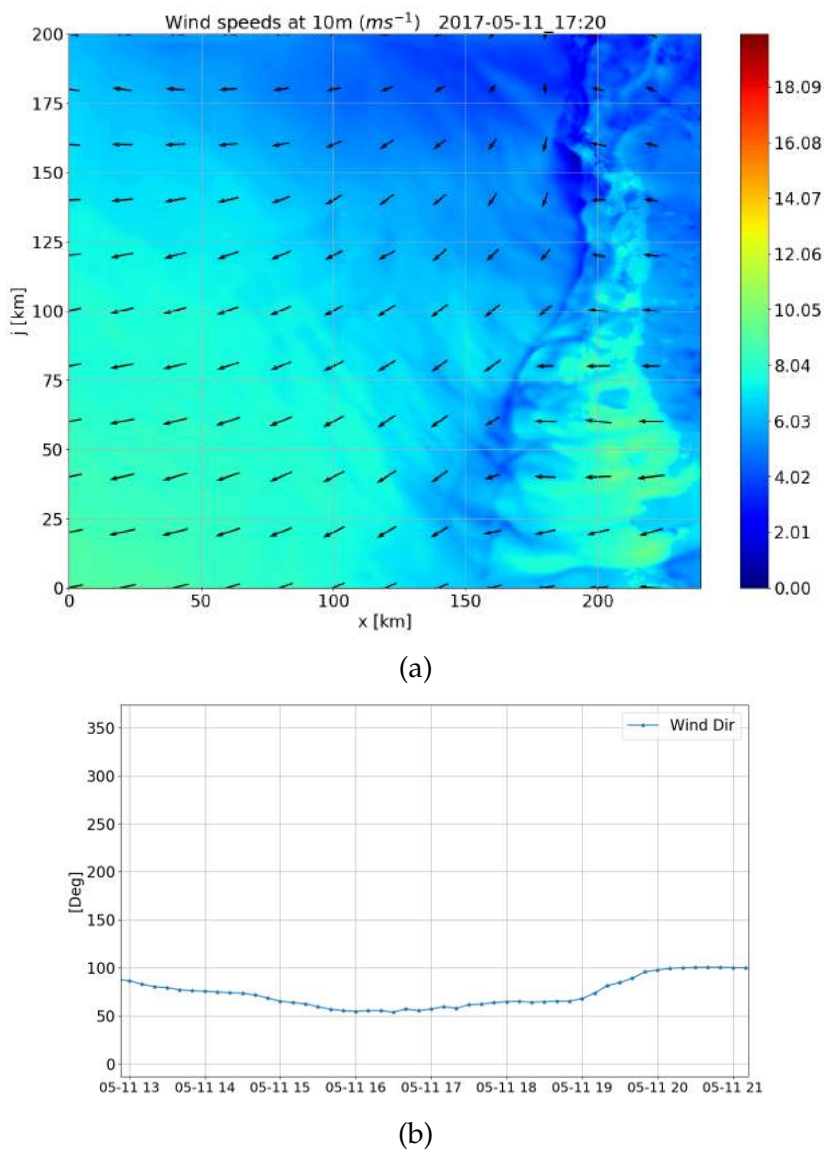


Figure 5.4: Case 3 (2017-05-11 17:20): WRF-Fitch wind speed field (a); Variation of WRF-EWP wind direction with time at an upstream undisturbed location - both at 10m above surface.

In Figure 5.5, it can be seen that the simulation result is very similar to that of the EWP-scheme when comparing the overall wind speed fields. The downstream flow presented in the SAR image, show regions of increased wind speed in comparison to

the upstream and free stream flow. This is also captured in the Fitch scheme, which presents the parts of the downstream flow as increased wind speeds. Though, the southern boundary of the wakes from both wind farms show signs of decreased wind speeds. The WRF-Fitch simulation captures very well the wake region, wind speed increase along portions of the downstream flow, the length and slight turning or meandering of the wake from WF1 (red).

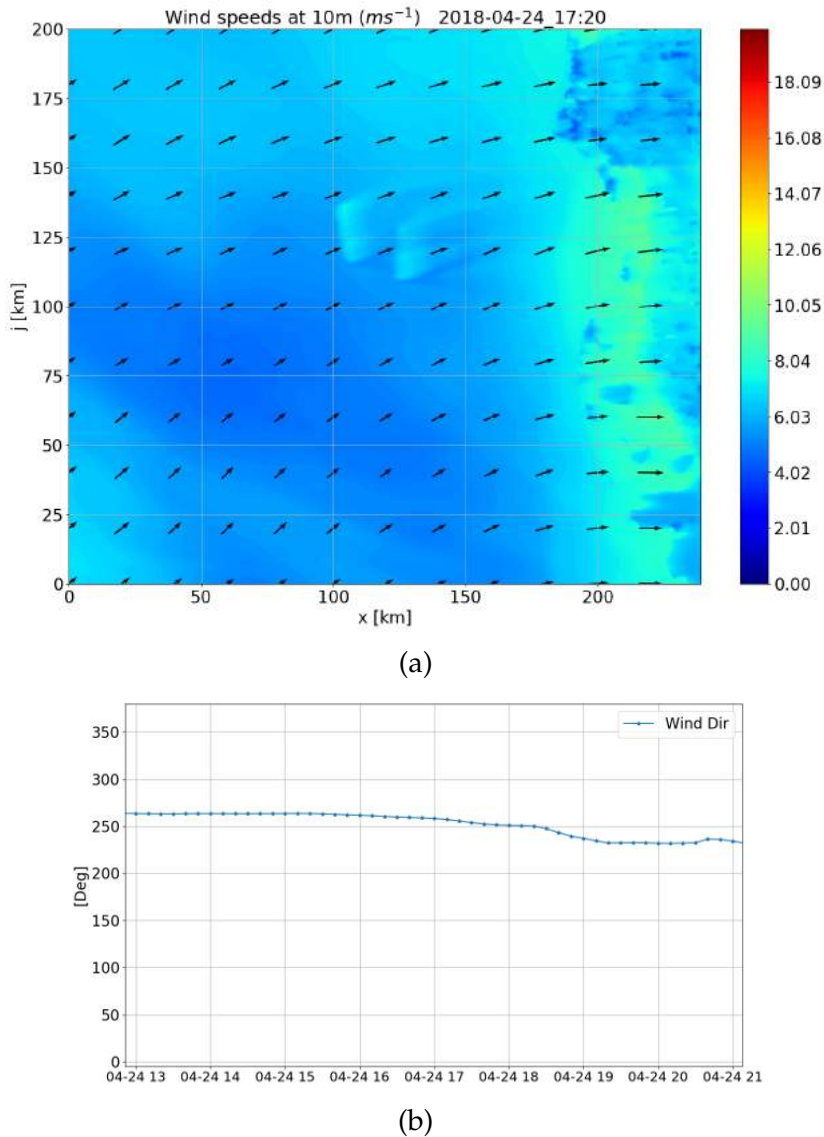


Figure 5.5: Case 4 (2018-04-24 17:20): WRF-Fitch wind speed field (a); Variation of WRF-EWP wind direction with time at an upstream undisturbed location - both at 10m above surface.

In Figure 5.6, it can be seen that the simulation result is very similar to that of the EWP-scheme when comparing the overall wind speed fields. However, like in the EWP-scheme result, the streak-like-looking physical structures do not show up in the WRF-Fitch simulation either. As seen in Figure 5.5, the downstream flow presented in the SAR image, show regions of increased wind speed in comparison to the upstream and free stream flow. This is also captured in the Fitch scheme, which presents the parts of the downstream flow as increased wind speeds. Though, the

WRF-Fitch simulations show indications of gravity waves downstream of the wind farms, which suggest a stable stratification of the atmosphere, this signal is weakened due to the increased wind speeds downstream of the wind farm at 10 m height.

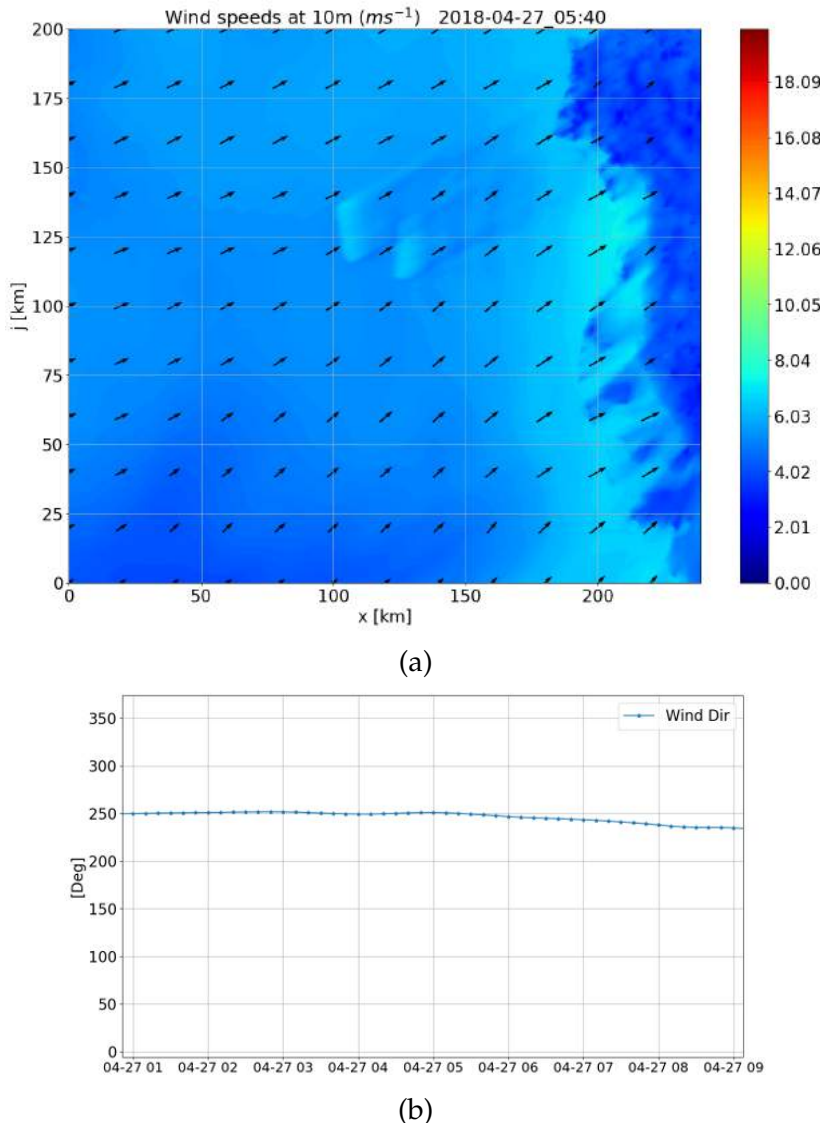


Figure 5.6: Case 5 (2018-04-27 05:40): WRF-Fitch wind speed field (a); Variation of WRF-EWP wind direction with time at an upstream undisturbed location - both at 10m above surface.

5.1.3 Summary and Conclusions

The EWP and Fitch parametrisation schemes with the two wind farms WF1 and WF2 have been explored in WRF. A more detailed analysis of the effect of wind turbines on the modelled flow field is carried out in Chapter 5.2 - on the basis that the preliminary results from both the WRF wind farm parametrisation schemes capture the wind field satisfactorily when compared to satellite images - the patterns in the wind field, wind speed ranges, wind directions, presence of wakes, and the wake pattern and direction.

5.2 Wind Speed, Wake and TKE Field

Chapter 5.2 presents analyses of the wind speed deficit and TKE difference fields using simulations run with and without wind farm parametrisations. As shown in Figure 5.7, 8 wake analysis points (WAP) and 4 undisturbed flow analysis points (UAP) have been identified to assist with identifying and quantifying these wake characteristics:

1. Analysing the disturbed horizontal wind speed flow field at 90 m height.
2. Analysing the vertical profiles of horizontal wind speed difference and TKE difference.
3. Obtaining free stream parameter values to find wind speed, wind direction, and stability.

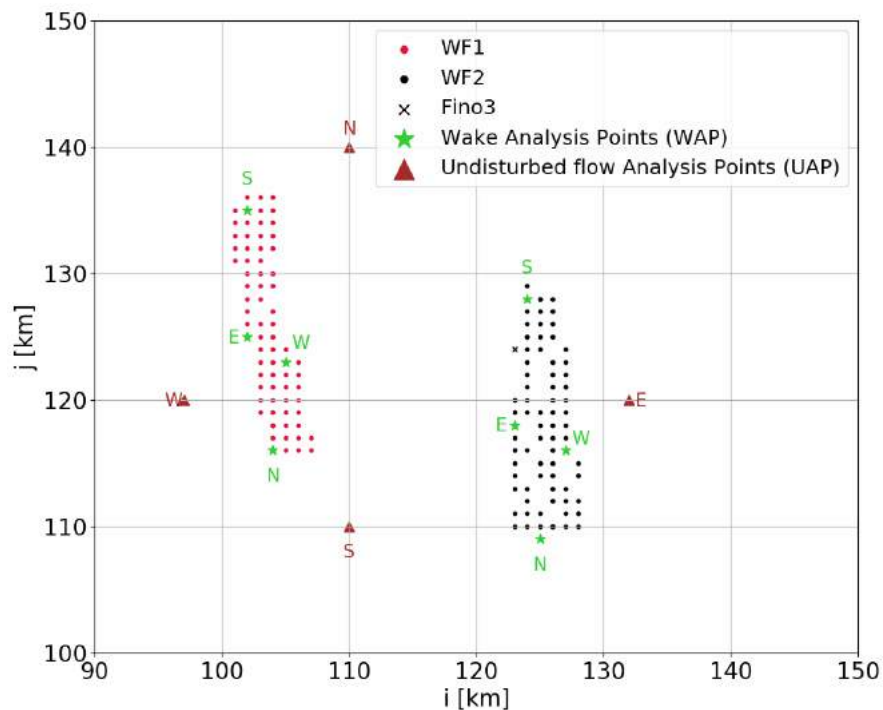


Figure 5.7: Analysis Points used to analyse disturbed wind speed and TKE flow fields, and obtain free stream parameter values.

The WAP shown in Figure 5.7 for each wind farm have an associated direction indication next to them. This indicates which point is used when the incoming flow is in that associated direction (P_0), to identify points along a line through this analysis point (downstream of the flow) at the angle of wind direction, and this line extends up to the boundary of the domain at the same angle. In addition, 20 points upstream are also identified. This gives points upstream and downstream of the flow at the angle of wind direction through the respective analysis points, along which wind speed difference, and TKE difference values are obtained.

The initial wind direction is obtained using an arbitrary point located at $i=80$ km and $j=150$ km, and based on this initial value, the undisturbed flow analysis points

are used to obtain the undisturbed or free-upstream flow wind direction and wind speed. It is this undisturbed wind direction value that is used to draw the line of points.

Wake lengths are determined by obtaining the wind speed difference values between simulations with and without WRF. The wind speed differences along these points, starting from (P_0) are then analysed towards the downstream direction, and the wake length is determined when a threshold value of wind speed deficit is encountered, say at downstream point (P_{40}). The wake length (km) is calculated as the actual distance between these two Cartesian coordinate points (as the grid spacing or resolution of the axes is 1 km).

There are three reasons for choosing different wake analysis points:

1. The wake length to be identified is calculated from the end of the wind farm.
2. As the length and width of the wind farms are unequal, using the would increase the wake length for Northerly and Southerly flows as the length of the wind farms along the N-S is much larger than the width in the E-W direction.
3. Looking at WF2 in Figure 5.7, there are empty spaces larger than others between turbines due to the allocation of turbines to the nearing grid cell in the WRF parametrisations. If there had been complete recovery of wind speed due to different conditions in the atmosphere in these spaces, the wake length determination algorithm could stop there and not count for further downstream flow differences.

The letter indicating the wind direction (see Figure 5.7) is based on the following undisturbed wind direction ranges ¹ (a narrower range is used for N-S flows due to the smaller width of the wind farms as compared to the length):

- S → $240 < \text{Wind Dir} < 300$
- W → $120 \leq \text{Wind Dir} \leq 240$
- N → $60 < \text{Wind Dir} < 120$
- E → $300 \leq \text{Wind Dir} \leq 360 \text{ & } \text{Wind Dir} \leq 60$

The letters "a" and "b" in Figure 5.7 are used to identify the analysis starting (upstream) and ending (downstream) points for WF1, and "c" and "d" for WF2 respectively. In all figures of vertical cross section of either wind speed difference or TKE difference along wake length presented in the following chapters, these starting upstream and ending downstream point identifiers have been marked close to the x-axis.

The reason for this automated method of detecting points along the wake length is that though individual cases are being analysed at first, to quantify the effect of stability on wakes, a larger set of simulations are used. To quantify the effect of stability on wakes, all 5 cases with complete 24 hour period of 10-minute resolution each are used, which results in 720 time stamps. Manually identifying the wind direction, adjusting the direction and positioning of the line of the points for such a large sample would be time-consuming. Hence, though wakes may turn or

¹wind direction from True North

deficits along the perpendicular sections of the wakes may vary, this method is time-efficient and can be applied to a data set of more than just 720 modelled time stamps as well.

The rotor areas of the wind farms have been highlighted by a red box in each plot. The hub heights of each wind farm are marked in horizontal dashed red lines, and the vertical extent of the rotor blades in horizontal dashed black lines.

Chapter 5.2.1 presents the results from the WRF-EWP and WRF-Fitch simulations for Cases 1, 2, and 3. The results include modelled 90 m wind speed fields, 90 m wind speed difference with and without the wind farms, profiles of wind speed difference and TKE difference with and without wind farms along wake length points for each wind farm. Chapter 5.2.2 presents the same but for the Fitch scheme. Cases 1, 2, and 3 are presented here as they bring out important characteristics of the two schemes and the different stability conditions as obtained from the WRF modelled parameters presented in Table 5.3 in Chapter 5.3.

The results and analysis of Cases 4 and 5 for both EWP and Fitch scheme which show presence of wake lengths between 60 km and 100 km are presented in Appendix A.

5.2.1 EWP scheme

Case 1

Presented in Figures 5.8 and 5.9, are the horizontal wind speeds at 90 m when the wind farms are parametrised, and horizontal wind speed difference at 90 m with and without the wind farms using the EWP scheme for case 1 (2016-09-13 16:20) respectively.

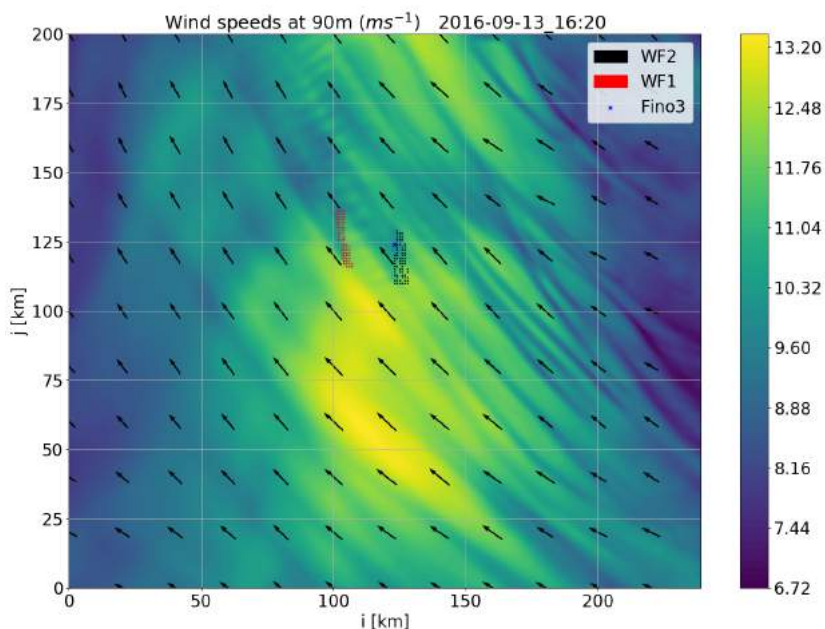


Figure 5.8: Case 1 (2016-09-13 16:20) : WRF-EWP modelled wind speeds at 90 m with wind farms.

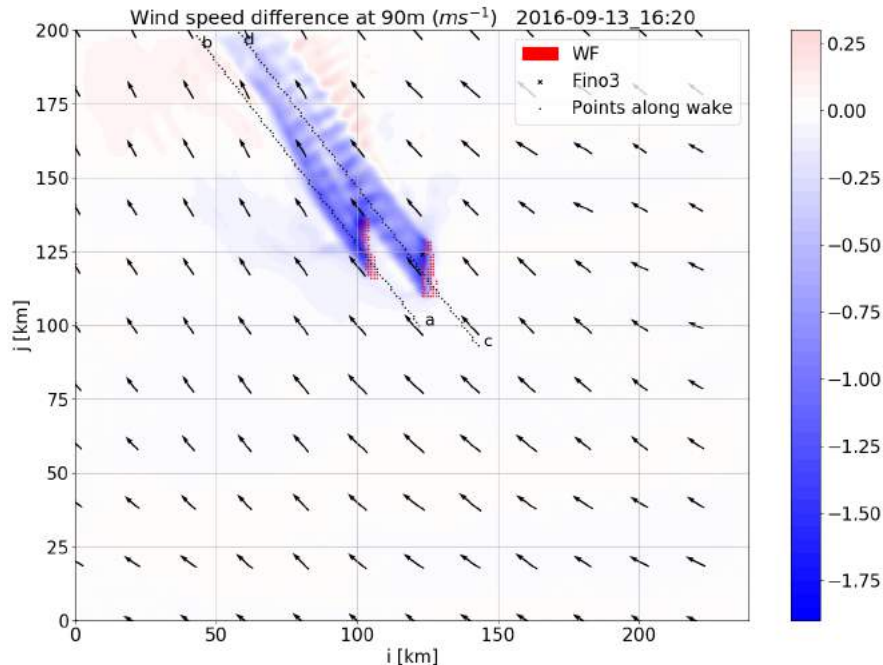


Figure 5.9: Case 1: WRF-EWP modelled wind speed difference at 90 m
- with and without wind farms.

Figure 5.8 shows a large variation in the wind speeds across the domain, and wakes are visible along the downstream direction from the wind farm. As expected, in Figure 5.9 the wind speed deficit is downstream along the wind direction. The wind farms are highlighted in red, and the wind speed deficit region extend until the boundary of the domain. The wakes from WF1 are turning to the right, but the extent of wake turning from WF2 is not as clear, which could be because the wake from WF1 is on top.

Gravity waves are visible in both figures, with stronger gravity waves along the WF2 wake length. Roy et al. (2010) [37] have studied the effect a wind farm may have on sea surface temperature, which can potentially influence the stability conditions. The presence of gravity waves in the wake of the wind farm suggests that the atmosphere in the wind farm is stably stratified. A region of increased wind speeds outside the wake region is also present some distance downstream of the wind farms.

Figure 5.10 presents for Case 1 the vertical profile of wind speed difference with and without wind farms using the EWP scheme, along the points identified in the wake region for WF1 (a) and WF2 (b). It can be seen, that the wind speed deficit is highest in the region just downstream of the turbine rotors, which is in agreement with what is expected as the farm region is where the KE is extracted from the air, causing a deceleration of the wind right downstream to it.

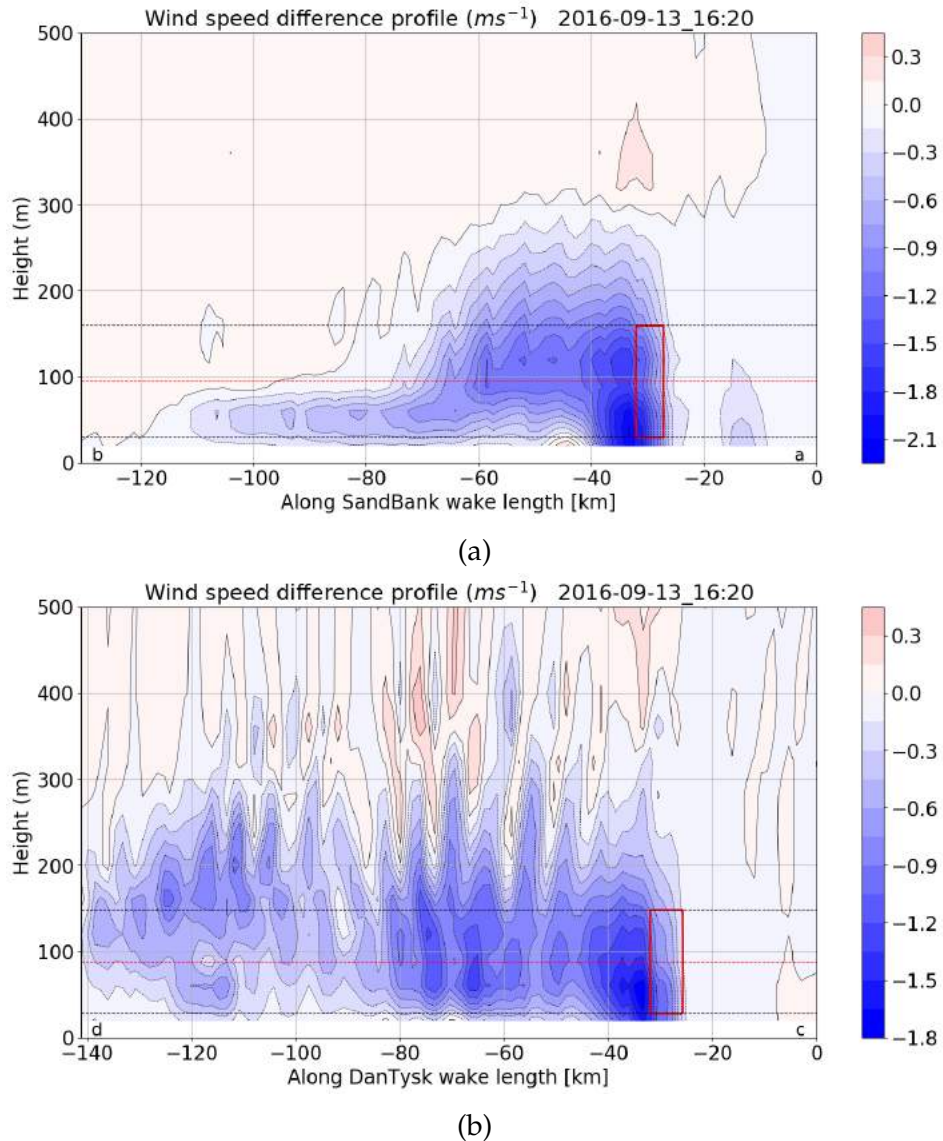


Figure 5.10: Case 1: Profile of WRF-EWP modelled wind speed difference with and without wind farms along wake length points of WF1 (a) and WF2 (b).

In Figure 5.10a, the wind speed difference along WF1 extends up to a vertical height of 300 m for approximately 30 km downstream, after which this vertical column where the wind speed difference is negative reduces to near the hub height. This is a consequence of the wake turning away from the identified points along the line based on which the wind speeds are obtained for the vertical layers. However, the wind speed deficits below hub height are prominent up - with a wind speed deficit around 0.3 ms^{-1} at approximately 70-80 km downstream from the end edge wind farm is observed.

In Figure 5.10b, the wind speed difference along WF2 extends up to an average vertical height of 300 m for the entire wake length downstream of the wind farm, but varying across this distance. The presence of gravity waves is highlighted in this plot by the periodical positive and negative difference around the 300 m height along the downstream distance of the wake.

Similarly, Figure 5.11 presents for Case 1 the vertical profile of TKE difference with and without wind farms using the EWP scheme, along the points identified in the wake region for WF1 (a) and WF2 (b). It can be seen, that there is a decreased TKE below the hub height within the wind farm rotor region which extend to different distances downstream for both wind farm, and a gradually increasing TKE in the vertical observed above the hub height. This is in accordance with what Volker et al. (2015) [11] observed.

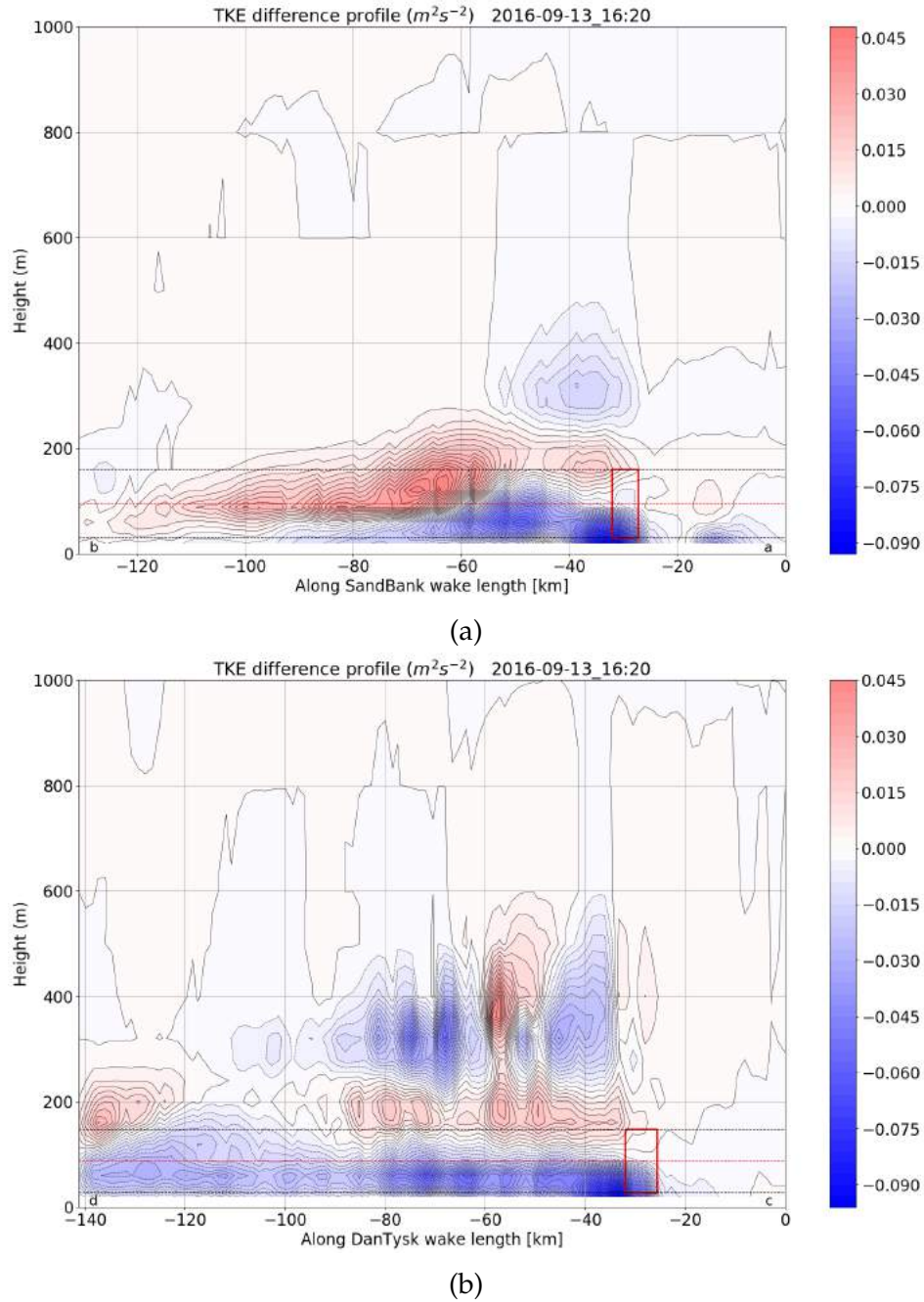


Figure 5.11: Case 1: Profile of WRF-EWP modelled TKE difference with and without wind farms along wake length points of WF1 (a) and WF2 (b).

In Figure 5.11, the turning of the wake from WF1 (a), and strong gravity waves in

the wake region of WF2 (b), are again visible in the TKE plots. Due to the wake turning, the TKE along the entire wake length is not captured for WF1. For WF2 (b) however, due to stable conditions, the TKE deficit also extends up to the domain boundary as highlighted downstream by "d" (as does the wind speed deficit).

Case 2

Presented in Figures 5.12 and 5.13, are the horizontal wind speeds at 90 m when the wind farms are parametrised, and horizontal wind speed difference at 90 m with and without the wind farms using the EWP scheme for Case 2 (2016-11-02 08:20) respectively.

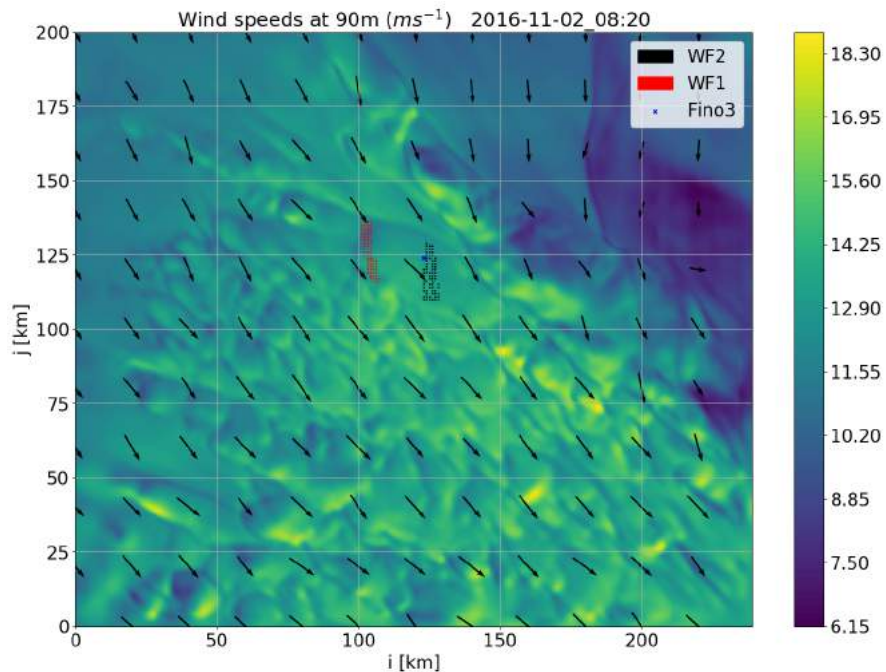


Figure 5.12: Case 2 (2016-11-02 08:20) : WRF-EWP modelled wind speeds at 90 m with wind farms.

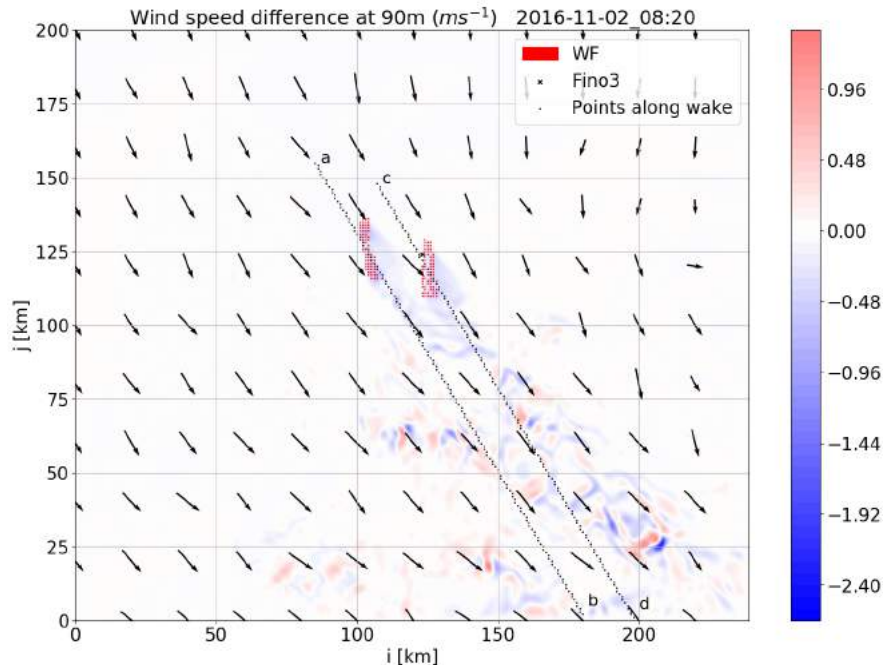


Figure 5.13: Case 2: WRF-EWP modelled wind speed difference at 90 m - with and without wind farms.

Figure 5.12 shows a large variation in the wind speeds across the domain, with no wakes around the wind farm, but visible open cells under very unstable conditions. Open cells are characterised by highly fluctuating mean wind fields (wind speed and direction) [47] [48]. With Northerly flows, the wind direction also seems to vary slightly over land and water.

Figure 5.13 shows a rather small extent of wind speed deficit downstream of the wind farms, which indicates an unstable stratification of the atmosphere. However, in regions extending beyond the flow downstream of the wind farms, parcels of fluctuating wind speeds are present, which happen in the presence of open cells. This is likely related to the WRF-modelling of the phase of open cell wind fields, because if these fluctuations are averaged over the area, it is less-likely that there is a deviation from zero wind speed.

Figure 5.14 presents for Case 2 the vertical profile of wind speed difference with and without wind farms using the EWP scheme, along the points identified in the wake region for WF1 (a) and WF2 (b). It can be seen, that the wind speed deficit is high in the region of or just downstream of the turbine rotors, which is in agreement with what is expected as the farm region is where the KE is extracted from the air, causing a deceleration of the wind right downstream to it.

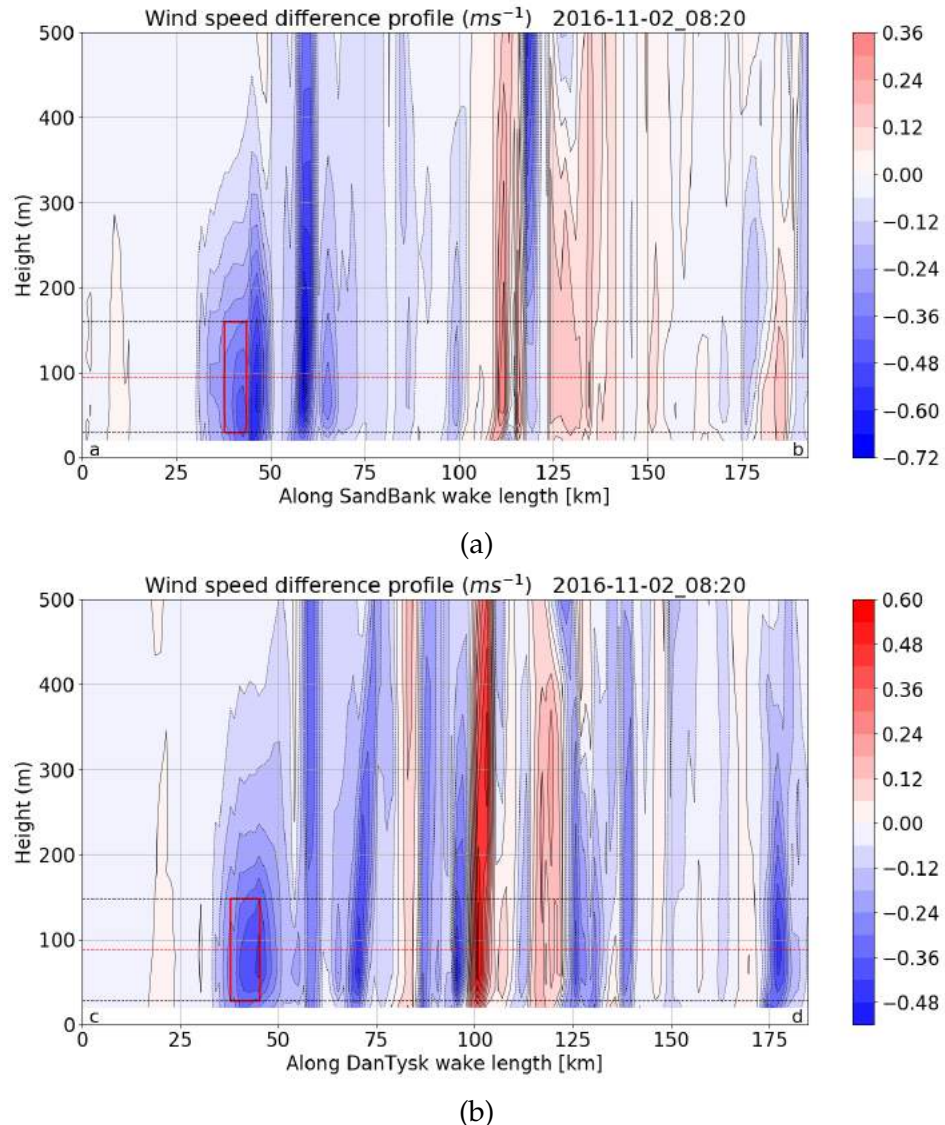


Figure 5.14: Case 2: Profile of WRF-EWP modelled wind speed difference with and without wind farms along wake length points of WF1 (a) and WF2 (b).

This indication of unstable conditions - which involves a high amount of convective flow, these wind speed deficits do not propagate much downstream. The wind speed recovers very fast, however, other regions of increased and decreased wind speeds are visible. However, as seen in Figure the wind speed difference along WF1 (a), a region of decreased wind speed after the wake recovery exists, and a region of increased wind speed downstream of WF2 (b) - both extend into the vertical direction, indicating the effect of mixing cause by convection in unstable conditions.

Similarly, Figure 5.15 presents for Case 2 the vertical profile of TKE difference with and without wind farms using the EWP scheme, along the points identified in the wake region for WF1 (a) and WF2 (b).

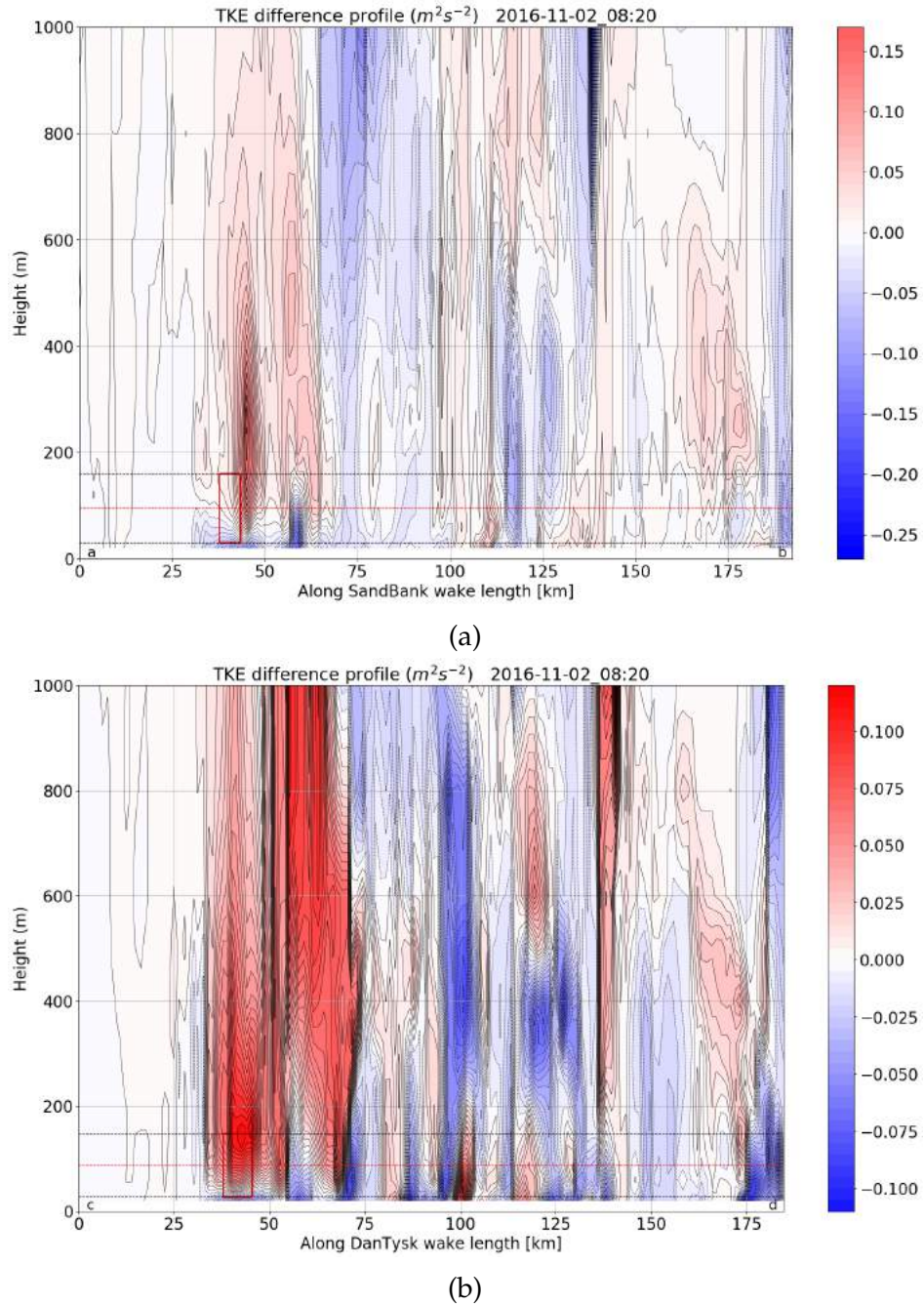


Figure 5.15: Case 2: Profile of WRF-EWP modelled TKE difference with and without wind farms along wake length points of WF1 (a) and WF2 (b).

In Figure 5.15a, it can be seen that there is a decreased TKE below the hub height within the WF1 rotor region, and a gradually increasing TKE in the vertical up to 1 km is observed above the hub height, but this effect does not propagate downstream. However in Figure 5.15b for WF2, a decreased TKE is at a much lower level than the hub height of the wind farm, with increased TKE for most part of the rotor area, and well above the wind farm - extending up to 1 km. Lundquist et al. (2012) [12] found the TKE differences to extend up to nearly 600 m under stable conditions using the Fitch scheme. Therefore, the vertical extent of TKE difference can be attributed to mixing in convective flow due to unstable conditions again.

Case 3

Presented in Figures 5.16 and 5.17, are the horizontal wind speeds at 90 m when the wind farms are parametrised, and horizontal wind speed difference at 90 m with and without the wind farms using the EWP scheme for Case 3 (2017-05-11 17:20) respectively.

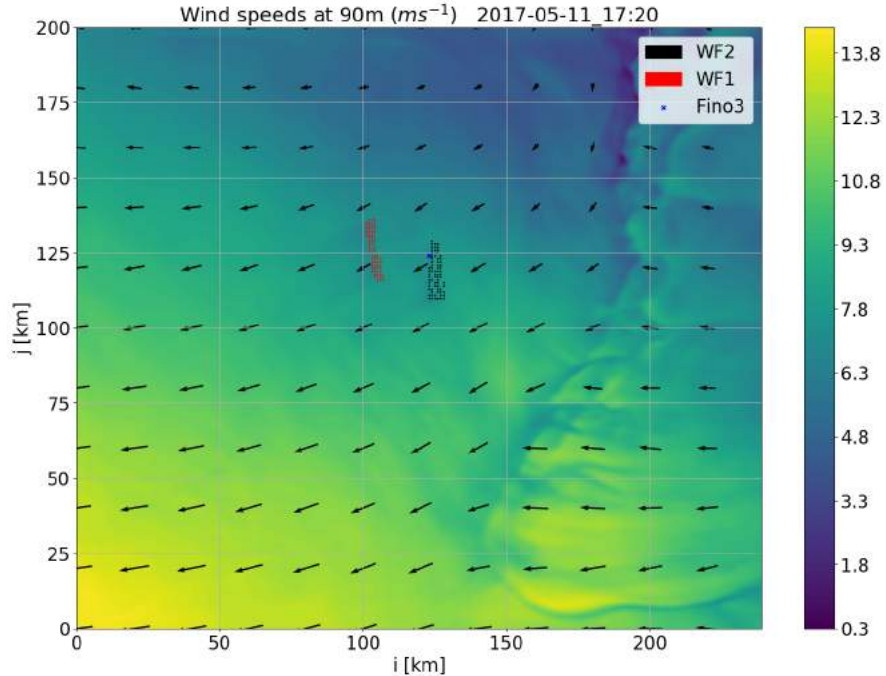


Figure 5.16: Case 3 (2017-11-05 17:20) : Wind speeds at 90 m with wind farms.

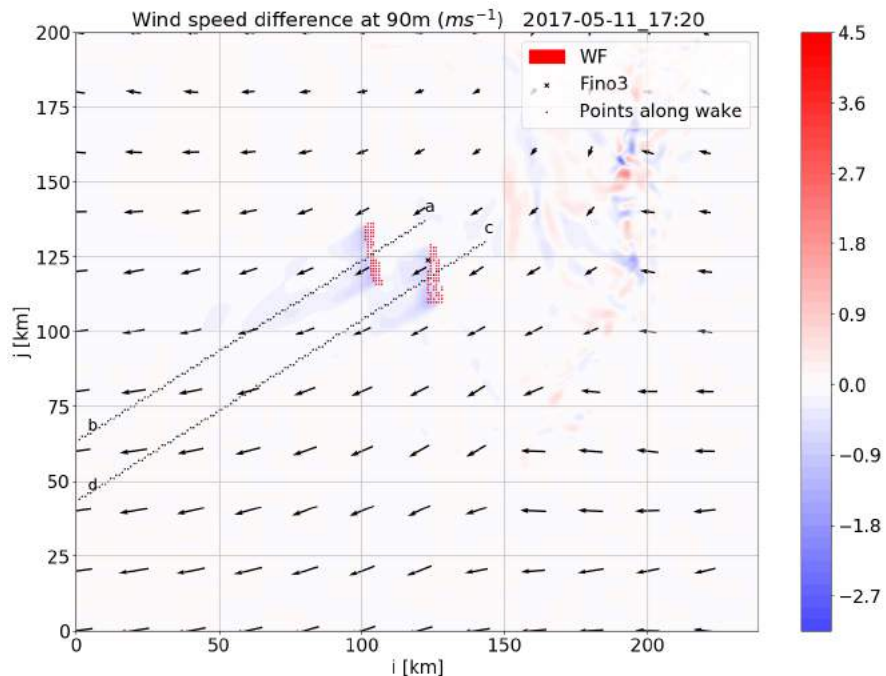
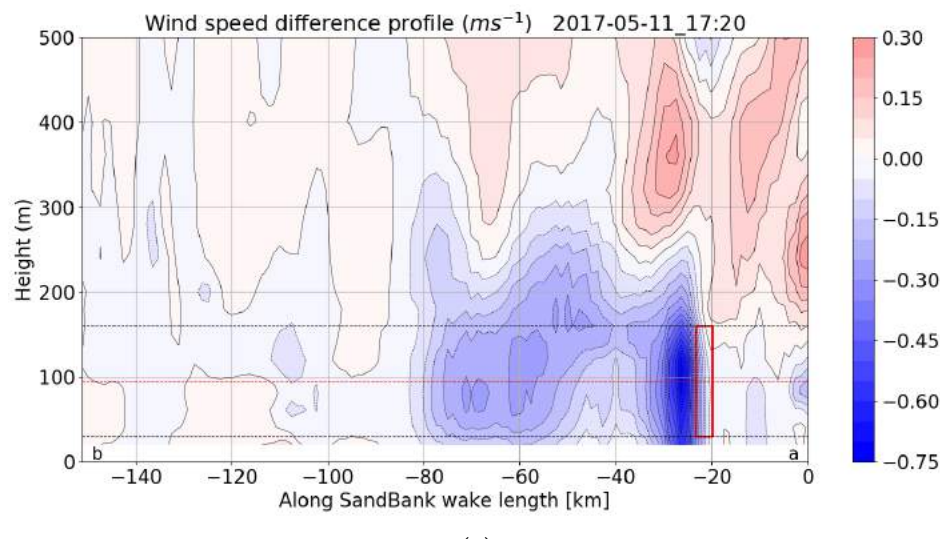


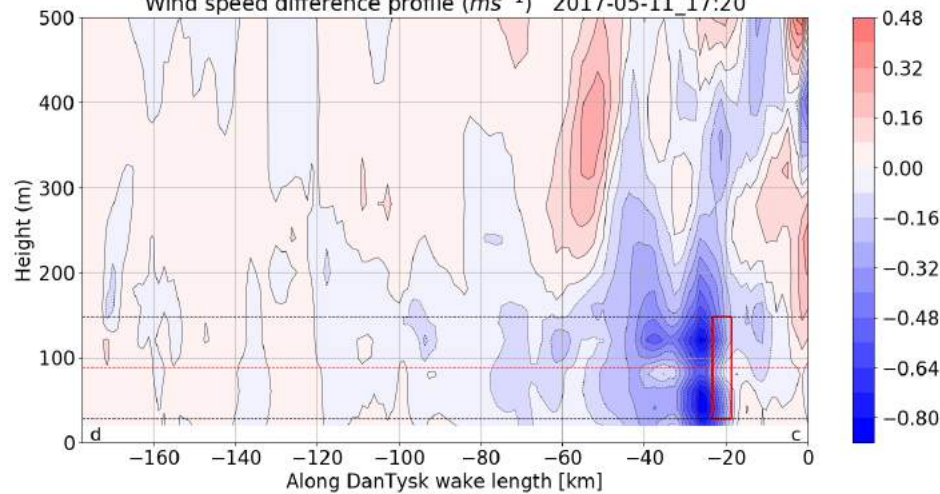
Figure 5.17: Case 3: Wind speed difference at 90 m - with and without wind farms.

Figure 5.16 shows mild wakes along the downstream direction from the wind farm. In Figure 5.17 the wind speed deficits are visible downstream along the wind direction. Parcels of increased and decreased wind speeds are visible upstream of the wind farms, closer to the west coast and over land. It is due to magnitude of these parcels of increased and decreased wind speeds upstream, that the wakes from the wind farm are not clearly visible and are masked due to the magnitudes.

Figure 5.18 presents for Case 3 the vertical profile of wind speed difference with and without wind farms using the EWP scheme, along the points identified in the wake region for WF1 (a) and WF2 (b). It can be seen again, that the wind speed deficit is highest in the region just downstream of the turbine rotors.



(a)



(b)

Figure 5.18: Case 3: Profile of wind speed difference with and without wind farms along wake length points of WF1 (a) and WF2 (b).

In Figure 5.18a, the wind speed difference along WF1 extends up to a vertical height of 250-300 m for approximately 60 km downstream. There is also an increased wind speed a certain height above and upstream of the wind farm WF1, which has not

been encountered in the previous simulations. The wind speed difference along WF2 in Figure 5.18b does not extend as much as in WF1, but a region of increased wind speeds around 300 m height upstream and downstream of WF2 is also observed.

Similarly, Figure 5.19 presents for Case 3 the vertical profile of TKE difference with and without wind farms using the EWP scheme, along the points identified in the wake region for WF1 (a) and WF2 (b).

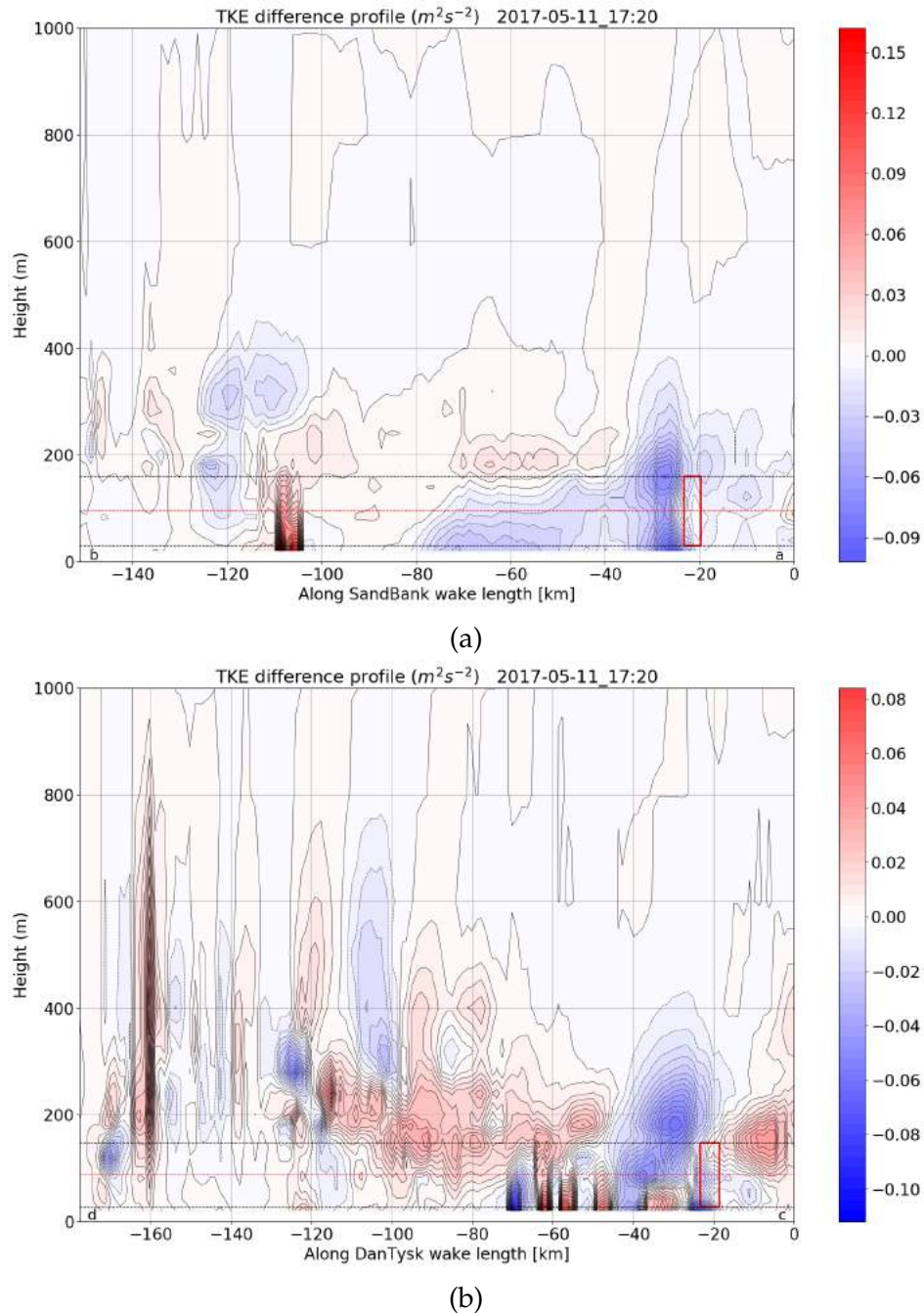


Figure 5.19: Case 3: Profile of TKE difference with and without wind farms along wake length points of WF1 (a) and WF2 (b).

It can be seen, that there is a decreased TKE all along the rotor region for both WF1

(a) and WF2 (b). In the case of WF1, this TKE deficit propagates along the rotor distance nearly 60 km, with a small parcel of increased TKE above the rotor height some distance downstream. However in the case of WF2 (b), this TKE deficit does not propagate similarly. The TKE difference for WF2 downstream below hub height shows alternating patterns between decreased and increased TKE, with increased TKE upstream of the rotors above hub height as well. This could be indicative of a near-neutral stable atmospheric stratification, wherein the TKE differences do not propagate as much as in stable conditions, but also are not very short-lived as in convective unstable conditions. The stability condition from the simulations is computed later in Chapter 5.3, however, in situ measurements of TKE are needed to substantiate this theory.

5.2.2 Fitch scheme

The results between the EWP and Fitch scheme differ as expected based on the literature in the following ways, and the features of the results from the Fitch scheme are presented for the 3 cases below:

- The magnitude of wind speed reduction is larger in the Fitch scheme.
- The TKE change due to the presence of the wind farm shows up as a sharp increase restricted to the rotor area, which is not the case in the EWP scheme.
- In the EWP scheme, there is a decreased TKE below the hub height of the turbines rotor area, and an increase TKE above it. The TKE differences are not as large in the EWP scheme, and there is a propagation of the TKE in the downstream direction, whereas in the Fitch scheme the TKE propagation downstream is negligible.
- There are increased wind speeds below the rotor area as seen in the Fitch scheme, whereas in the EWP scheme there are decreased wind speeds below the rotor area.

Case 1

Presented in Figures 5.20 and 5.21, are the horizontal wind speeds at 90 m when the wind farms are parametrised, and horizontal wind speed difference at 90 m with and without the wind farms using the Fitch scheme for Case 1 (2016-09-13 16:20) respectively.

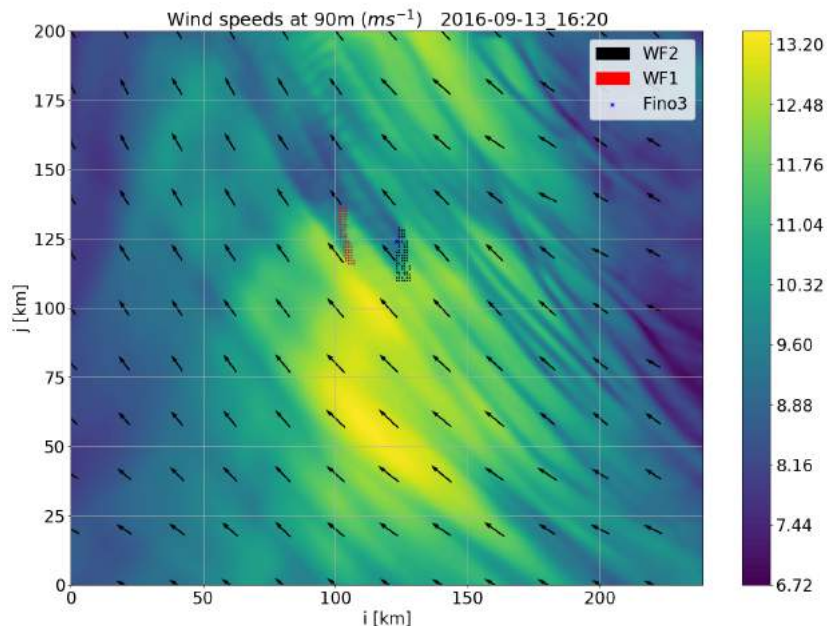


Figure 5.20: Case 1 (2016-09-13 16:20) : WRF-Fitch modelled wind speeds at 90 m with wind farms.

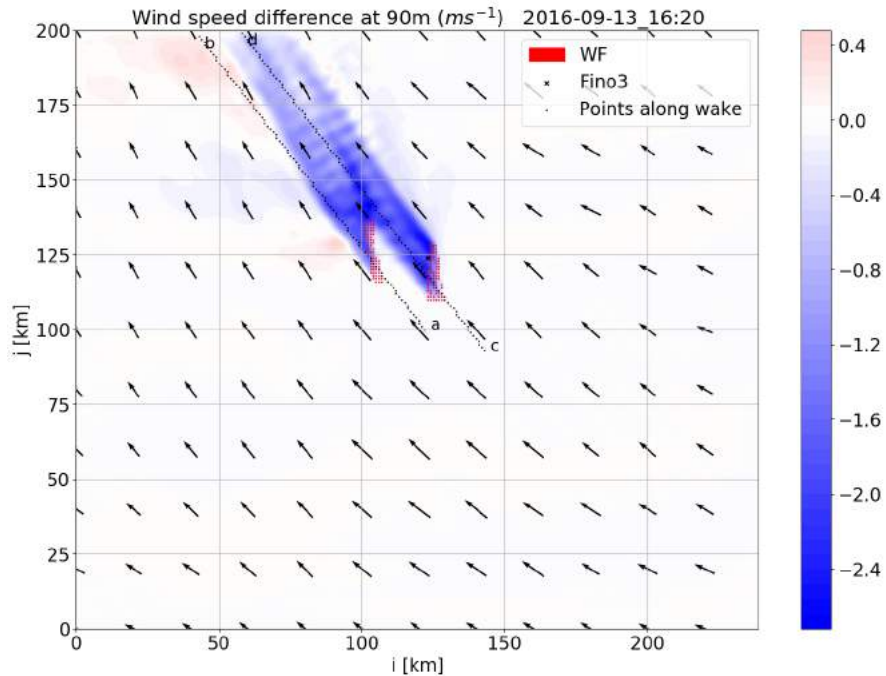


Figure 5.21: Case 1: WRF-Fitch modelled wind speeds difference at 90 m - with and without wind farms.

Figure 5.20 shows the same wind speed field pattern as seen in Figure 5.8 from the WRF-Fitch simulation. The only difference between a larger wind speed deficit is noticeable in this WRF-Fitch figure. Figure 5.21 confirms this with the maximum wind speed deficit in this WRF-Fitch result being approximately -2.7 ms^{-1} , whereas in the result from WRF-Fitch, the maximum wind speed deficit is approximately -1.85 ms^{-1} . Gravity waves are also present in the WRF-Fitch simulation.

Figure 5.22 presents for Case 1 the vertical profile of wind speed with and without wind farms using the Fitch scheme, along the points identified in the wake region for WF1 (a) and WF2 (b).

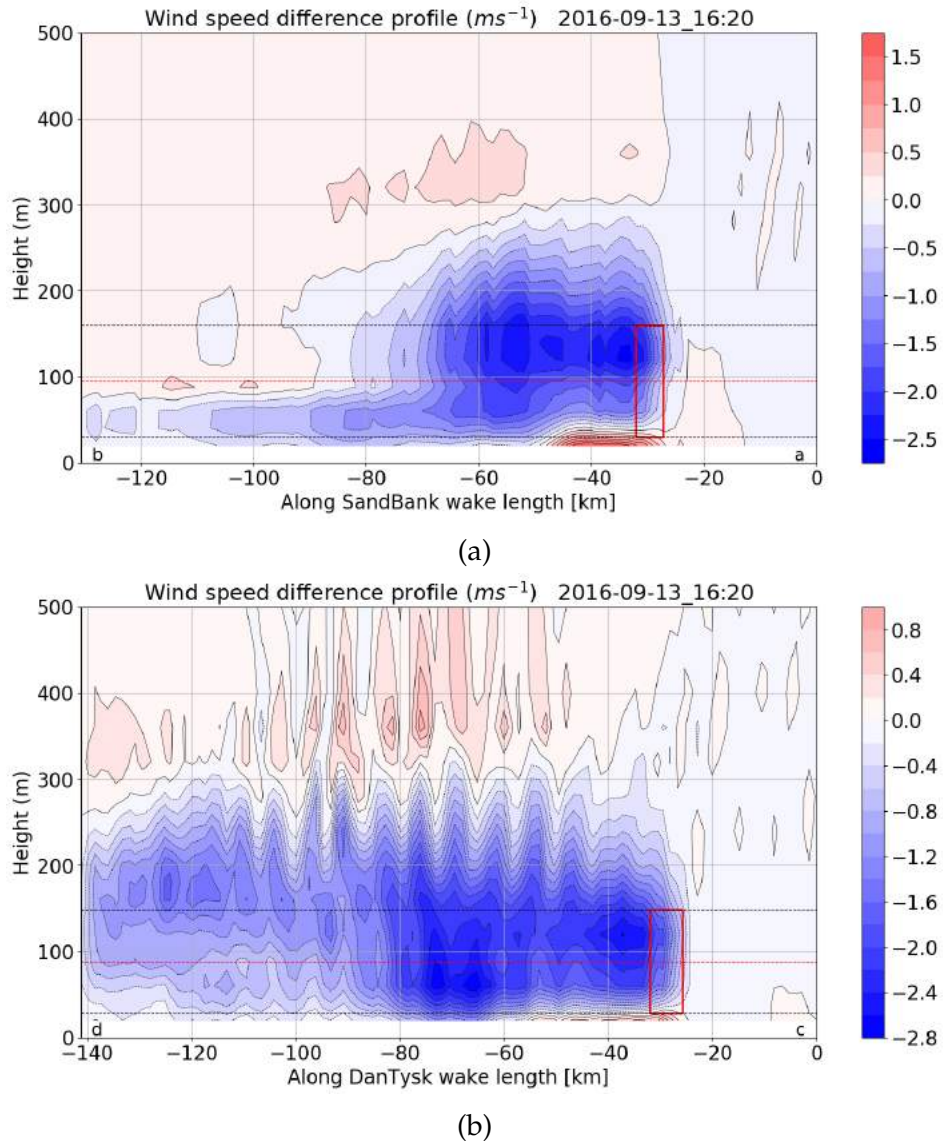


Figure 5.22: Case 1: Profile of WRF-Fitch modelled wind speed difference with and without wind farms along wake length points of WF1 (a) and WF2 (b).

It can be seen, that the flow along the wake length does not deviate from the WRF-Fitch scheme simulation. However, two significant differences to highlight here are:

1. The maximum wind speed deficit for WF1 (a) is approximately -2.5 ms^{-1} and that for WF2 (b) is approximately -2.8 ms^{-1} , which is higher than the values observed in the WRF-Fitch simulation for the same case.
2. From the wind farms to a certain distance downstream, there are increased wind speeds below the rotor areas for both wind farms, with an increment magnitude of between 0.7 to 1.5 ms^{-1} , but this is absent in the EWP scheme.

This increase in wind speed below the rotor areas explains the increased wind speeds in the downstream flow at 10 m as seen in the WRF-Fitch simulations in Figures 5.4, 5.5, and 5.6. Also visible is an increased wind speed upstream of WF1 (a).

Similarly, Figure 5.23 presents for Case 1 the vertical profile of TKE difference with and without wind farms using the Fitch scheme, along the points identified in the wake region for WF1 (a) and WF2 (b).

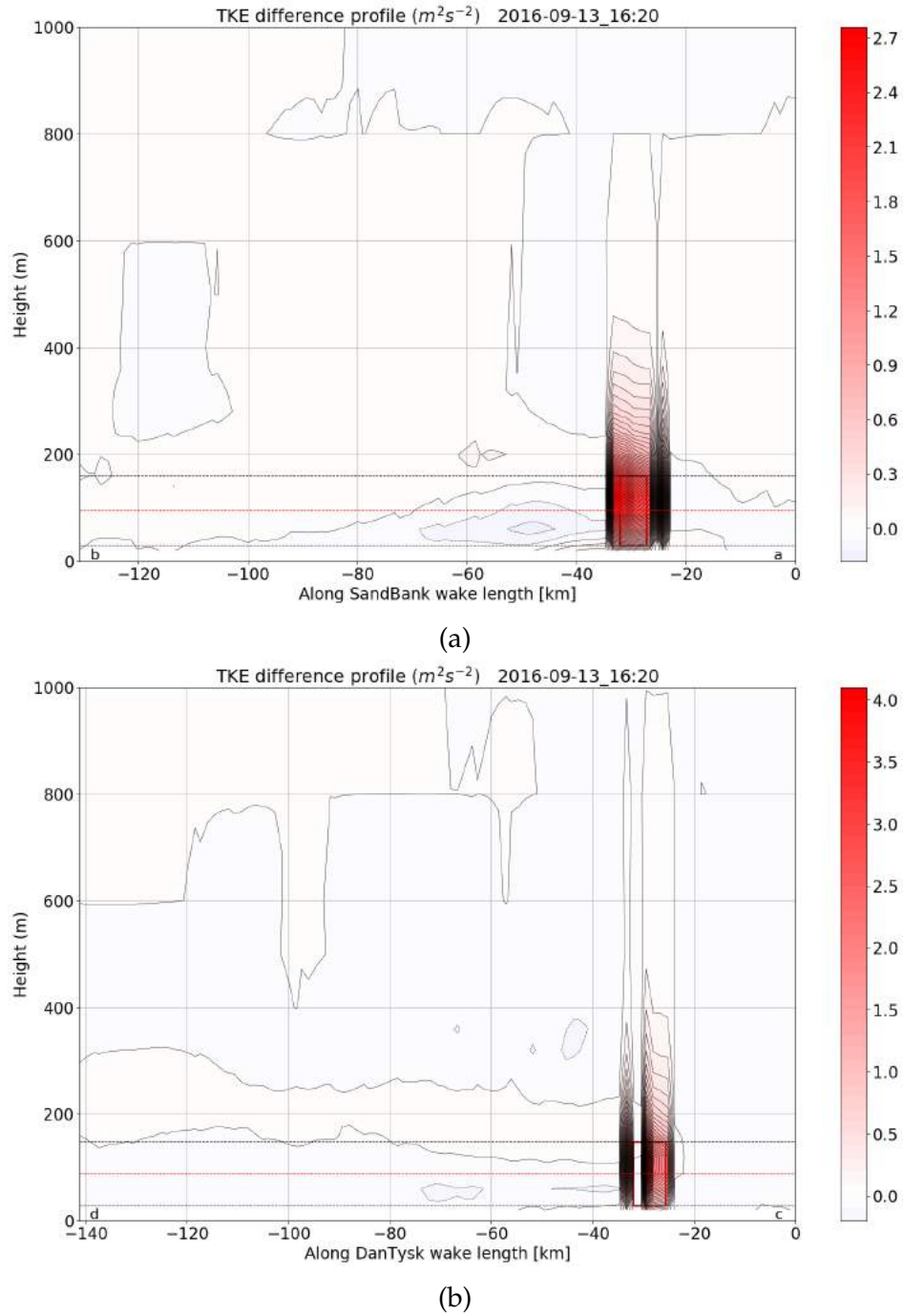


Figure 5.23: Case 1: Profile of WRF-Fitch modelled TKE difference with and without wind farms along wake length points of WF1 (a) and WF2 (b).

It can be seen, that there is a very sharp increase in the TKE in the wind farm rotor area for both wind farms, with a decreasing magnitude in the vertical. Though there is decreased TKE downstream of the wind farms, the magnitude of this decrease is too small as compared to the increase in TKE, such that the decreased TKE regions

are not clearly visible. This result is expected, as the TKE in the Fitch scheme is generated by a source term that dominates the turbulence shear production from the PBL scheme as seen in Figure 3.2.

Case 2

Presented in Figures 5.24 and 5.25, are the horizontal wind speeds at 90 m when the wind farms are parametrised, and horizontal wind speed difference at 90 m with and without the wind farms using the Fitch scheme for Case 2 (2016-11-02 08:20) respectively.

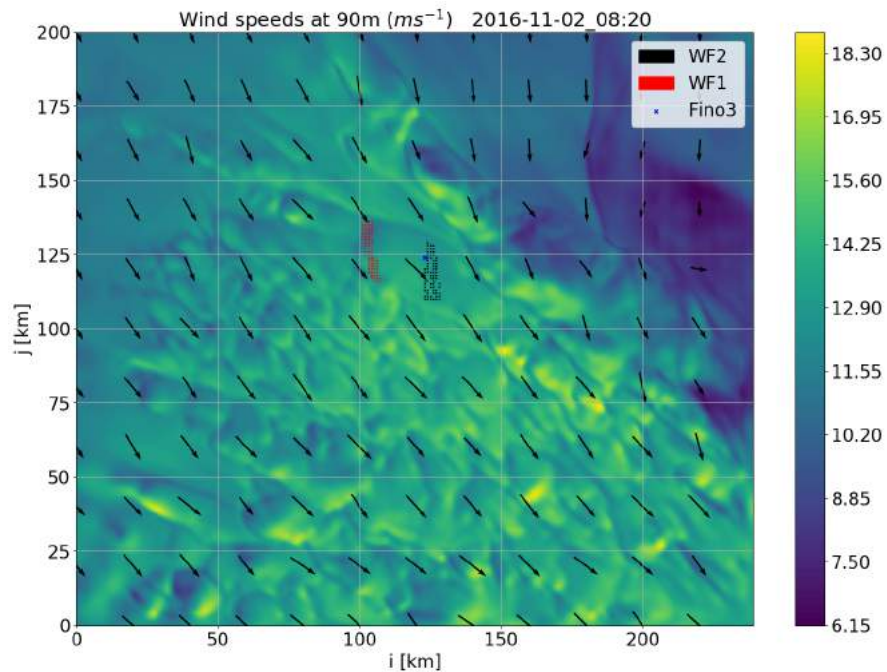


Figure 5.24: Case 2 (2016-11-02 08:20) : WRF-Fitch modelled wind speeds at 90 m with wind farms.

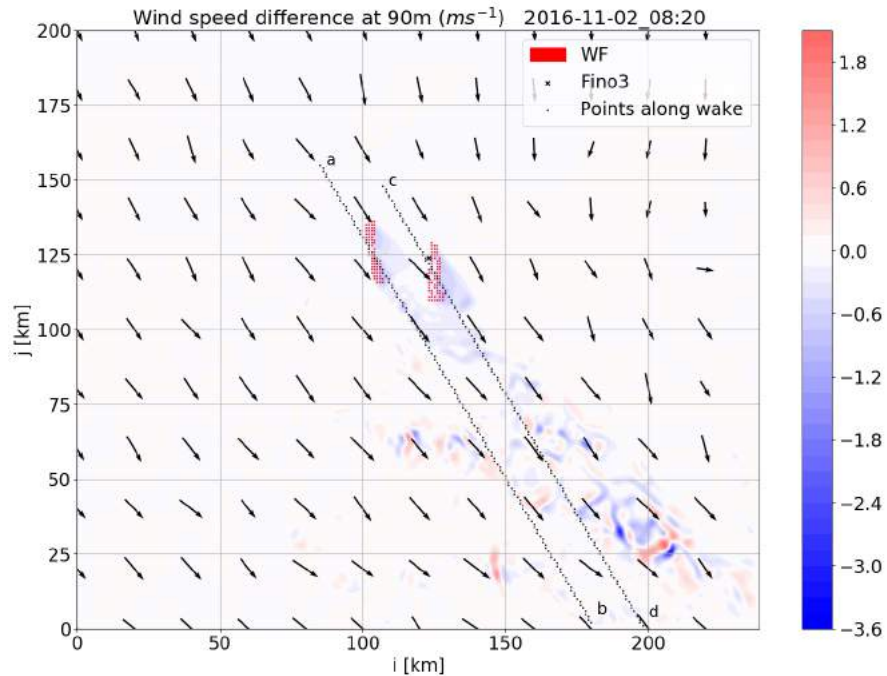


Figure 5.25: Case 2: WRF-Fitch modelled wind speeds difference at 90 m - with and without wind farms.

Figure 5.24 shows no wakes around the wind farm, but visible open cells under very unstable conditions. The difference between the modelled wind speed field is not very different from that of the WRF-Fitch simulation.

Figure 5.25 shows a rather small extent of wind speed deficit downstream of the wind farms, which confirms an unstable stratification of the atmosphere. This too shows very similar patterns as seen in the WRF-Fitch simulation. As seen in Case 1 of WRF-Fitch, here too the wind speed differences are much larger than those observed in the WRF-Fitch simulation.

Figure 5.26 presents for Case 2 the vertical profile of wind speed with and without wind farms using the Fitch scheme, along the points identified in the wake region for WF1 (a) and WF2 (b).

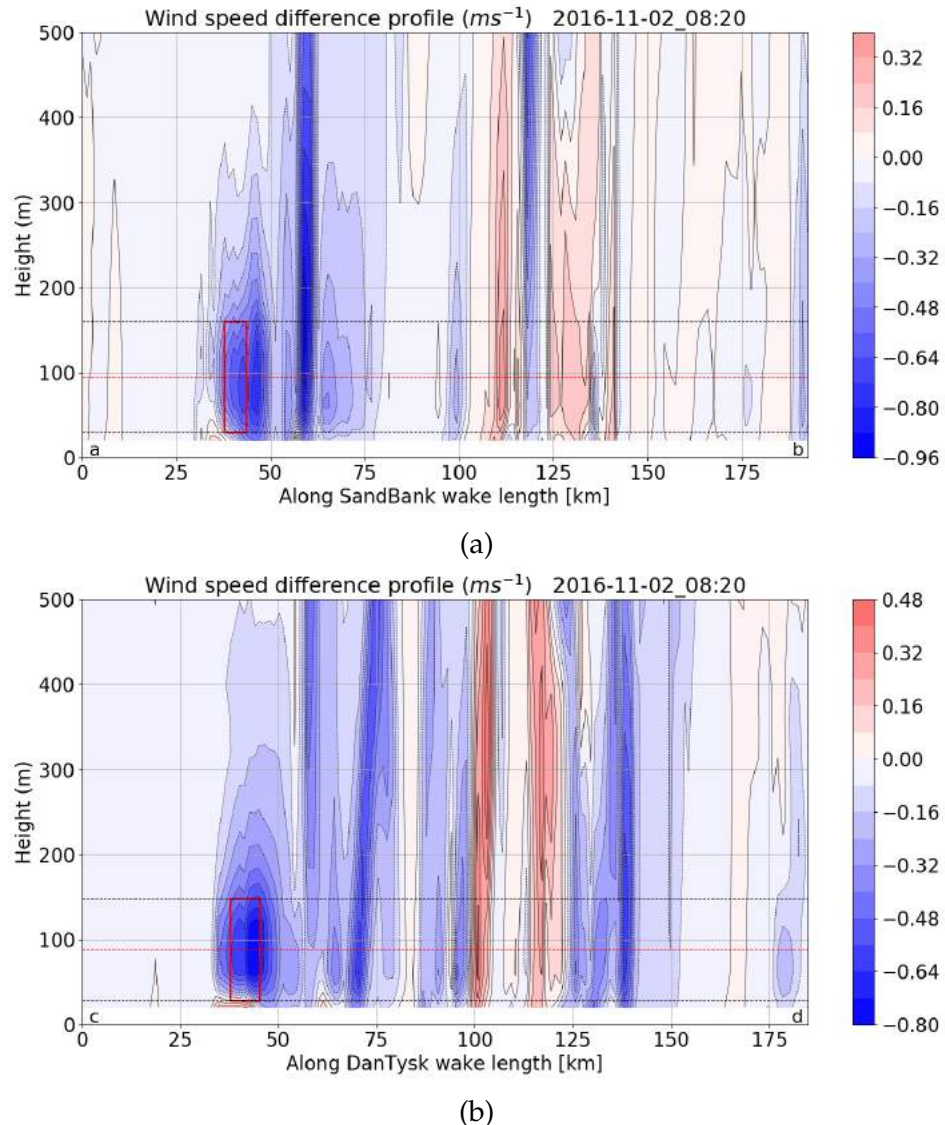


Figure 5.26: Case 2: Profile of WRF-Fitch modelled wind speed difference with and without wind farms along wake length points of WF1 (a) and WF2 (b).

It can be seen, that the wind speed deficit is high in the region of or just downstream of the turbine rotors, with an increased wind speed below the rotor blades area. However, due to very unstable conditions which involves a high amount of convective flow, these wind speed differences do not propagate much downstream. The wind speed deficits are higher in this WRF-Fitch simulation as compared to the WRF-Fitch simulation under unstable conditions as well.

Similarly, Figure 5.27 presents for Case 2 the vertical profile of TKE difference with and without wind farms using the Fitch scheme, along the points identified in the wake region for WF1 (a) and WF2 (b).

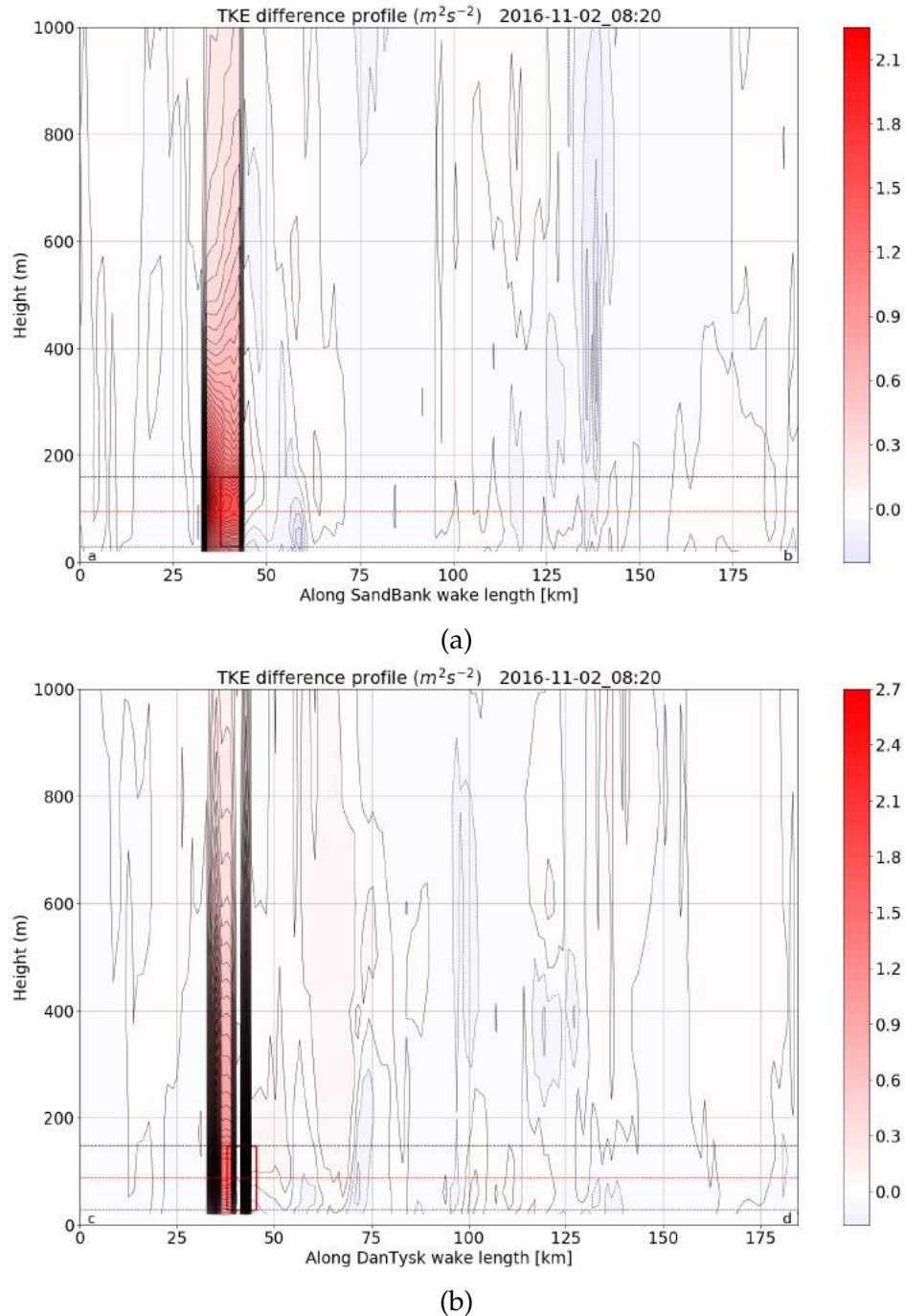


Figure 5.27: Case 2: Profile of WRF-Fitch modelled TKE difference with and without wind farms along wake length points of WF1 (a) and WF2 (b).

It can be seen, in this case too there is a large increase in the TKE restricted to around the wind farm rotor area for both wind farms, with a decreasing magnitude in the vertical. Here too, the magnitude of increase in TKE in and around the wind farm rotor region masks the minor TKE downstream. Due to convective unstable conditions however, the increased TKE extends with a decreasing magnitude to 1 km vertically above the wind farm. This is not observed under stable conditions, wherein the increased TKE extension in the vertical direction is limited and suppressed.

Case 3

Presented in Figures 5.28 and 5.29, are the horizontal wind speeds at 90 m when the wind farms are parametrised, and horizontal wind speed difference at 90 m with and without the wind farms using the Fitch scheme for Case 3 (2017-05-11 17:20) respectively.

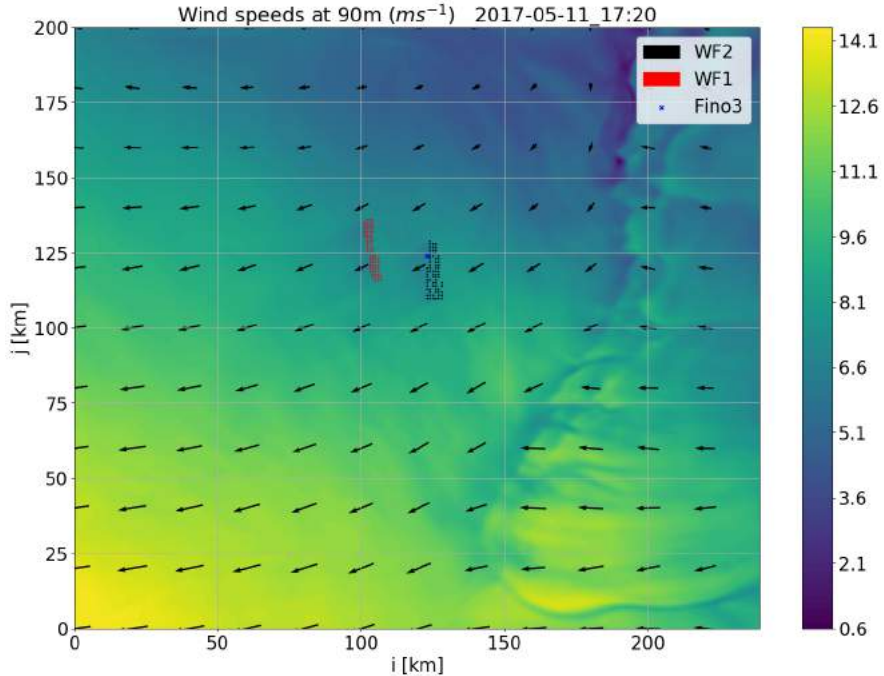


Figure 5.28: Case 3 (2017-11-05 17:20) : WRF-Fitch modelled wind speeds at 90 m with wind farms.

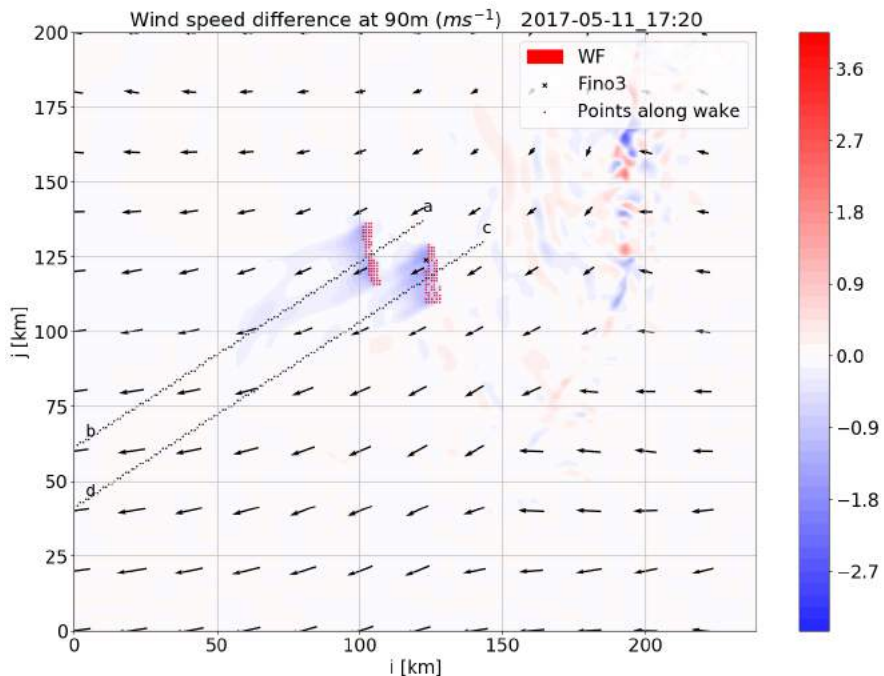


Figure 5.29: Case 3: WRF-Fitch modelled wind speed difference at 90 m - with and without wind farms.

The wind speed field and wake field in Figures 5.28 and 5.29 for Case 3 with the WRF-Fitch scheme respectively, show almost no differences when compared to the simulations from WRF-Fitch, with differences only in the wind speed values in the wind speed field and wake field.

Figure 5.30 presents for Case 3 the vertical profile of wind speed with and without wind farms using the Fitch scheme, along the points identified in the wake region for WF1 (a) and WF2 (b).

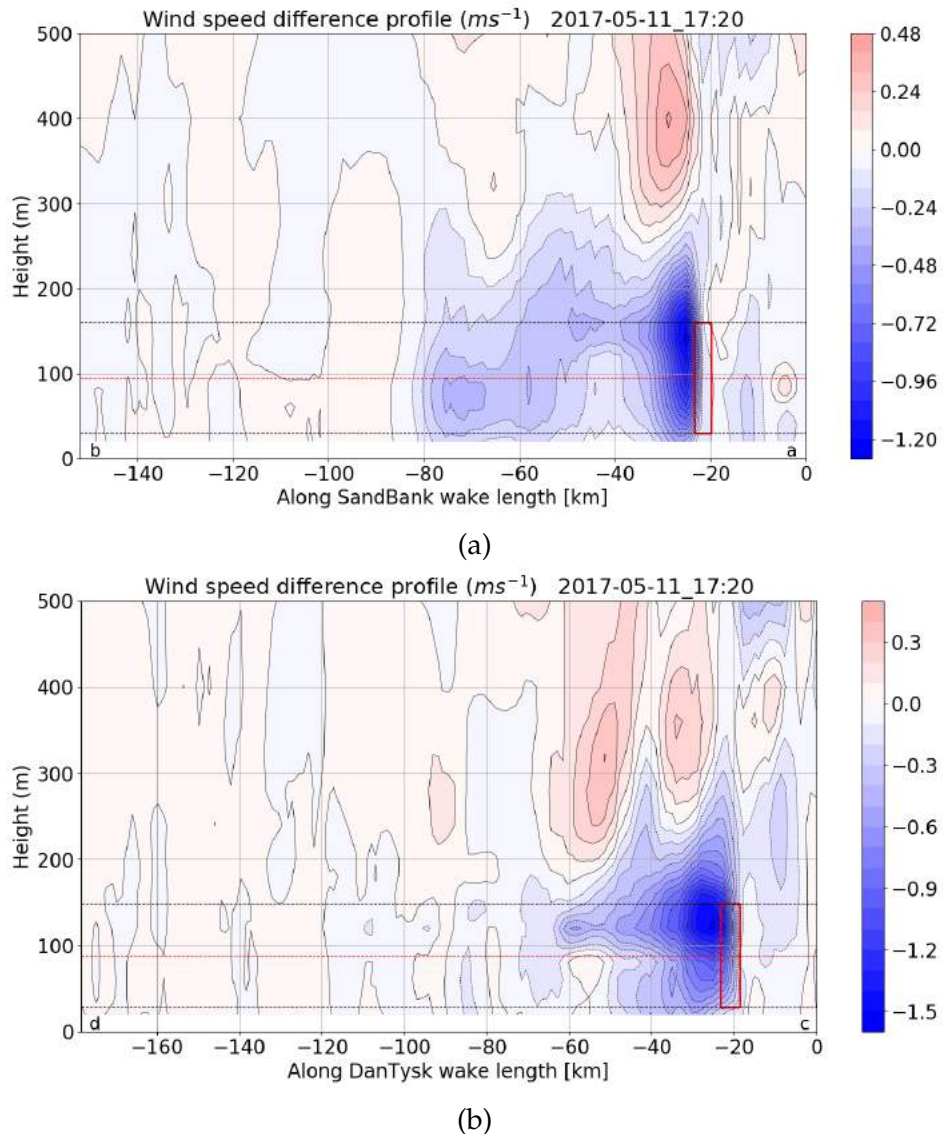


Figure 5.30: Case 3: Profile of WRF-Fitch modelled wind speed difference with and without wind farms along wake length points of WF1 (a) and WF2 (b).

It can be seen again, that the wind speed deficit patterns downstream are relatively similar to those observed in the WRF-Fitch simulations. In this case however, these is not a clear increase in wind speed below the rotor blades area as compared to Case 1 and Case 2 from WRF-Fitch simulations. The WRF-Fitch scheme results in the maximum wind speed deficit being larger in magnitude and closer to the upper

portion of the wind farm rotor area, which is not the case is the WRF-Fitch simulation and also causes differences in the flow downstream along the hub height.

Similarly, Figure 5.31 presents for Case 3 the vertical profile of TKE difference with and without wind farms using the Fitch scheme, along the points identified in the wake region for WF1 (a) and WF2 (b).

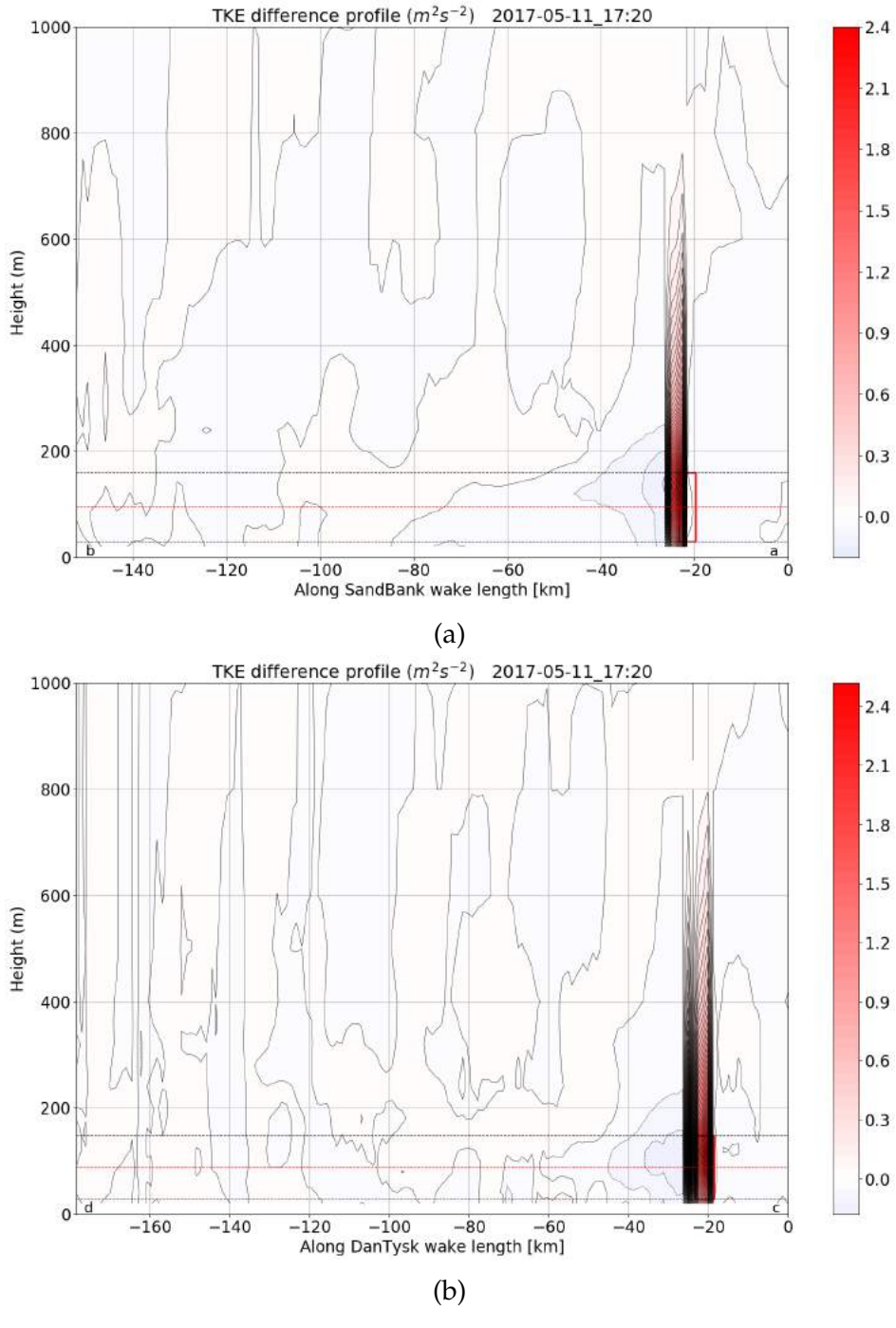


Figure 5.31: Case 3: Profile of WRF-Fitch modelled TKE difference with and without wind farms along wake length points of WF1 (a) and WF2 (b).

It can be seen, in this case too there is a large increase in the TKE restricted to around

the wind farm rotor area for both wind farms, with a decreasing magnitude in the vertical. Here too, the magnitude of increase in TKE in and around the wind farm rotor region masks the minor TKE downstream.

5.2.3 Summary

The wind fields simulated in case 1 (stable) and case 2 (unstable) are consistent with what is expected of the wake behaviour i.e wakes are expected to propagate greater distances or have a longer fetch under near-neutral stable and stable conditions, and have a shorter fetch in unstable conditions.

Gravity waves are simulated using both parametrisation schemes. However, for Case 5 with the corresponding satellite SAR image 2.4 which shows gravity waves across the flow domain, is not captured by the EWP nor Fitch scheme. However, the EWP scheme presents stronger gravity waves than the Fitch scheme in the wake of the wind farm.

There is a significant difference in the way TKE is modelled in the two schemes. In the EWP scheme, there is an increase in the TKE above the hub height of the wind farm, and a decreased TKE below hub height - both are gradual and propagate downstream. In the Fitch scheme, there is a sharp increase in the TKE in the wind farm rotor blade area and above the same, but the decreased TKE downstream of the wind farm is of negligible magnitude when compared to the increase at the wind farm locations.

5.3 Effect of Stability on Wakes

To quantify the effect of stability on wakes, the wake lengths for all the time stamps in the five simulations are calculated. As described in Chapter 5.2, as the number of time stamps for which the wake lengths have been calculated are 5 simulations of 24 hours each with time resolution of 10 minutes, totalling to 720 time stamps. Therefore, the process of identifying the line of points along wake based on upstream wind direction and corresponding wake analysis points, has been programmed in Python.

The wake lengths are determined by obtaining the wind speed difference values starting from the wake analysis point of each wind farm and going downstream. These wind speed differences are obtained for a height of 90 m for simplicity, with the assumption that the values do not deviate from the hub heights of 88 m (WF2) and 94.75 m (WF1). Wake lengths are determined by finding the downstream point at which the wind speed difference becomes smaller than a threshold percentage of the wind speed difference at the upstream wake analysis point. All the results presented in this chapter are for a threshold percentage set at 10%.

As an example, if the wind speed difference at a wake analysis point is -1 ms^{-1} , the first downstream point along the identified wake line found to have a wind speed difference greater than $-0.1 \text{ ms}^{-1} (> -0.1\text{ms}^{-1})$. The wake length is determined by identifying the downstream point (grid cell) where the the wind speed difference (with and without wind farms) is smaller than 10% of the wind speed difference at the wake analysis point, and then calculating the distance between these two points/grid cells. Wake lengths are obtained from the straight line of points identified based on an upstream wind direction, therefore they do not consider the turning or curvature of wakes. Due to this limitation, the total true length of the wakes are not considered at instances when the wakes are curved.

The atmospheric stability parameter L (Obukhov length) is calculated by calculating the Bulk Richardson number Ri_B using Equation 2.1, and then by using Equations 2.2 and 2.3. This Bulk Richardson number is calculated using the wind speed and temperature at 20 m height, and wind speed (assumed to be zero) and temperature at sea surface, all at the undisturbed flow analysis point (UAP) for each time instant. The atmospheric stability class is then identified using the classification method as presented in Table 2.2. Though wakes are affected by stability, the stability classification is based on a single upstream undisturbed flow point without considering the spatial distribution of Ri_B or L . *This approach has been chosen to understand the effect of free stream stability on wakes, and not the possibly modified stability due to the presence of wind farms.* However, as an example, Larsén et al. showed with the use of satellite SAR wind fields, that the wind speed at 10 m can vary by nearly 5 ms^{-1} in a range of up to 3 km in the presence of open cells - which were identified in the modelled wind field of Case 2 in Chapter 5.1. This introduces uncertainties in the stability classification. To get an idea of the possible spatial distribution of stability, the spatial distribution of the temperature differences between 20 m height and sea surface for the five snapshots are presented in Appendix B.

Tables 5.3 and 5.4 present the calculated wake lengths (km) of WF1 and WF2 for

a threshold value of 10%, and atmospheric stability classification for the respective UAP's, for the five snapshot time-steps from the five simulations of WRF-EWP scheme and WRF-Fitch scheme respectively, with both wind farms present in the innermost domain (D3).

Case	L (m)	Stratification	WF1 Wake Length	WF2 Wake Length
Case 1	108.99	Stable	41.23 km	103.86 km
Case 2	-180.18	Unstable	38.59 km	37.74 km
Case 3	-1176.47	Neutral	53.85 km	50.25 km
Case 4	476.19	Near Neutral Stable	77.37 km	83.68 km
Case 5	588.24	Neutral	103.25 km	106.04 km

Table 5.3: WRF-EWP modelled upstream stability values, and total wake length for WF2 and WF1 using a wake-length threshold of 10%.

Case	L (m)	Stratification	WF1 Wake Length	WF2 Wake Length
Case 1	109.59	Stable	49.04 km	99.81 km
Case 2	-180.18	Unstable	37.74 km	38.59 km
Case 3	-1176.47	Neutral	13.89 km	24.70 km
Case 4	476.19	Near Neutral Stable	92.89 km	88.77 km
Case 5	588.26	Neutral	117.18 km	108.27 km

Table 5.4: WRF-Fitch modelled upstream stability values, and total wake length for WF2 and WF1 using a wake-length threshold of 10%.

As it can be seen, the Obukhov length and the corresponding atmospheric stability classification using the two schemes give very similar results. The calculated wake lengths are in good agreement with what is visible in the profile plots of wind speed difference.

For Case 1, 4, and 5, the simulation based calculated wake lengths for the stratification condition from both schemes are in good agreement with the expected behaviour of wakes under the respective stability conditions, as longer wakes are expected in near-neutral stable and stable conditions than in unstable conditions.

Though the wake lengths for Case 2 do not differ with the schemes, the rather large values of wake length are a result of unexpected fluctuations in the wind field as seen in Figures 5.13 and 5.25. However, there is a large difference in the wake lengths between the two schemes in the neutral condition for Case 3. This is a result of the modelled flow fields varying in flow pattern and magnitude of difference in the wind speeds caused by the wind farms between the two schemes. The basis of calculating the wake lengths being at a single height above ground and the threshold percentage values used, also have an impact on the wake length calculations.

Though a manual approach of identifying the wakes and wake lengths for the five cases could possibly result in better results, this algorithm based approach yields satisfactory results over a larger sample, and is applied to all the time steps of the five simulations.

The stability distribution over the 5 simulations consisting of 720 time steps for the EWP and Fitch scheme is presented in Table 5.5. The stability distributions are almost the same between the two schemes. More than 60% of the 720 time steps belong to the unstable or neutral category, with only around 10% belonging to the stable category.

Scheme	Parameter	Unstable	Neutral	Near Neutral	Stable
EWP	Frequency (counts)	246	219	182	73
	Frequency (%)	34.17	30.41	25.28	10.14
Fitch	Frequency (counts)	246	219	181	74
	Frequency (%)	34.17	30.41	25.14	10.28

Table 5.5: Stability distribution (Frequency %) over simulations 1, 2, 3, 4, and 5 combined from the EWP and Fitch scheme respectively.

Figure 5.32 presents the time-variation of the stability conditions for the EWP and Fitch scheme over 24 hour periods from the simulations 1, 2, 3, 4, and 5. It can be seen that the variation of stability conditions with time is also almost the same between the two schemes.

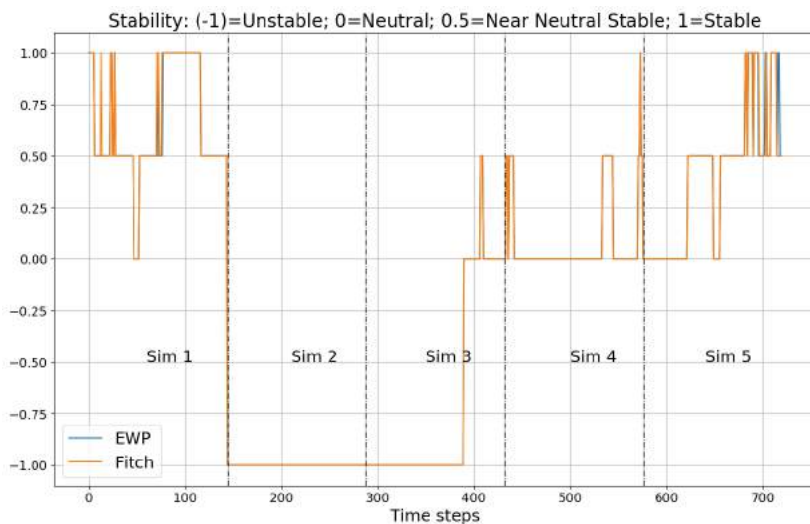


Figure 5.32: Variation of stability conditions with time for the EWP and Fitch scheme from the five simulations.

The presence of open cells indicating unstable atmospheric conditions in Case 2 (2016-11-02 08:20) as shown in Figures 5.12 and 5.24. This is further supported with Figure 5.32, wherein the entire duration of simulation 2 shows the atmosphere to be unstable.

Figure 5.33 presents the wind rose for the total 720 instances for the EWP scheme (a) and Fitch scheme (b) from the five simulations. It can be seen that the wind roses are almost the same for both schemes. The wind direction distributions are also similar to the wind roses obtained from Fino3 MET mast measurements as shown in Figures 4.2, with dominant westerly flows.

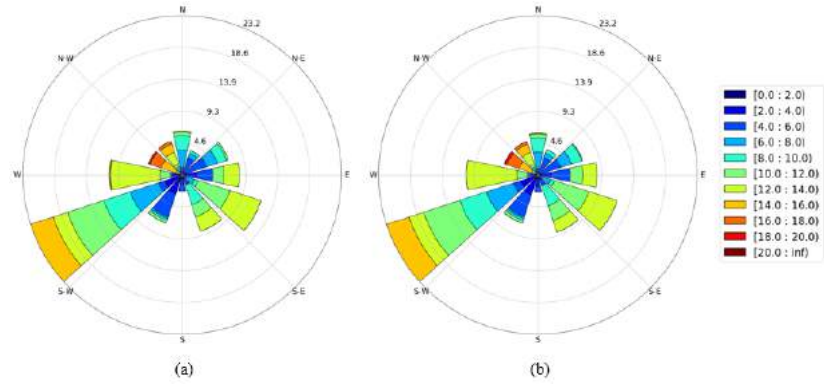


Figure 5.33: Wind rose of the total 720 instances distributed based on the wind direction for the EWP scheme (a) and Fitch scheme (b) from the five simulations.

As mentioned, due to the lower wind speed bulk under stable conditions, the overall mean wake length for stable conditions is probably reduced. This is further analysed in Figure 5.34, which shows the mean wake length of the two wind farms as a function of wind speed intervals.

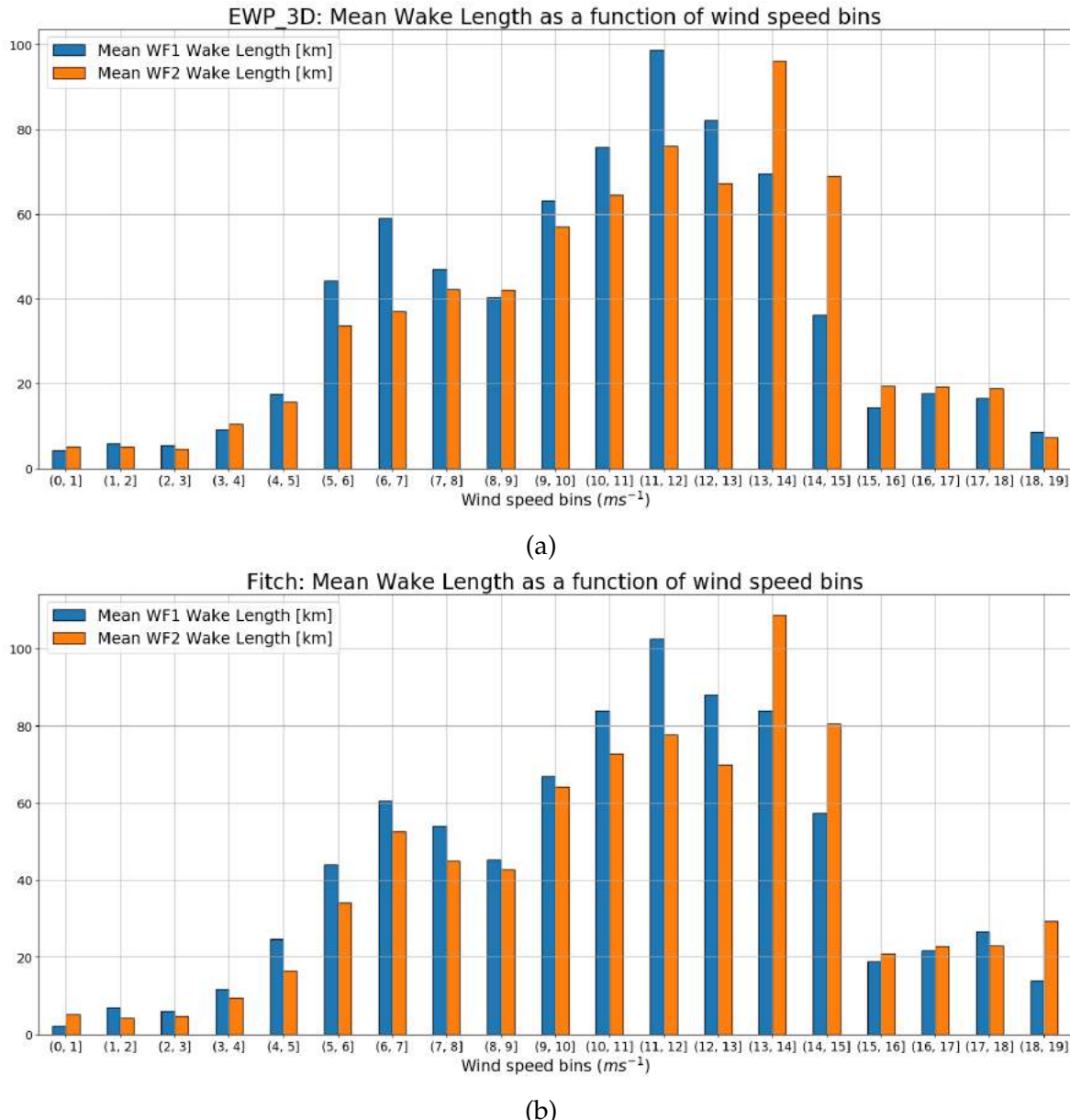


Figure 5.34: Mean wake lengths [km] of WF1 and WF2 as a function of wind speed intervals for EWP scheme (a) and Fitch scheme (b).

As it can be seen, the mean wake lengths are greatest for the wind speed range 9-14 ms^{-1} .

Figure 5.35 presents the mean wake lengths of the 720 instances calculated for each of the wind farms as a function of undisturbed wind direction - both obtained using the EWP scheme (a) and Fitch scheme (b). The wind direction is the undisturbed upstream wind direction from the WRF simulations.

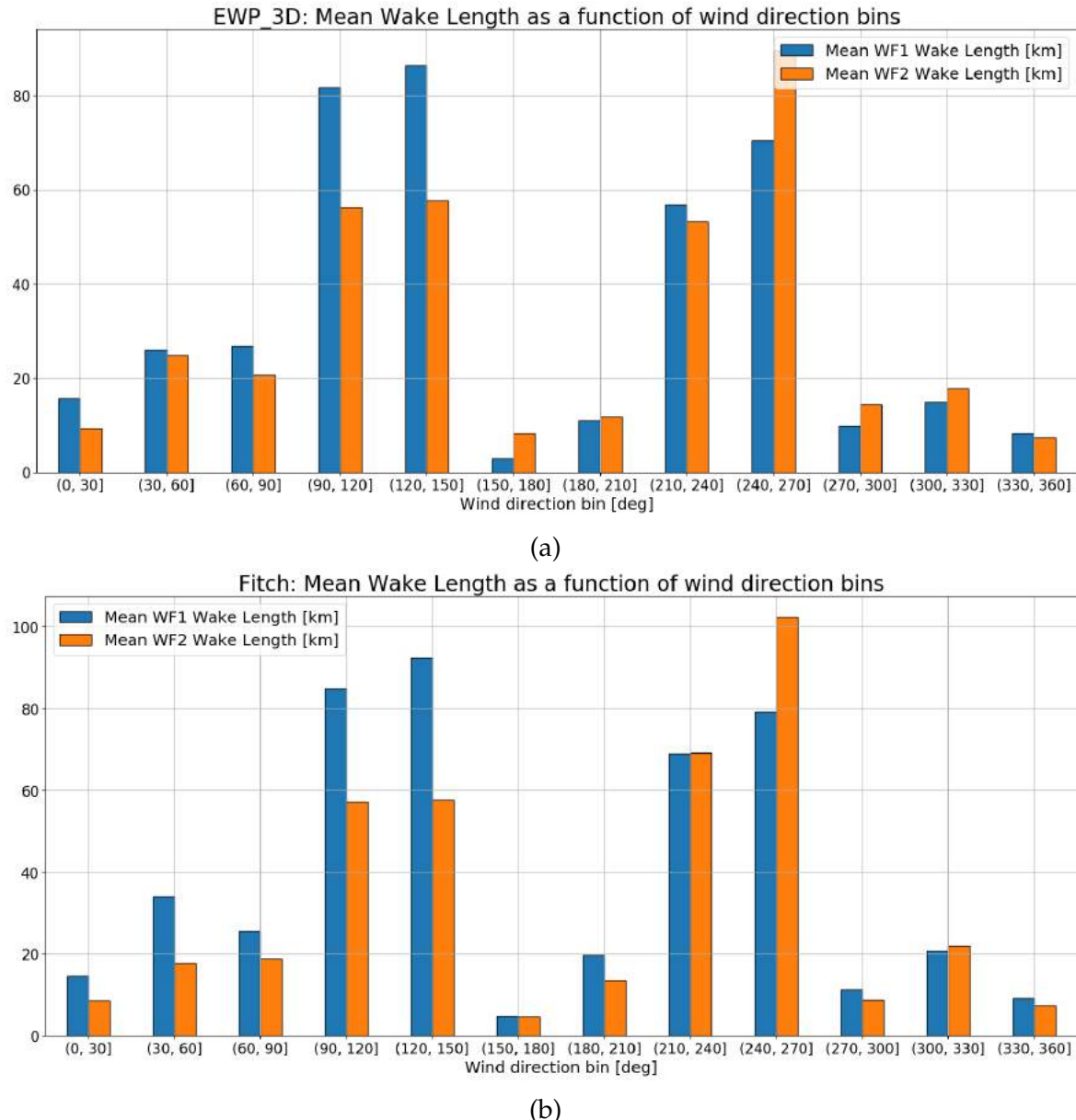


Figure 5.35: Mean wake lengths [km] of WF1 and WF2 as a function of wind direction bins for EWP scheme (a) and Fitch scheme (b).

As it can be seen, the longest mean wake lengths are encountered in the directions where superposition of the wind farm flows occur. It is interesting to note that in the 90° - 150° wind direction bins, the mean wake length of WF1 is greater than that of WF2, which is expected - as in this inflow sector WF1 is the upstream wind farm, and superposition of wakes would result in WF1 showing longer wakes. The opposite is seen in the 240° - 270° wind direction bin, as now WF2 is the upstream wind farm with respect to the inflow sector.

Figure 5.36 presents the stability rose - distribution (frequency) of the stability classifications calculated for the total 720 instances, distributed based on the wind direction for the EWP scheme (a) and Fitch scheme (b) from the five simulations. The atmospheric stratification class is based on the undisturbed upstream parameters (from UAP's) from the WRF simulations.

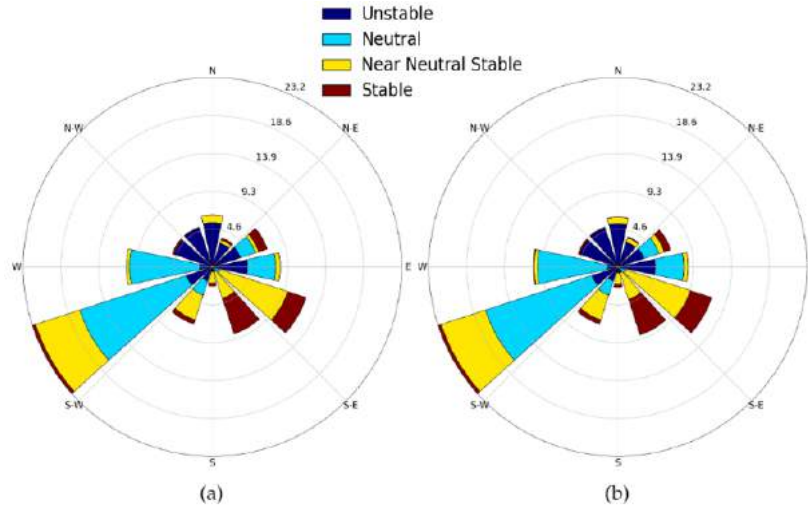


Figure 5.36: Stability rose of the total 720 instances distributed based on the wind direction for the EWP scheme (a) and Fitch scheme (b) from the five simulations.

Here too, it can be seen that the differences between the EWP scheme based and Fitch scheme based stability roses are very small. Majority of the flows are from the S-W and S-E directions, with neutral and near neutral stable conditions dominating the flow from the S-W and W directions. Most of the stable and near neutral stable flows are from the S-E direction.

Figure 5.37 presents the wind speed distributions of the total 720 instances distributed based on the stability conditions for the EWP scheme (a) and Fitch scheme (b).

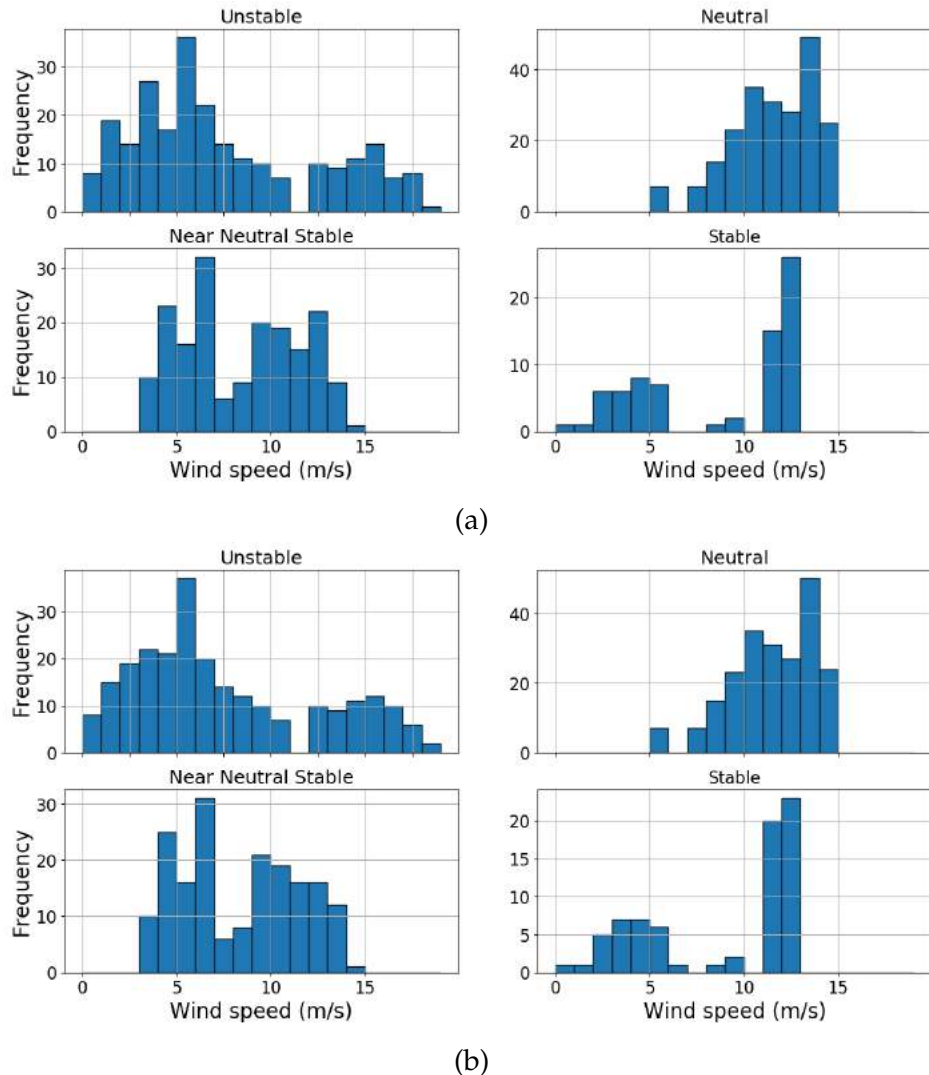


Figure 5.37: Wind speed distributions of the total 720 instances distributed based on the stability conditions for the EWP scheme (a) and Fitch scheme (b).

It can be seen that under unstable conditions, the wind speeds are fairly spread over a wider range. In stable conditions however, the wind speeds are concentrated in two regions - the lower range below 6 ms^{-1} , and about 60% of the stable wind speeds are in a range of $11\text{-}13 \text{ ms}^{-1}$. This could lead to shorter wakes and lower power losses under stable conditions due to the bulk of lower wind speeds, and could affect the mean wake length of the category. Under neutral and near neutral conditions however, there is a much larger share of higher wind speeds with the bulk around 7 ms^{-1} for the near neutral conditions, and around $10\text{-}15 \text{ ms}^{-1}$ under neutral conditions.

Figure 5.38 presents the mean wake lengths (km) of the 720 instances calculated for each of the wind farms as a function of atmospheric stratification using the EWP scheme (a) and Fitch scheme (b).

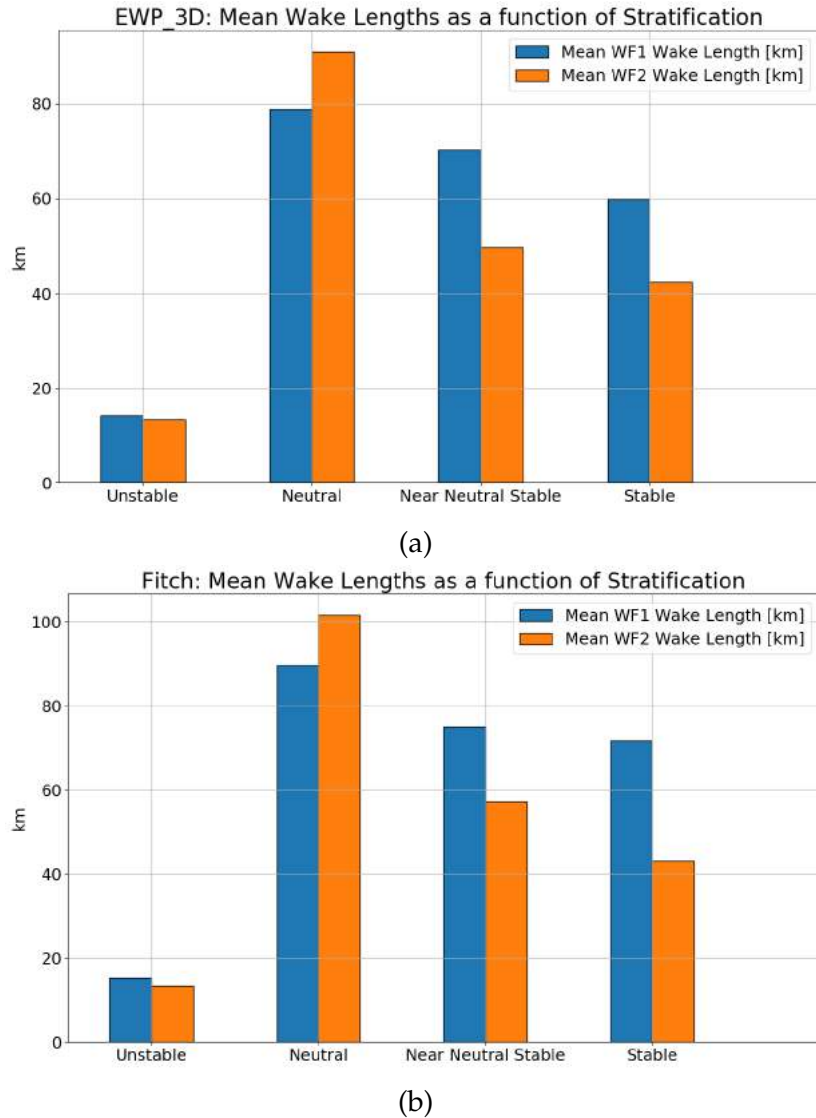


Figure 5.38: Mean wake lengths [km] of WF1 and WF2 as a function of atmospheric stability condition for EWP (a) and Fitch (b) from the five simulations.

Between the schemes, the mean wake lengths are greater in the Fitch scheme for neutral and near-neutral stable for both wind farms, and for WF1 only under stable condition. This could be a result of the magnitude of difference in wind speeds as modelled in the Fitch scheme as presented in Chapter 5.1.2, wherein the Fitch scheme shows a larger magnitude of wind speed deficit due to the presence of the wind farms than the EWP scheme. The mean wake lengths for the other conditions and for WF2 under stable conditions are very similar in both schemes. As expected, the mean wake lengths are greater for the near-neutral stable and stable conditions than unstable conditions. It can be seen that the mean wake lengths are greatest for neutral stratification, followed by near neutral stable and stable resulting in almost identical values, and unstable conditions yielding the shortest wakes.

As highlighted from Figure 5.37, due to the share of lower wind speeds under stable conditions, the mean wake length is lowered due to the potential absence of wakes at wind speeds around and below the power curve cut-in wind speed. Also as seen

in Figure 5.36, neutral, near-neutral stable and some stable conditions dominate the sectors where flow interaction or superposition of flow may occur between the wind farms i.e. W, S-W, E, and S-E sectors where cross flow between the wind farms occurs. The combination of higher wind speeds and higher occurrence in the cross-flow direction under neutral and near neutral stable conditions could explain the longer wakes than in stable conditions.

Therefore, it suggests that the WRF wind farm parametrisation schemes simulate the wake fields for different stability conditions as expected in most cases, and the automatic wake length detection algorithm captures the wake lengths satisfactorily with the functionality to change the wind speed deficit threshold, but also with the limitations in capturing wake turning. It also highlights the dependence on the estimation of atmospheric stability conditions, the wind speed, wind direction, and stability distribution, and the wake length determination method (which does not capture wake turning) used in this project. One way of reducing these uncertainties is to run simulations for a long duration (more than a few months) to capture all possible combinations of varying stability, wind speeds, and wind directions, and to then obtain a matrix of the wake length as a function of all three. However, with a sample of five-one day simulations that's not possible. But these simulations aid in understanding how exactly wakes behave in the two schemes under different stability and wind conditions. Also, there are inherent uncertainties in the WRF modelling system, the two wind farm parametrisation schemes, along with the initial and boundary conditions used, that introduce uncertainties and errors to these results.

5.4 Effect of Stability on Power Production

As explained in Chapter 3.3, the power losses are calculated by taking the difference of the power production of the two wind farms and the sum of the productions of the individual wind farms if the other had not been there - using the wind farm parametrisation schemes.

Figure 5.39 presents the total power losses (MW) of the 720 instances calculated for each of the wind farms as a function of atmospheric stratification using the EWP scheme (a) and Fitch scheme (b). This atmospheric stratification class is calculated using the UAP parameters from the WRF-EWP and WRF-Fitch simulations, using the same method as presented in Chapter 5.3.

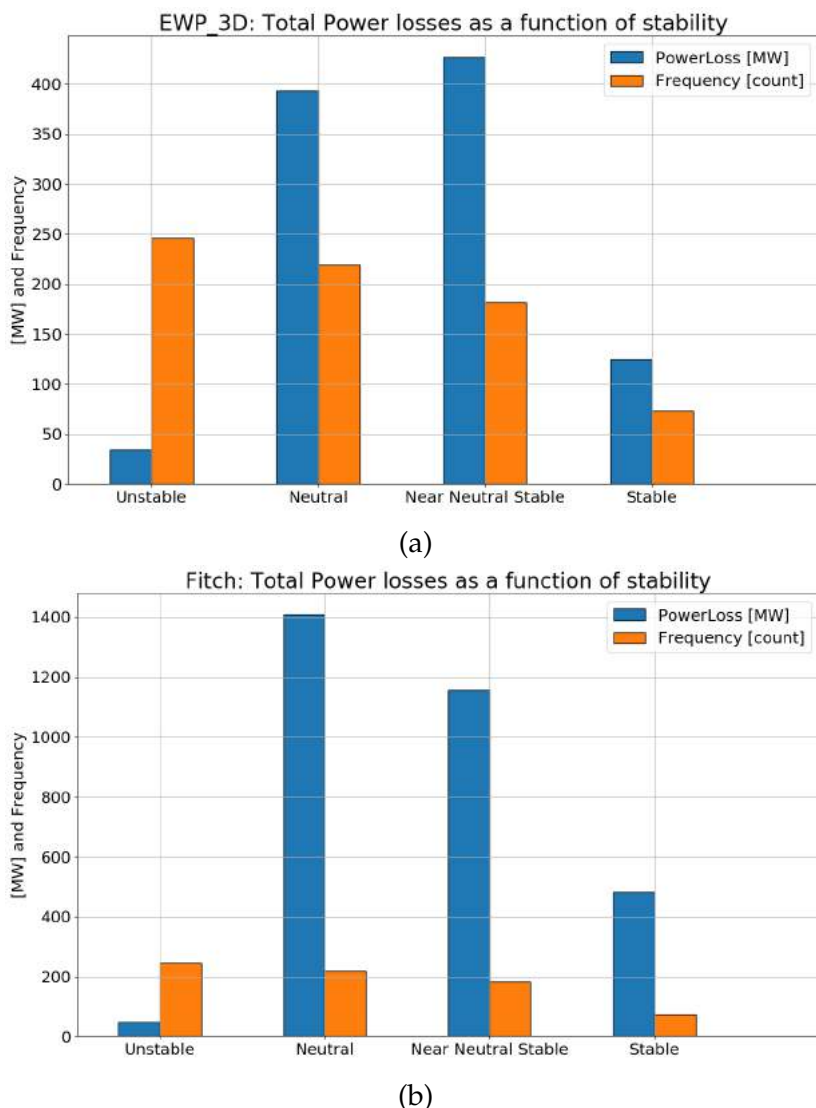


Figure 5.39: Total power losses (MW) as a function of atmospheric stability condition, and corresponding frequency of occurrences for EWP (a) and Fitch (b).

It can be seen that the total power losses are greatest for near neutral stable conditions, followed by neutral and stable conditions using the EWP scheme. For the

Fitch scheme however, the greatest total power losses are observed under neutral and near-neutral stable conditions, followed by stable conditions. In both schemes, though the frequency or occurrences of unstable samples is the largest, the power losses are the lowest. Stable conditions have the lowest frequency of occurrence (around 10%) throughout these 720 modelled time stamps. In this case too, the total power losses (MW) are lower in stable conditions as compared to neutral and near neutral stable conditions due to the distribution of wind speeds and stabilities in different directions as presented in Figures 5.33, 5.36, and distribution of wind speeds in each stability condition as shown in Figure 5.37. The lower total power losses under stable conditions is due to the portion of low wind speeds under stable conditions, along with most of the stable conditions being concentrated in the S-E and N-E sectors. Lower wind speeds translate to shorter wakes and lower power production, which would result in lower power losses as well. Similar to the mean wake lengths, the power losses are the largest in neutral and near neutral stable conditions, due to the presence of greater number of higher wind speeds, and a large amount of neutral condition flows being present in the cross-flow directions.

The total power losses among all stability conditions using the Fitch scheme are much greater than when the EWP scheme is used, with total power losses of 3093.96 MW using the Fitch scheme and 978.94 MW using the EWP scheme. This is an indication of the differences obtained wind speed values using the two schemes, as the modelled power values are directly proportional to the modelled wind speeds. The longest mean wake lengths occur in neutral conditions according to Figure 5.38 for both schemes, but the power losses are higher in near-neutral stable conditions for the EWP scheme. This could perhaps be indication of the wind speed deficits being larger in near-neutral stable conditions as compared to neutral conditions in the EWP scheme. On the contrary, it also highlights that longer mean wake lengths do not translate to larger power losses, as the mean wake length is dependent on the range and distribution of wake lengths obtained for a stability class.

However, as expected, the total power losses are greater for the near-neutral stable and stable conditions even with lower frequency of occurrences than unstable conditions - which have the highest frequency of occurrences among the 720 time stamps. This behaviour of the parametrisation schemes is in agreement with literature.

Figure 5.40 presents the total power losses (MW) of the 720 instances calculated for each of the wind farms as a function of undisturbed wind direction - both obtained using the EWP scheme (a) and Fitch scheme (b). The wind direction is the undisturbed upstream wind direction from the WRF simulations.

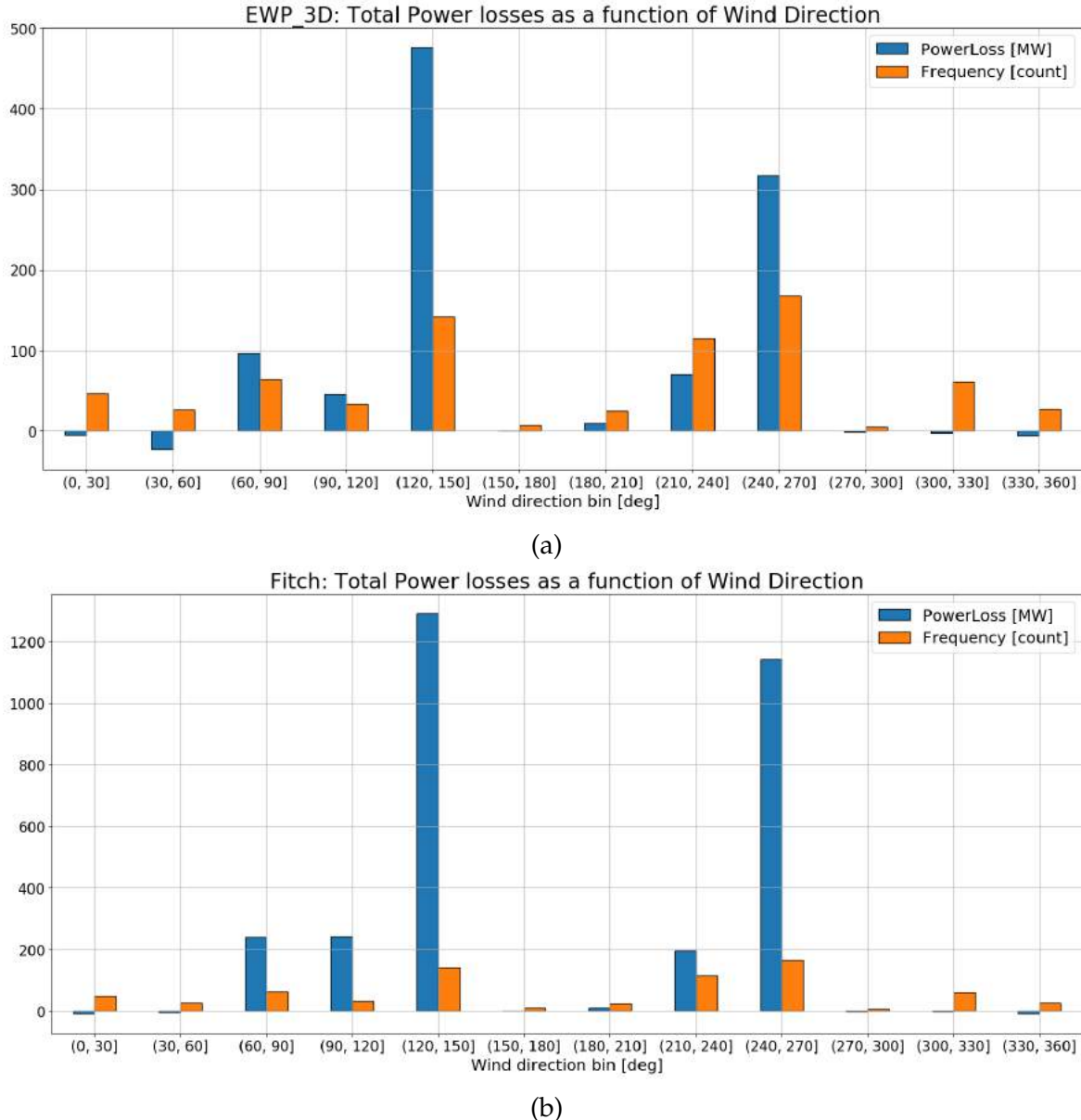


Figure 5.40: Total power losses (MW) as a function of wind direction bins, and corresponding frequency of occurrences for EWP (a) and Fitch (b).

It can be seen that the highest power losses occur in the East-West directions where cross-flow or flow interaction between the wind farms is possible.

To evaluate the WRF-modelled power against measurements, only the modelled power values from simulations 3, 4, and 5 are used as there are no valid power measurements available for the time-stamps corresponding to those in simulations 1 and 2. Figure 5.41 presents the comparison of total measured power (WF1+WF2) and WRF-modelled power using the EWP and Fitch schemes for the three simulations.

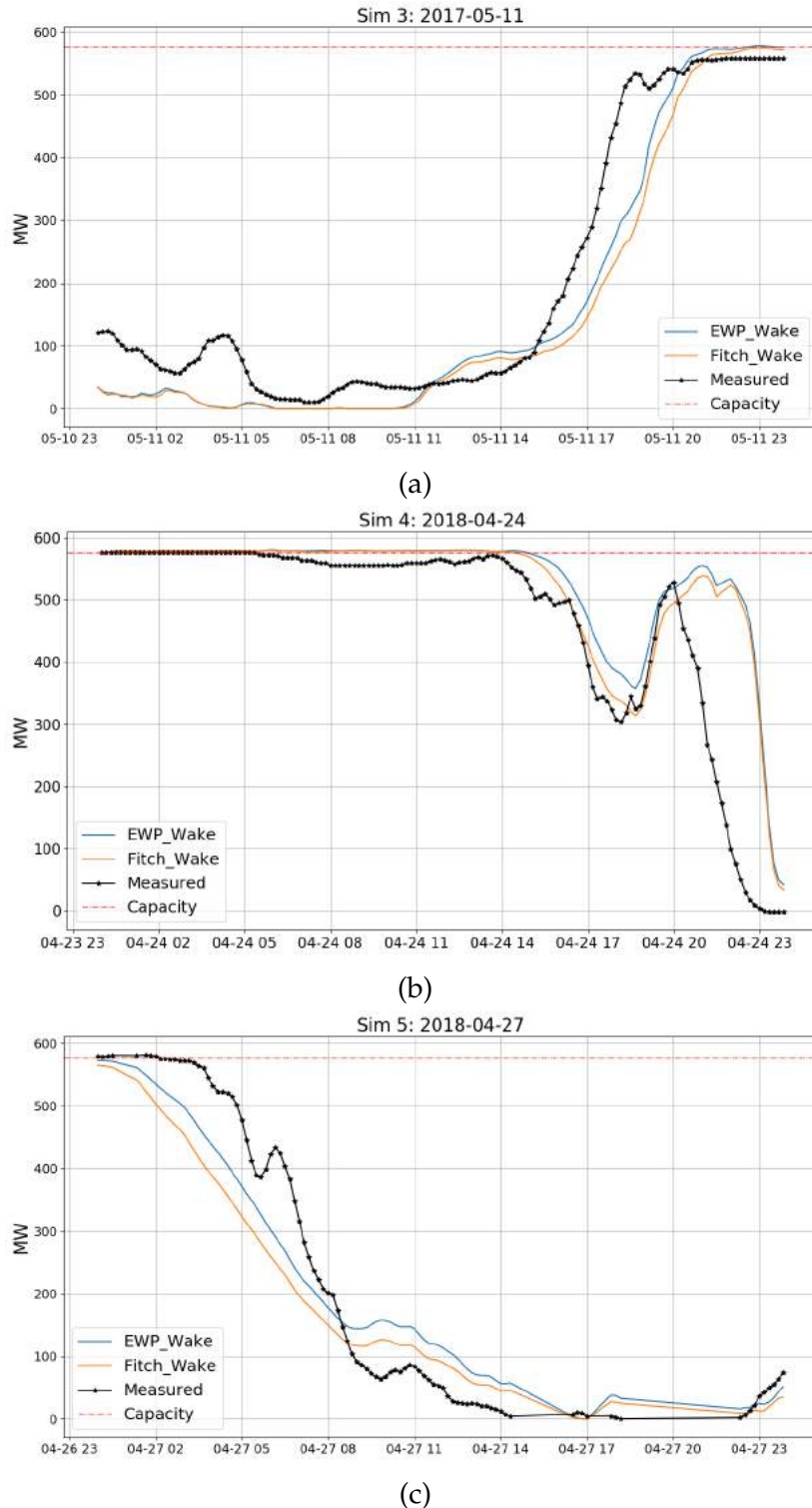


Figure 5.41: Comparison of measured and WRF-modelled power (MW) using EWP and Fitch schemes for simulation 3 (a), simulation 4 (b), and simulation 5 (c).

It can be seen that the WRF-modelled power using both schemes is in good agreement with the measurements for most time-steps of all 3 simulations. However, towards the end of simulation 4 (b) the absolute bias is very large, at approximately 450 MW around hour=22 - both in the EWP and Fitch scheme, which is much larger

than the bias values observed in simulation 3 (a) and simulation 5 (b). It can also be seen that the Fitch scheme models a lower power than the EWP scheme. This is also because of the larger magnitude of reduction in the wind speed values when using the Fitch scheme as seen in Chapter 5.2. Therefore, in the case of a positive bias (measurements are higher than modelled power), the EWP scheme would perform better than the Fitch scheme for these 3 simulations. Though both, the EWP and Fitch scheme would perform better than with no wind farm parametrisation scheme. The opposite is true when there is a negative bias, wherein the Fitch scheme performs better than the EWP scheme,

Tables 5.6, 5.7 and 5.8 present the Average Bias, Mean Absolute Error (MAE) and Root Mean Squared Error (RMSE) of the modelled 10-minute power (MW) values compared to measured power over simulations 3, 4, and 5 using the WRF-EWP and WRF-Fitch schemes.

	EWP	Fitch
Simulation 3	37.61	47.84
Simulation 4	-58.99	-48.55
Simulation 5	11.02	37.94

Table 5.6: Average bias of 10-min measured and modelled power (MW) over simulations 3, 4, and 5 using the WRF-EWP and WRF-Fitch schemes.

	EWP	Fitch
Simulation 3	49.31	54.87
Simulation 4	59.19	51.82
Simulation 5	57.05	66.36
Average	55.18	57.68

Table 5.7: MAE of 10-min measured and modelled power (MW) over simulations 3, 4, and 5 using the WRF-EWP and WRF-Fitch schemes.

	EWP	Fitch
Simulation 3	67.57	79.24
Simulation 4	121.75	115.10
Simulation 5	67.05	84.24
Average	85.46	92.86

Table 5.8: RMSE of 10-min measured and modelled power (MW) over simulations 3, 4, and 5 using the WRF-EWP and WRF-Fitch schemes.

It can be seen that for time period covering simulations 3, 4, and 5, the average MAE and RMSE is lower for the EWP scheme than the Fitch scheme. The average NMAE (MAE normalised by total capacity) for the EWP scheme is 9.58%, whereas for the Fitch scheme it is 10.01% - almost 0.5% higher when using the Fitch scheme.

Figure 5.42 shows an overall view of the influence of stability, wind speed and wind direction on the power losses due to wake interaction as seen in WRF. The stability conditions, wind speed, and wind direction parameters are obtained from the corresponding Undisturbed flow Analysis Points (UAP's) based on an initial wind direction from the WRF-EWP scheme, as the stability conditions from the WRF-EWP scheme and WRF-Fitch scheme are almost the same as seen in Figure 5.32 in Chapter 5.3.

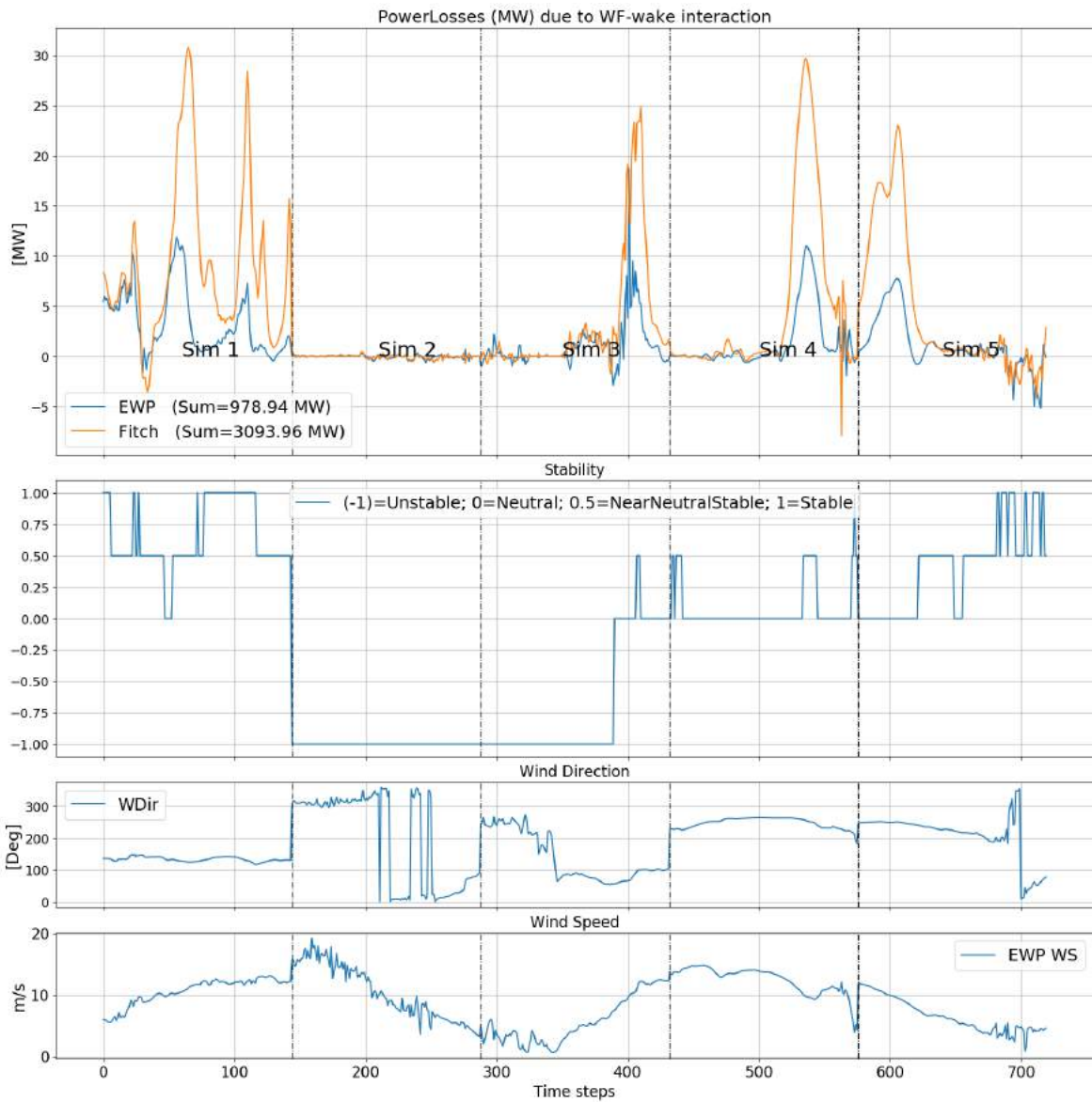


Figure 5.42: 10-min Power Losses [MW] due to the wake interaction as seen in WRF using the Fitch and EWP scheme as a function of corresponding atmospheric stability, wind direction, and wind speed for the five simulations.

It can be seen that simulation 1 and 5 show high power losses and have a lot of near neutral stable and stable conditions, but due to low wind speeds and changed wind direction towards the second half of simulation 5, the power losses drop.

The relationship between stability and power losses becomes clear when analysing simulation 2, where the power losses are the lowest throughout and the atmosphere is unstable throughout as well, even if with high wind speeds. There is also a visible correlation between power losses and wind direction, with highest power losses occurring in the cross-flow directions between 80° and 135° , and between 260° and 320° . Also, under lower wind speeds, the power losses are also very low. Negative power losses suggests that the presence of both wind farms gives higher power instead of the sum of each of them having been there individually. Though the cause of this is not clear, the plot indicates that the larger negative values occur in stable conditions.

For the 9 day simulation, the WRF modelled power using the EWP and Fitch schemes is plotted against the measured capacity for the same duration and presented in Figure 5.43. It can be seen that for most parts of the power time series, the WRF-EWP and WRF-Fitch modelled power values are similar, but differ by a larger margin on 2018-04-19 and 2018-04-20. Though the two schemes model the phases of increasing and decreasing production in good agreement with the measurements, the values differ on visual inspection.

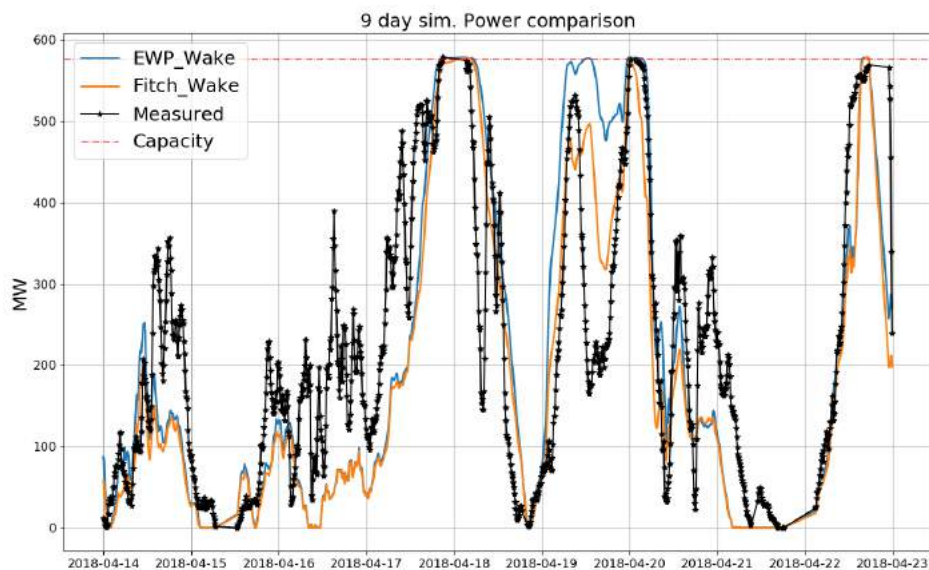


Figure 5.43: Comparison of 10-min measured and WRF-modelled power (MW) using EWP and Fitch schemes for the 9 day simulation as a function of corresponding atmospheric stability, wind direction, and wind speed for the five simulations.

Table 5.9 presents the Average Bias, Mean Absolute Error (MAE) and Root Mean Squared Error (RMSE) of the modelled 10-minute power (MW) values compared to measured power over simulations 3, 4, and 5 using the WRF-EWP and WRF-Fitch schemes.

Parametrisation Scheme	EWP	Fitch
Average bias	15.10	44.23
MAE	96.51	88.84
RMSE	129.15	115.22

Table 5.9: Average bias, MAE, and RMSE of 10-min measured and modelled power (MW) over the 9-day simulation using the WRF-EWP and WRF-Fitch schemes.

It can be seen that in this case, while the average bias suggests that the EWP scheme performs better than the Fitch scheme, the Fitch scheme models the power more accurately than the EWP scheme when using the MAE and RMSE. This is different from the error comparison observed for the combinations of simulations 3, 4 and 5, where the EWP scheme modelled the power more accurately than the Fitch scheme.

Figure 5.44 shows an overall view of the influence of stability, wind speed and wind direction on the bias between measured and modelled power using WRF-EWP and WRF-Fitch. The stability, windspeed, and wind direction parameters are obtained from the corresponding Undisturbed flow Analysis Points (UAP's) based on an initial wind direction.

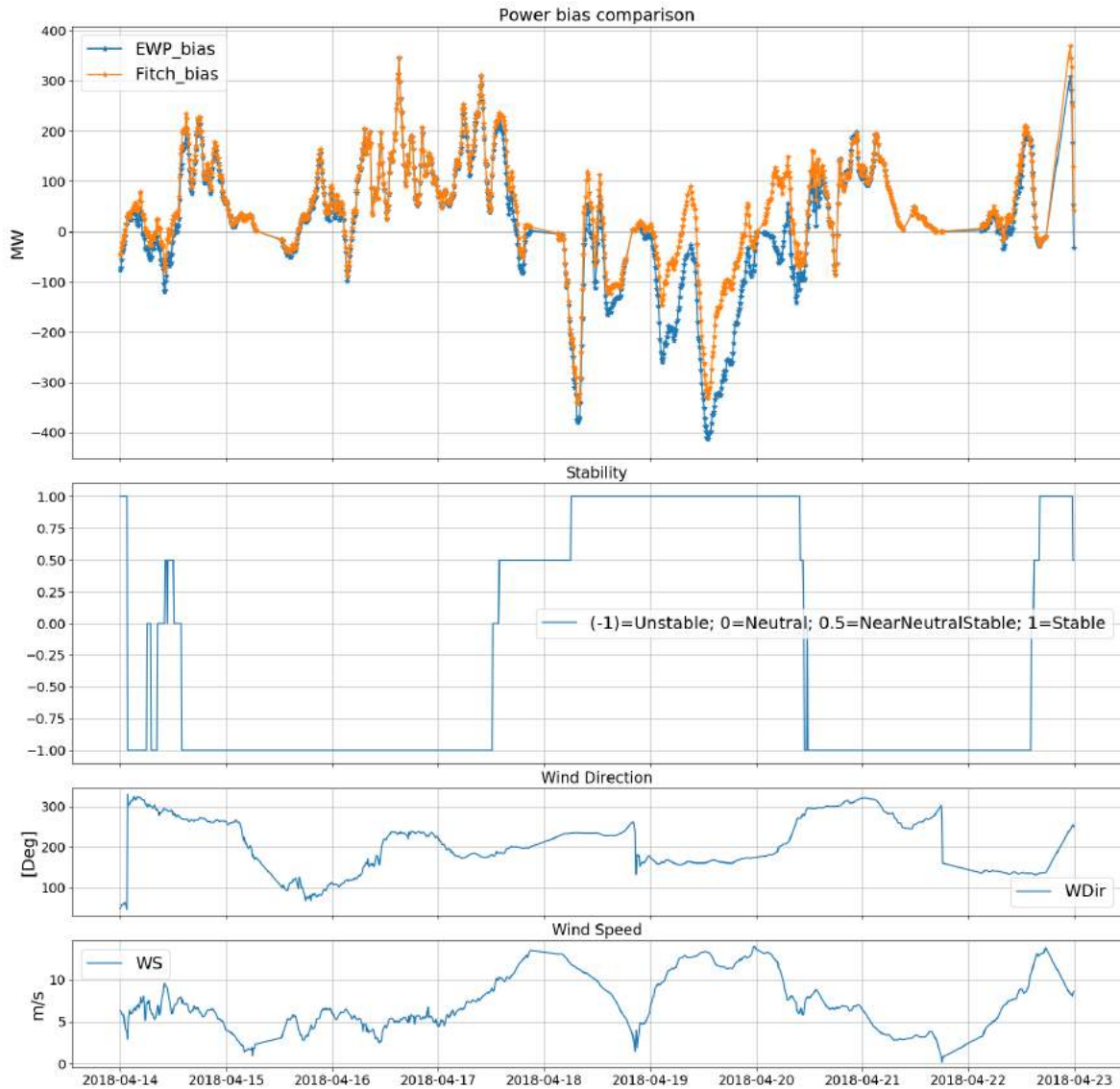


Figure 5.44: Bias between 10-min measured and WRF-modelled power (MW) using EWP and Fitch schemes for the 9 day simulation as a function of corresponding atmospheric stability, wind direction, and wind speed for the five simulations.

It can be seen that the WRF-EWP and WRF-Fitch modelled power values are very similar to each other for most of the time series over the 9 day simulation, but differ to a large extent between 2018-04-17 and 2018-04-21 (excluding 21st), during which there are extended periods of stable stratification. The significantly larger negative bias when using the EWP scheme indicates that the WRF-EWP modelled power is larger than the WRF-Fitch modelled power, and therefore so are the modelled wind speeds. Also in Figure 5.41, the WRF-EWP modelled power were either the same as or higher than the WRF-Fitch modelled power. This is the same pattern found in Chapter 5.2 where the wind speed deficits in the wake region of the wind farms were larger for the WRF-Fitch scheme, indicating a higher wind speed in the WRF-EWP modelled wake. However, under the extended period of stable conditions seen in the current figure, there is a corresponding larger negative bias when using the EWP-scheme, suggesting that in stable conditions, the WRF-EWP modelled power

is higher than the measured power for most instances. The WRF-Fitch modelled power bias though, fluctuates between the positive and negative bias, but for most of the time in the negative bias region. However, the WRF-Fitch modelled power bias is not as large as in the case of WRF-EWP, and this reflects in the error metrics as presented in Table 5.9.

Table 5.10 presents the Average bias of the modelled 10-minute power (MW) values compared to measured power over each day of the 9 day simulations using the WRF-EWP and WRF-Fitch schemes.

	Date	14th	15th	16th	17th	18th	19th	20th	21st	22nd
MAE	EWP	78.36	40.64	114.86	119.02	96.01	190.14	71.18	66.33	59.49
	Fitch	80.58	42.79	116.82	130.01	88.38	95.03	87.71	67.37	71.77
Avg Bias	EWP	47.69	26.26	106.84	108.08	-87.07	-190.14	27.69	66.33	50.49
	Fitch	69.42	30.83	110.07	125.10	-59.90	-80.67	70.59	67.36	66.43

Table 5.10: Average bias and MAE of 10-min measured and modelled power (MW) for each day over the 9-day simulation from 2018-04-13 to up to 2018-04-23 using the WRF-EWP and WRF-Fitch schemes.

It can be seen that the 18th and 19th are dominated by stable conditions (2018-04-18 and 2018-04-19), the corresponding average bias is negative when using both schemes. From the time-stamps present in the 9 days, both schemes appear to model power values higher than measurements under periods dominated by stable conditions, whereas the opposite seems to occur during periods dominated by unstable conditions wherein, both schemes model power values lower than the measurements. For periods dominated by unstable conditions, the EWP scheme models a more accurate power. For periods dominated by stable conditions however, the Fitch scheme models a more accurate power. It cannot be concluded that this is the general behaviour of the schemes, however, it can be said so about the behaviour of the two schemes from the cases available in the 9 day simulation.

Chapter 6

Discussion and Conclusions

This project presents an analysis of the effect of stability conditions on offshore wind farm wakes as seen in WRF using two wind farm parameterisation schemes - (i) The Explicit Wake Parametrisation (EWP) scheme, and (ii) Fitch scheme.

With limited measurements of the flow field affected by large offshore wind farms, studying the effects such large offshore wind farms have on neighbouring wind farms is needed to develop better performing wind farms that utilise the wind resources of a region optimally without affecting each other, and for reliable and accurate operational forecasting. An overview of the literature relevant to this project that deal with - offshore wind farm wakes; satellite SAR wind field images and their use in case studies of stability and wake lengths; the behaviour and use of wind farm parametrisation schemes in WRF; and the general effects of stability on wakes and power is provided in Chapter 1.

Case studies of stability and wake lengths from satellite SAR images are limited by the sample of images available, which may not be the case with modelling wind farms in WRF using the parametrisation schemes. The real case WRF modelled results are analysed in greater detail to answer two important research questions in this project:

1. What is the effect of atmospheric stability on offshore wind farm wakes using mesoscale models, with WRF wind farm parameterisation schemes - the EWP and Fitch scheme?
2. How do the two schemes differ in modelling the wind speeds or power in a real case setup?

Satellite SAR images have been used to identify cases with visible wakes from Sand-Bank (WF1) and DanTysk (WF2), and Fino3 MET mast data has been used to identify two cases of stable and unstable conditions. Answering the two important research questions involves the following WRF model setups - 24 hour periods that include the five identified cases are modelled with the two schemes separately using four different setups (8 setups for each identified case):

1. Both wind farms present in the innermost domain (D3) of the WRF model setup with the wind farm scheme on.
2. No wind farms present in D3.
3. Only WF1 present in D3 with the wind farm scheme on.
4. Only WF2 present in D3 with the wind farm scheme on.

Using the combinations of the above setups, the region of wind farm affected flow is obtained by (*Setup1 – Setup2*), and power losses caused by the interaction between the wind farms are obtained by (*Setup1 – (Setup3 + Setup4)*) (see Chapter 3.4).

The analysis shows that the modelled wind field patterns and flow characteristics are in good agreement with the SAR images, and indications of the appropriate stability conditions are present for cases where stability conditions are already known.

There are differences in the modelling of wind speeds below the rotor blade area - with the Fitch scheme presenting an increase below the rotor blade area, and the EWP scheme presenting a decrease throughout the rotor area and below. Also, the magnitude of the wind speed differences closer to hub height is larger in the Fitch scheme. However, the wake patterns are very similar in both schemes.

The TKE difference observed between the two schemes varies significantly, with relatively gradual changes in in the EWP scheme modelled flow field. A sudden and large increase in TKE is observed in the wind farm region in the Fitch scheme, which masks the negligible differences downstream. This sudden increase in TKE is a result of the TKE being generated by a source term in the Fitch scheme. In the EWP scheme, a decreased TKE is observed in the rotor blade area, and an increase above. Propagation of wind speed and TKE differences to longer distances downstream is observed for stable condition cases, but in the unstable case (Case 2), they extend up to large distances in the vertical due to convective conditions, but not in the horizontal.

A method of identifying the wake lengths and stability conditions based on the upstream wind direction and WAP's is developed (see Chapter 5.2). From all the 10-minute time steps from the five simulations- wake lengths, stability class, and power losses as in the parametrisation schemes are obtained.

An analysis of the effect of stability on wake lengths as seen in WRF using the two parametrisation schemes shows that the wake lengths are captured satisfactorily for each stability condition with a certain margin of error due to random values in the wake fields or due to wake turning. The mean wake lengths for the two wind farms are also found to be the greatest in the cross-flow direction, and between the wind speed range 9 ms^{-1} - 14 ms^{-1} . The longest mean wake lengths are found in neutral conditions using both schemes, followed by near neutral stable, stable and then unstable conditions, with number of time steps in stable conditions being the smallest. However, the mean wake lengths under stable conditions are not found to be the longest due to the presence of a significant number of low wind speeds, which result in shorter wakes, and the mean of these shorter wakes with some long wakes is lowered. Majority of neutral and near neutral stable conditions are in the direction of cross-flow, with a distribution including higher wind speeds, which results in longer wakes.

The total power losses due to the interaction of wind farm wakes over all five days of 10-minute time steps adds up to 3093.96 MW or 515.66 MWh as seen in the Fitch scheme, and 978.94 MW or 163.16 MWh in the EWP scheme, since there are larger wind speed deficits in the Fitch scheme resulting in higher power losses due to wind farm wake interaction. The total power losses as a function of stability condition are

found to be the highest in near neutral stable and neutral conditions, and the lowest in unstable conditions, though unstable conditions occur most frequently. This again, is due to the shorter wake lengths corresponding to the significant frequency of low wind speeds in stable conditions.

This is a shortcoming of the limited sample of modelled time steps, and does not directly imply that the modelled wakes, identified wake lengths and stability conditions, or calculated power losses are incorrect, though they have a certain associated uncertainty.

On comparing the WRF-EWP and WRF-Fitch modelled power against measurements for the specific case studies, it is found that due to significantly higher wind speed deficits observed at the hub height in the Fitch scheme, the power production values are almost always equal to or lower than the WRF-EWP modelled power. However, apart from the uncertainties from the modelling and methods of estimating parameters used, there is also an uncertainty in the power measurements.

The case study of the 9 day simulation also indicates that both, the EWP and Fitch scheme for these 9 days tend to:

- Over-predict the power under stable conditions, and therefore the Fitch scheme has lower errors due to lower modelled power compared to EWP scheme.
- Under-predict power under unstable conditions, and therefore the EWP scheme has lower errors due to higher modelled power compared to Fitch scheme.

This is easier to visualise by analysing Figure 5.44 and Table 5.10. There are various associated uncertainties that must be considered in such an analysis:

1. Fino3 measurements are influenced by the wind farms in certain wind flow directions.
2. Uncertainty in atmospheric stability classification.
3. Inherent uncertainties in the WRF model and the associated data used to run the model.
4. Uncertainties in wind turbine measurements.
5. Uncertainty from atmospheric stability being defined by one upstream point for each time step, instead of a spatial average.

Finally, due to the estimated larger occurrences of unstable conditions based on the Bulk Richardson number distribution at the Fino3, there is a possibility of the EWP scheme predicting the power values better. But this cannot be concluded from specific identified cases. Fino3 measurements are influenced by the wind farms in certain sectors, and a larger simulation period than 9 days is needed to generalise the behaviour of the two schemes in how they model the wakes and power for different stability conditions for the two offshore wind farms.

Chapter 7

Future Work

The project provides an understanding of the behaviour of the wind farm parametrisation schemes in WRF for the two wind farms. The results from the case studies indicate the possibility of the performance deviation of the schemes under stable conditions and unstable conditions.

The analysis of mean wake lengths belonging to each category of stability in Chapter 5.3 suggests that the two schemes and wake length calculation method used perform satisfactorily. The case studies indicate that wakes estimated from the the two schemes can affect flow from anywhere between 10 to nearly 100 km downstream under certain conditions.

Wind farms are normally not parametrised in operational NWP models, and to do so it requires details about the wind farms. Though, not only do the wakes have an impact on power production, but also on operational conditions and future wind resources of the surrounding areas. The wake interaction between WF1 and WF2 which are approximately 23 km apart, is observed to cause large power losses. Most of the newer wind farm clusters are separated by a distance much smaller than 23 km, suggesting the importance in understanding the behaviour of offshore wind farm wakes as seen in mesoscale models.

However, the evaluation also highlights the need for further investigations using a larger sample of cases than a few days or weeks. A much longer simulation period is needed to go from an understanding of the behaviour of the schemes and modelled wakes based on case studies, to understanding the general effect of stability on offshore wind farm wakes and wake interaction between WF1 and WF2. A longer simulation period would also provide enough data to classify wake lengths as functions of corresponding stability conditions, wind speed bins, and wind directions.

Beyond wake lengths and power as a function of stability, it would also be of value to evaluate the modelled wind speeds across the wind farms against nacelle measured wind speeds for the two wind farm parametrisation schemes. Since real-case modelled wind speeds using the two schemes have not been evaluated over distances around 23 km, this would aid in explaining the large difference in modelled power values between the EWP and Fitch scheme.

Therefore, understanding the behaviour of the two schemes in WRF under the different stability conditions, and the simulated wakes and power, have a direct impact on current and future wind resources, and operational forecasting for reasons such as O&M services, power forecasting, energy trading, and structural loading.

Appendix A

Wind Speed, Wake and TKE field for Cases 4 and 5

A.1 EWP scheme

A.1.1 Case 4

Presented in Figures A.1 and A.2, are the horizontal wind speeds at 90 m when the wind farms are parametrised, and horizontal wind speed difference at 90 m with and without the wind farms for case 4 (2018-04-24 17:20) respectively.

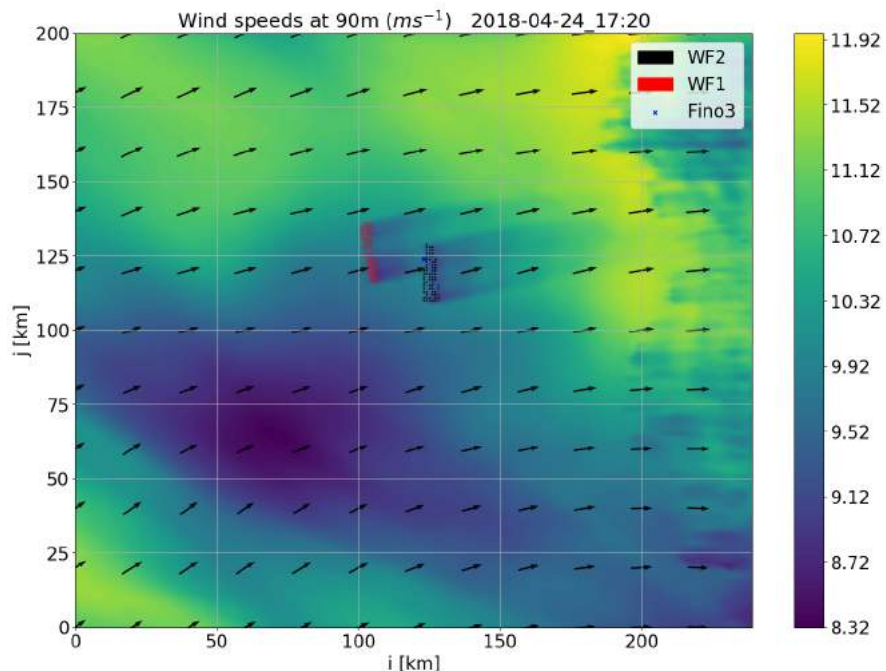


Figure A.1: Case 4 (2018-04-24 17:20) : WRF-EWP modelled wind speeds at 90 m with wind farms.

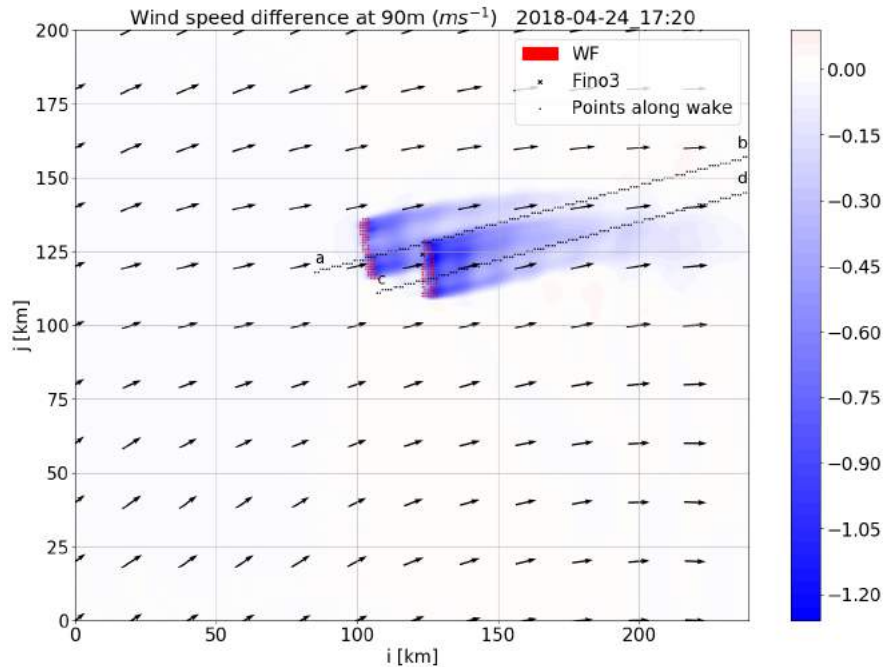


Figure A.2: Case 4: WRF-EWP modelled wind speed difference at 90 m
- with and without wind farms.

Figure A.1 shows the horizontal wind speed field at 90 m across the domain, and wakes are visible along the downstream direction from the wind farm.

Figure A.2 shows that the wind speed deficit region for WF2 (right wind farm) extends until the boundary of the domain, and there is a partial superposition of the wake from WF1 (left wind farm) and the wake from WF2. Small parcels of increased wind speeds of very small magnitude outside the wake region are also present some distance downstream of the wind farms.

Figure A.3 presents for Case 4 the vertical profile of wind speed difference with and without wind farms, along the points identified in the wake region for WF1 (a) and WF2 (b).

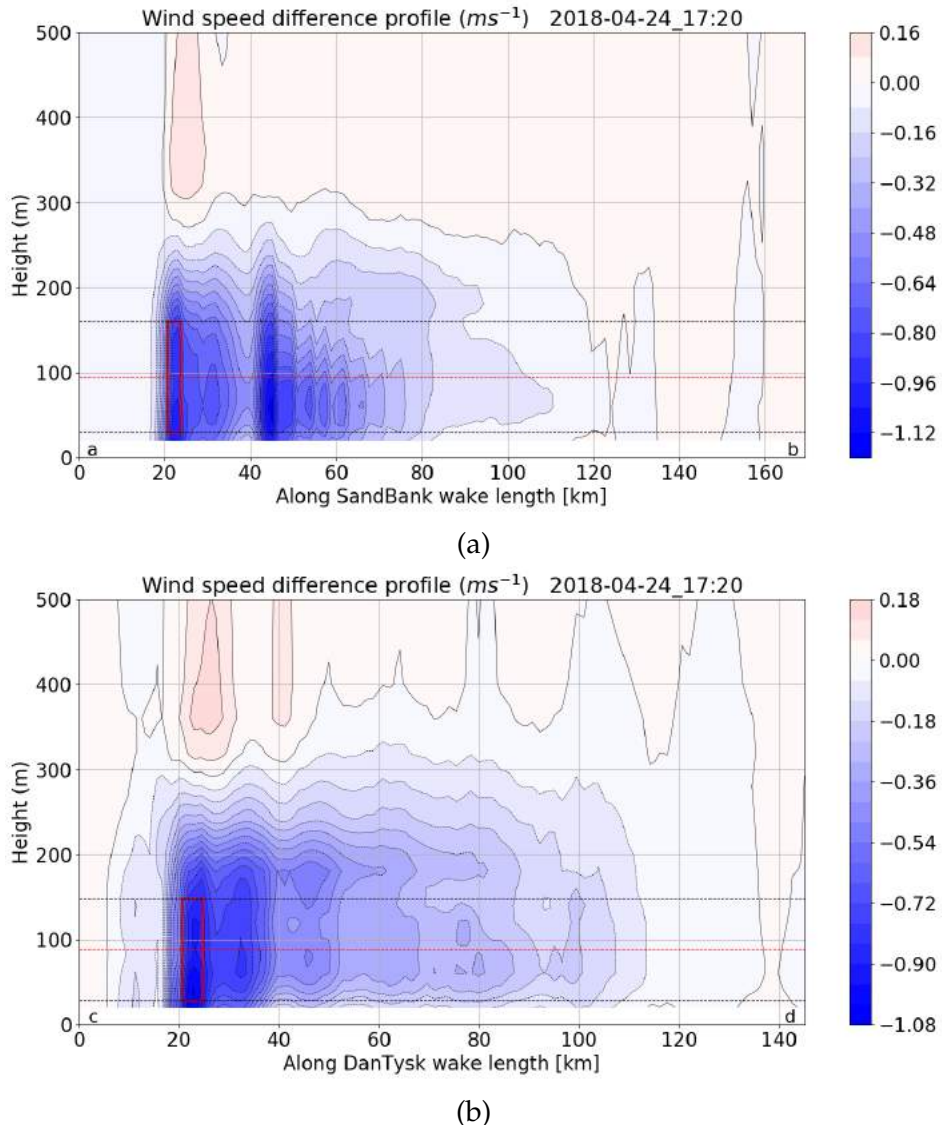


Figure A.3: Case 4: Profile of WRF-EWP modelled wind speed difference with and without wind farms along wake length points of WF1 (a) and WF2 (b).

It can be seen, that the wind speed deficit is highest in the region just downstream of the turbine rotors.

The wind speed difference along the hub height of WF1 (a) extends up to approximately 60-85 km downstream, and in the vertical to around 300 m for the first 60 km. The superposition of wakes from WF1 and WF2 is visible here, as a region of high velocity deficit is present some distance downstream of the indicated position of WF1. At heights above 300 m above the wind farm, an increase in wind speed is observed for both WF1 and WF2 (b). The wind speed difference along WF2 extends up to an average vertical height of 300 m along the wake length for about 70-90 km.

Similarly, Figure A.4 presents for Case 4 the vertical profile of TKE difference with and without wind farms, along the wake length for WF1 (a) and WF2 (b).

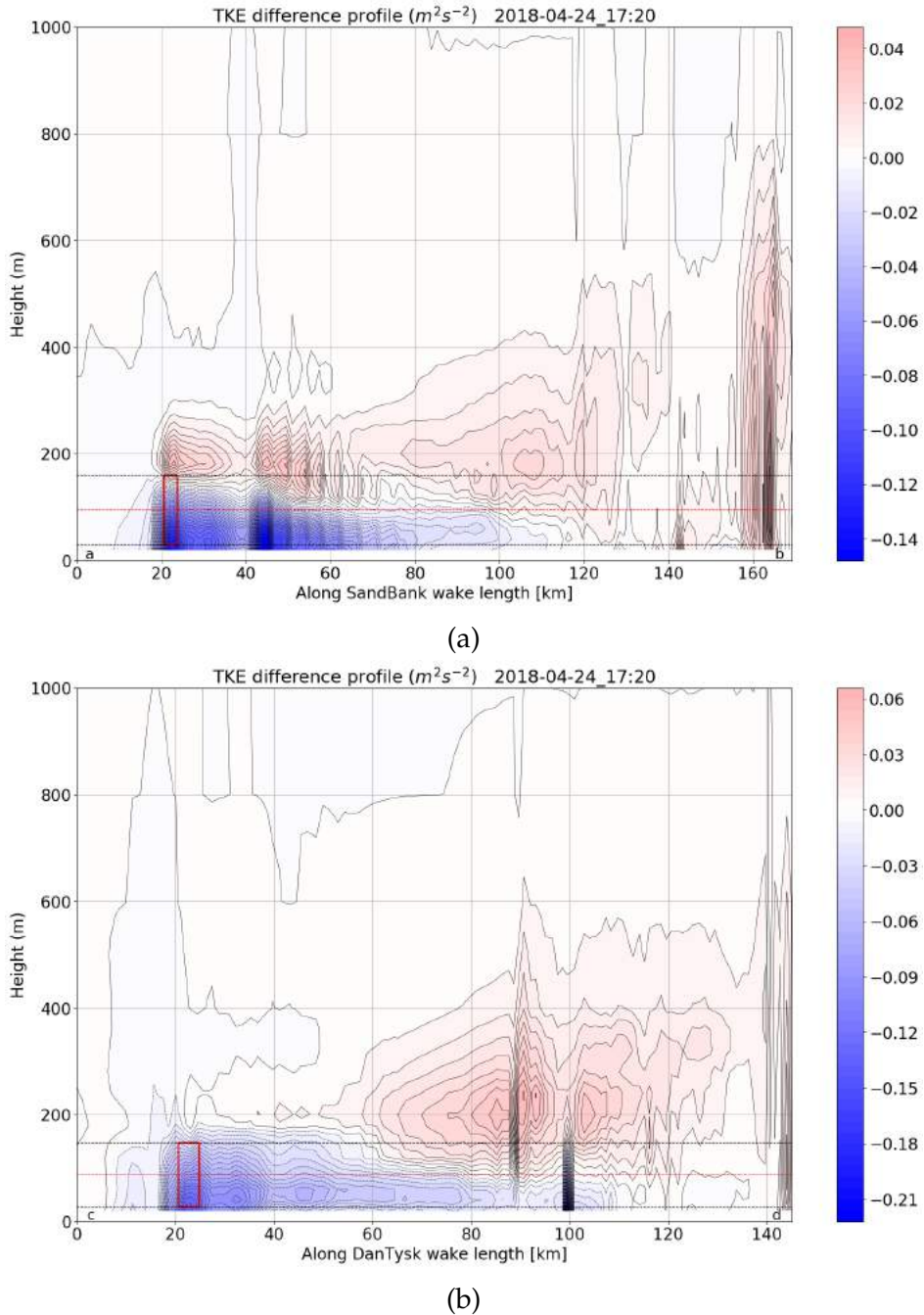


Figure A.4: Case 4: Profile of WRF-EWP modelled TKE difference with and without wind farms along wake length points of WF1 (a) and WF2 (b).

It can be seen, that there is a decreased TKE within the wind farm rotor region which extend to different distances downstream for both wind farm, and an increased TKE observed above the wind farms, with a smaller magnitude in the case of WF2 (b). However, far downstream of WF2, the increase in TKE above the rotor and hub height is larger than the magnitude of increase in WF1 (a). Due to the superimposed flow from WF1 to WF2, the TKE along WF1 (a) shows a region of decreased TKE some distance downstream of the indicated position of WF1, which indicates

the TKE introduced by WF2 in the flow field of WF1 if isolated. In both cases, the horizontal extent of this decreased TKE is approximately 80 km.

A.1.2 Case 5

Presented in Figures A.5 and A.6, are the horizontal wind speeds at 90 m when the wind farms are parametrised, and horizontal wind speed difference at 90 m with and without the wind farms for case 5 (2018-04-27 05:40) respectively.

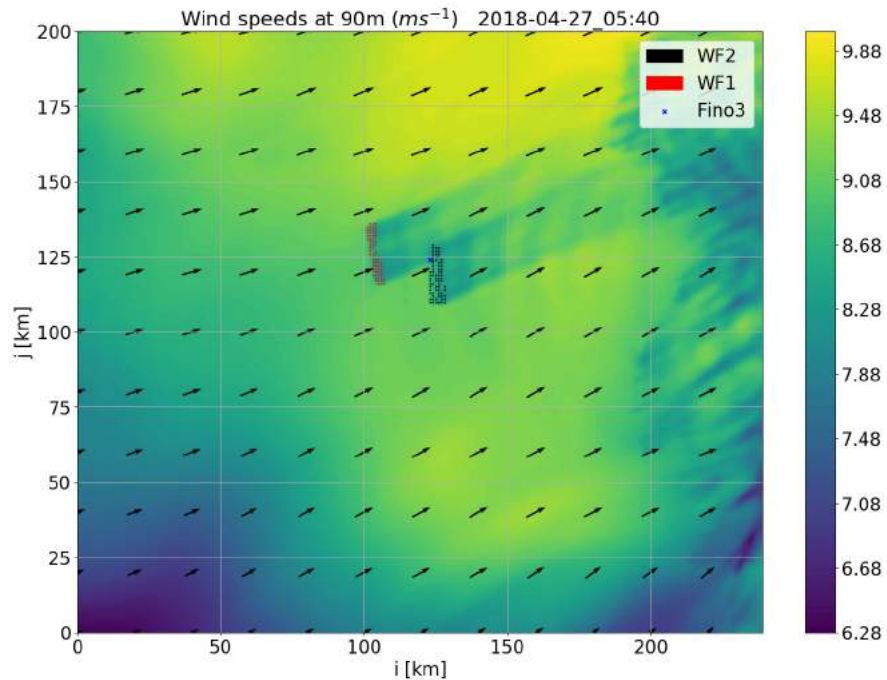


Figure A.5: Case 5 (2018-04-27 05:40) : WRF-EWP modelled wind speeds at 90 m with wind farms.

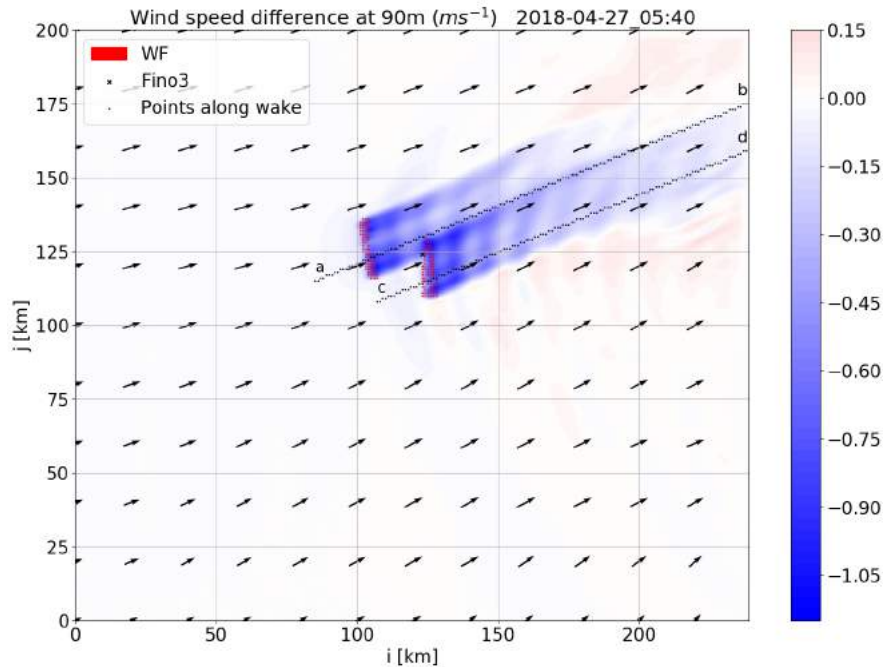


Figure A.6: Case 5: WRF-EWP modelled wind speed difference at 90 m
- with and without wind farms.

Figure A.5 shows the horizontal wind speed field at 90 m across the domain, and wakes are visible along the downstream direction from the wind farm.

It can be seen in Figure A.6, that the wind speed deficit region for WF2 (right wind farm) extend until the boundary of the domain, and there is a partial superposition of the wake from WF1 (left wind farm) and the wake from WF2. Though there is superimposed flow between WF1 and WF2, it is likely to not show up in the wind speed difference and TKE difference profiles along wake length. This is because the analysis points of WF1 lie outside this superimposed flow region as seen in Figure A.6. Areas of increased wind speeds outside the wake region are also present surrounding the downstream flow. Gravity waves are visible, which indicate very stable atmospheric conditions.

Figure A.7 presents for Case 5 the vertical profile of wind speed difference with and without wind farms, along the points identified in the wake region for WF1 (a) and WF2 (b).

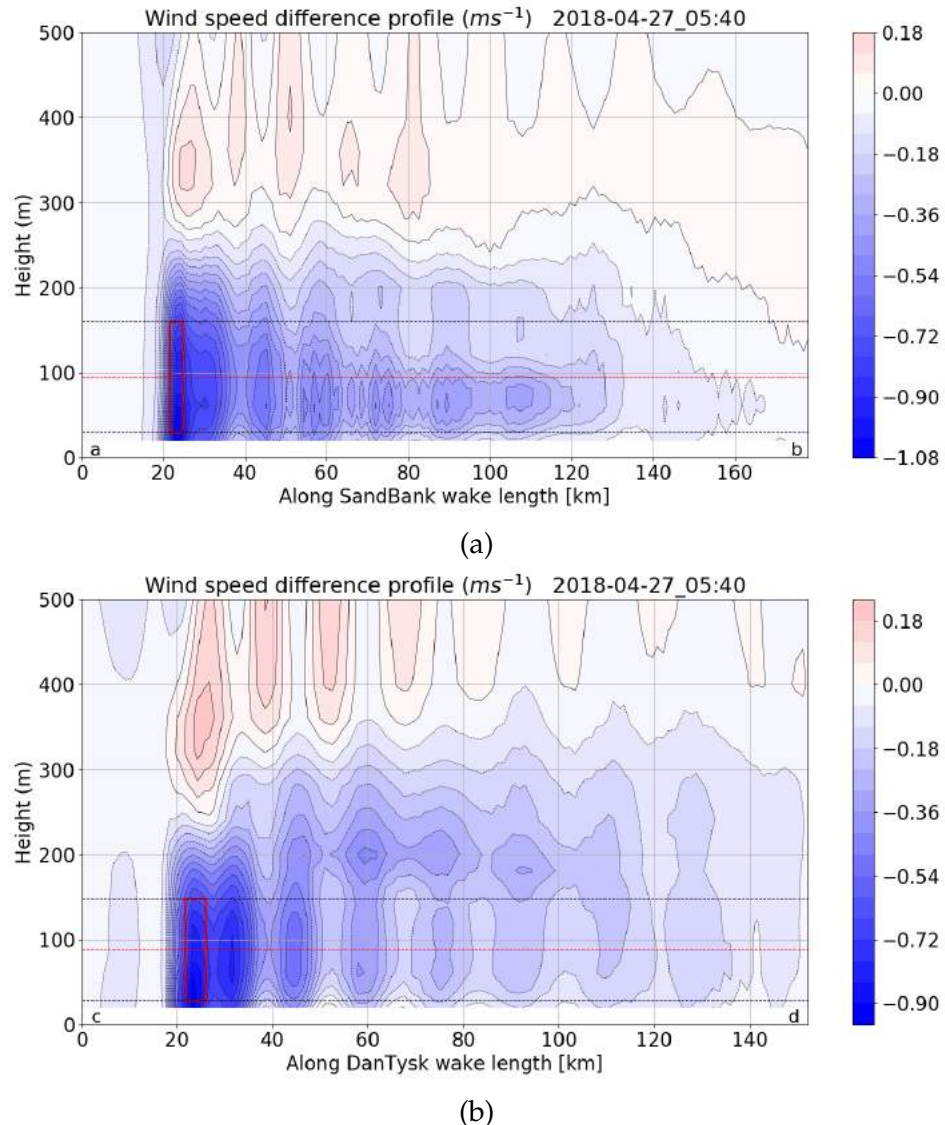


Figure A.7: Case 5: Profile of WRF-EWP modelled wind speed difference with and without wind farms along wake length points of WF1 (a) and WF2 (b).

It can be seen, that the wind speed deficit is highest in the region of and just downstream of the turbine rotors, with a higher wind speed deficit observed along the WF1 profile (a) than along WF2 (b) as WF1 is the upstream wind farm in this case.

In both cases, the wind speed deficit along the wind farm wake lengths extend up to the domain boundary. However, due to the presence of gravity waves, there are alternating parcels or vertical columns of larger and smaller magnitudes of wind speed deficit. This is also observed at heights above 300 m, where alternating parcels or vertical columns of increased and decreased wind speeds are visible, with more clarity in the WF2 profile (b).

Similarly, Figure A.8 presents for Case 5 the vertical profile of TKE difference with and without wind farms, along the wake length for WF1 (a) and WF2 (b).

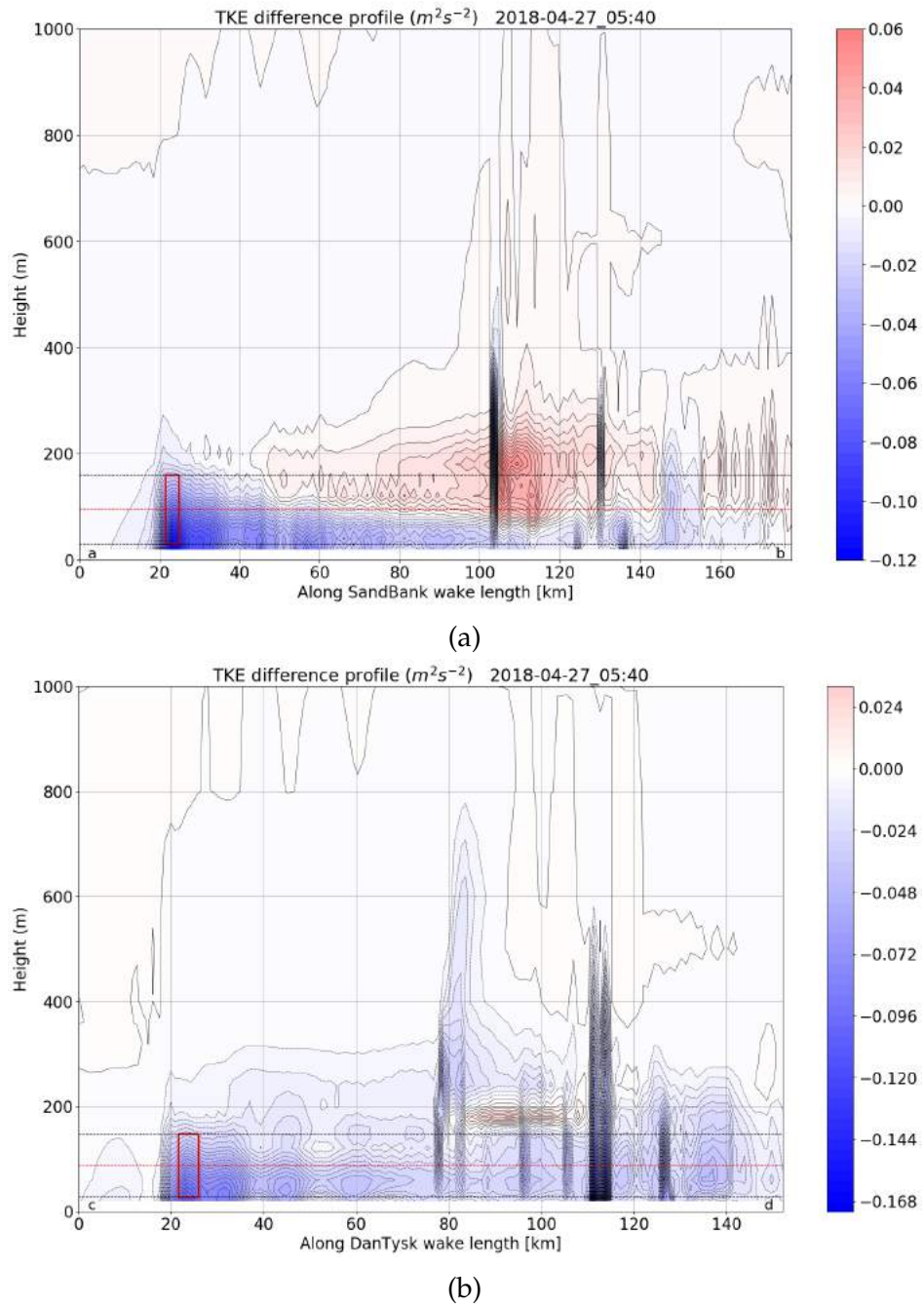


Figure A.8: Case 5: Profile of WRF-EWP modelled TKE difference with and without wind farms along wake length points of WF1 (a) and WF2 (b).

It can be seen, that there is a decreased TKE within the wind farm rotor region which extend to different distances downstream for both wind farm, without any increased TKE observed above the wind farms. However, a certain distance downstream of WF1 (a), the increase in TKE above the hub height is visible. This can be attributed to very stable conditions, due to which TKE is suppressed due to lack of convective motion in the atmosphere.

A.2 Fitch scheme

A.2.1 Case 4

Presented in Figures A.9 and A.10, are the horizontal wind speeds at 90 m when the wind farms are parametrised, and horizontal wind speed difference at 90 m with and without the wind farms for case 4 (2018-04-24 17:20) respectively.

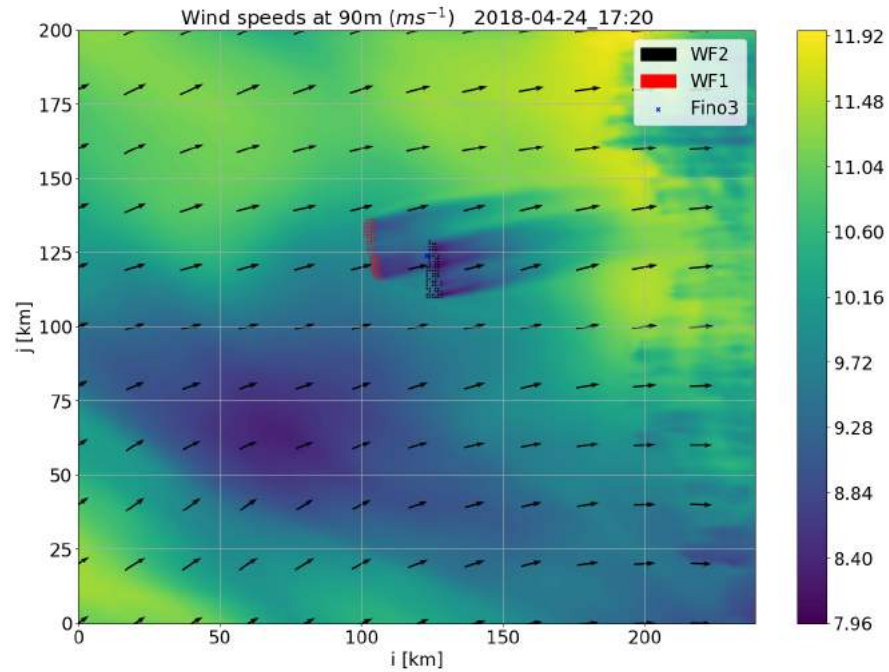


Figure A.9: Case 4 (2018-04-24 17:20) : WRF-Fitch modelled wind speeds at 90 m with wind farms.

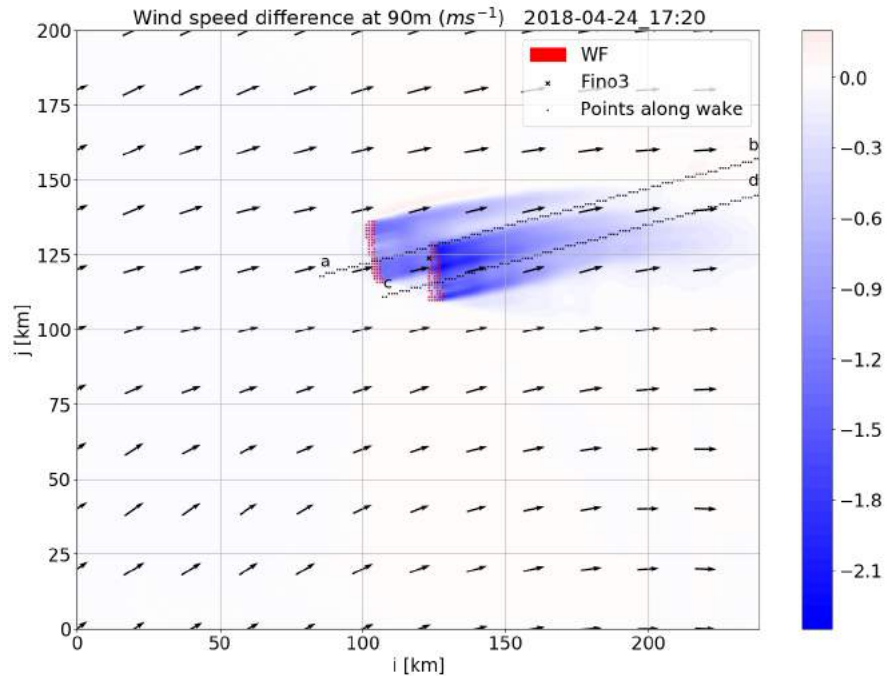


Figure A.10: Case 4: WRF-Fitch modelled wind speeds difference at 90 m - with and without wind farms.

The wind speed field and wake field in Figures A.9 and A.10 for case 4 with the WRF-Fitch scheme respectively, show almost no differences when compared to the simulations from WRF-EWP, with differences only in the wind speed values in the wind speed field and wake field.

Figure A.11 presents for Case 4 the vertical profile of wind speed difference with and without wind farms, along the points identified in the wake region for WF1 (a) and WF2 (b).

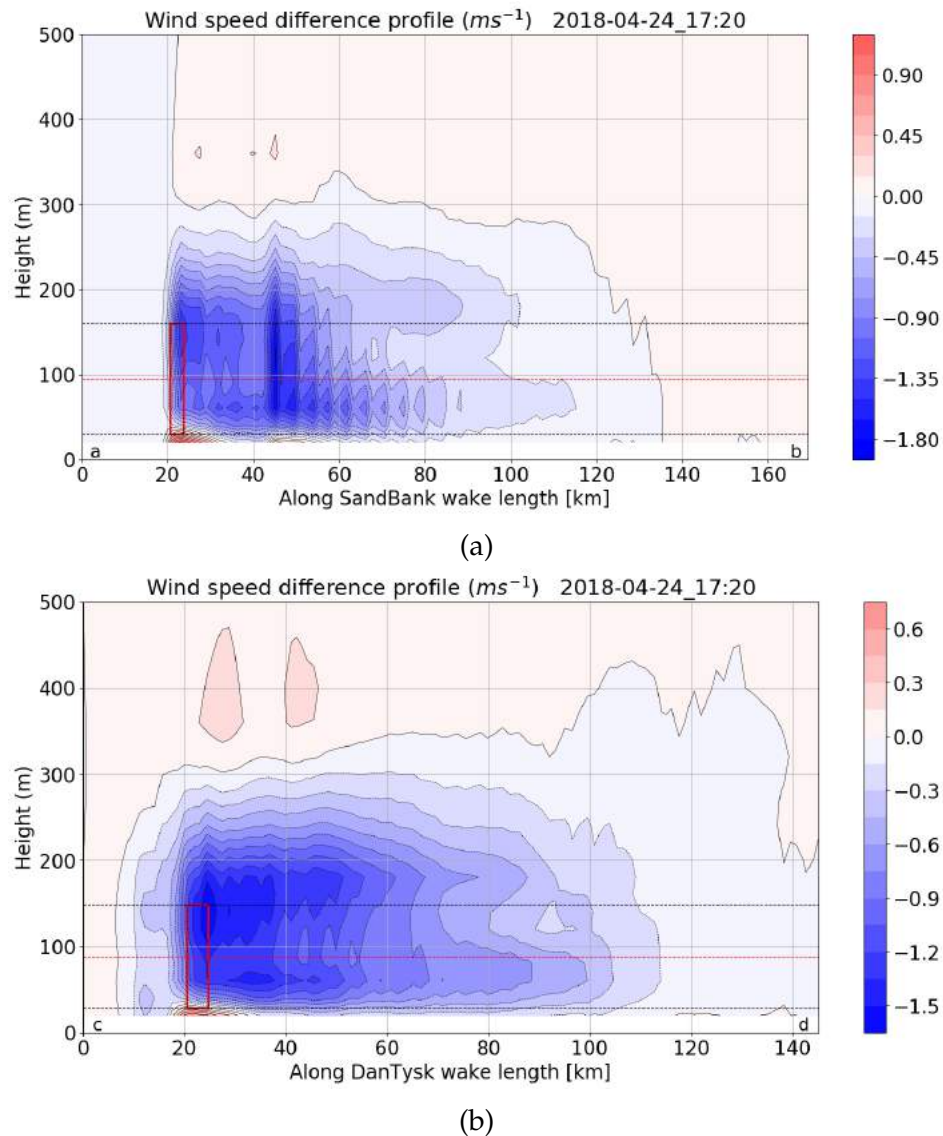


Figure A.11: Case 4: Profile of WRF-Fitch modelled wind speed difference with and without wind farms along wake length points of WF1 (a) and WF2 (b).

It can be seen again, that the wind speed deficit patterns are very similar to those observed in the WRF-EWP simulations. Differences being that the WRF-Fitch scheme results in the maximum wind speed deficit being larger in magnitude and closer to the upper portion of the wind farm rotor area, which is not the case in the WRF-EWP simulation. As in Case 1 and Case 2 from WRF-Fitch simulations, there is an increased wind speed below the rotor blades area. The extent in the downstream flow to which these wind speed deficits propagate are also very similar to what is observed using the WRF-EWP scheme. The superimposed flows are also visible here with the wind speed deficit downstream of WF1 (a) indicating the influence of WF2.

Similarly, Figure A.12 presents for Case 4 the vertical profile of TKE difference with and without wind farms, along the wake length for WF1 (a) and WF2 (b).

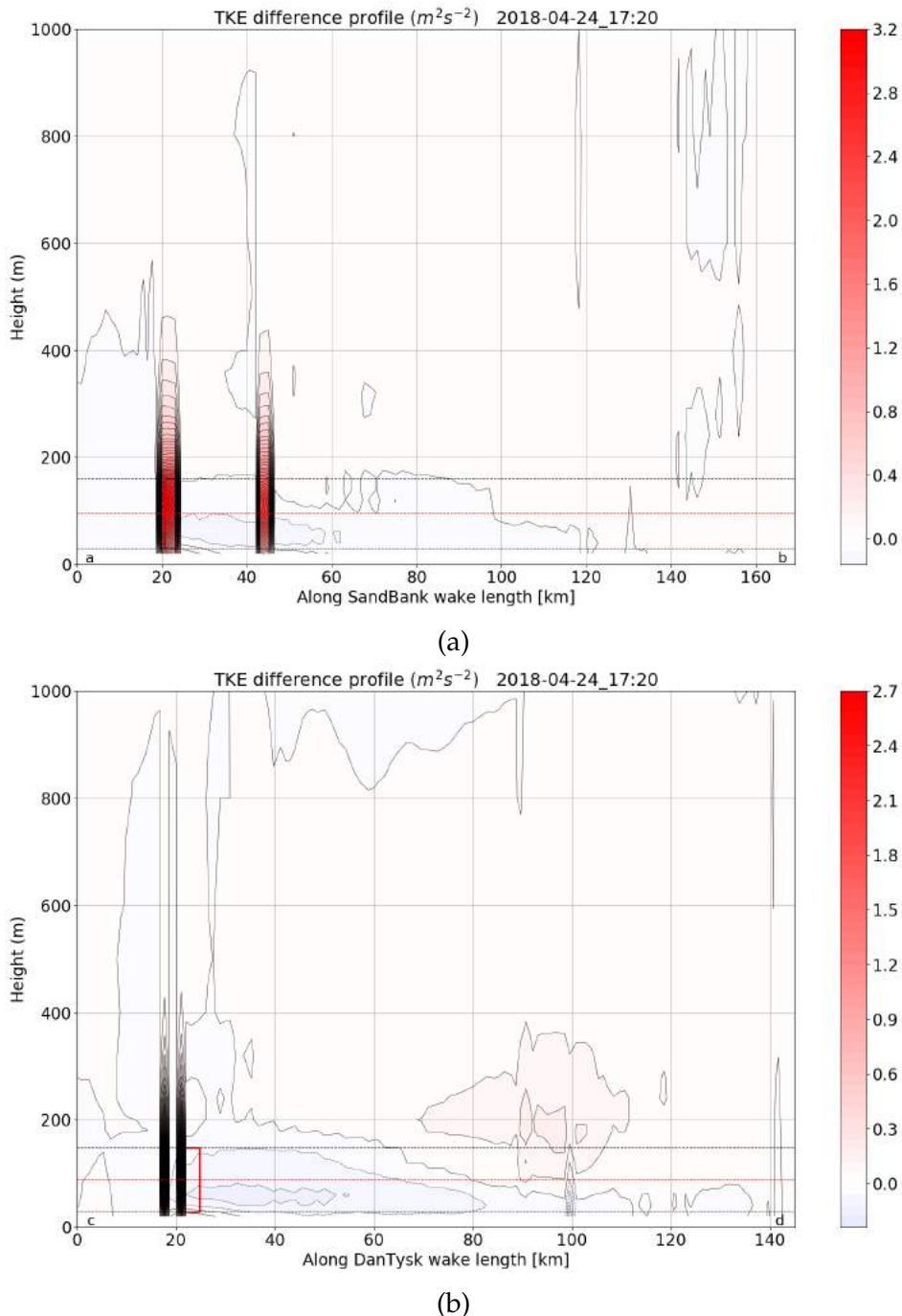


Figure A.12: Case 4: Profile of WRF-Fitch modelled TKE difference with and without wind farms along wake length points of WF1 (a) and WF2 (b).

It can be seen, in this case too there is a large increase in the TKE restricted to around the wind farm rotor area for both wind farms, with a decreasing magnitude in the vertical. Here too, the magnitude of increase in TKE in and around the wind farm rotor region masks the minor TKE downstream. The superimposed flows are also visible here with the increased TKE downstream of WF1 (a) indicating the influence of WF2.

A.2.2 Case 5

Presented in Figures A.13 and A.14, are the horizontal wind speeds at 90 m when the wind farms are parametrised, and horizontal wind speed difference at 90 m with and without the wind farms for case 5 (2018-04-27 05:40) respectively.

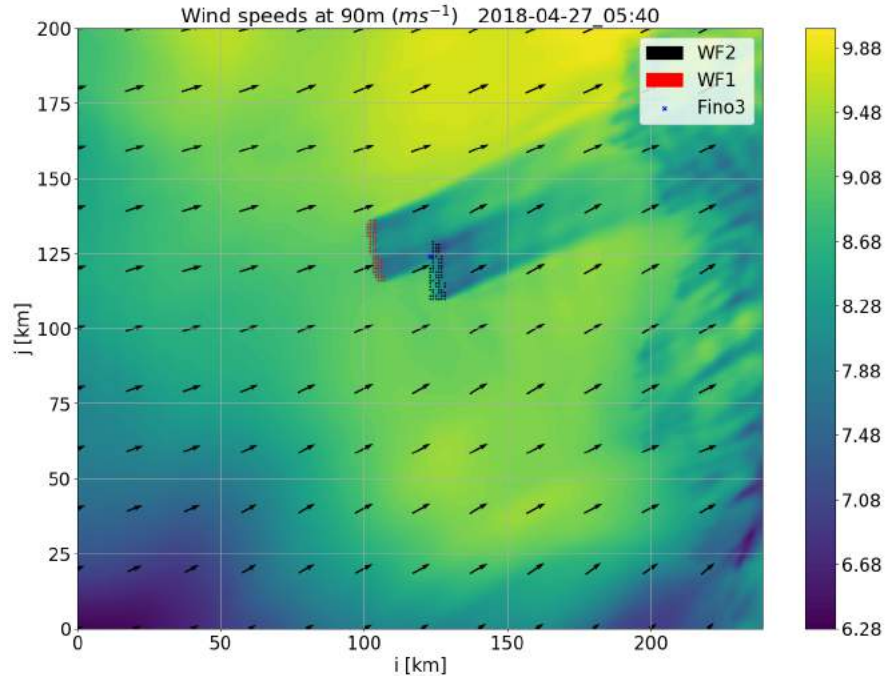


Figure A.13: Case 5 (2018-04-27 05:40) : WRF-Fitch modelled wind speeds at 90 m with wind farms.

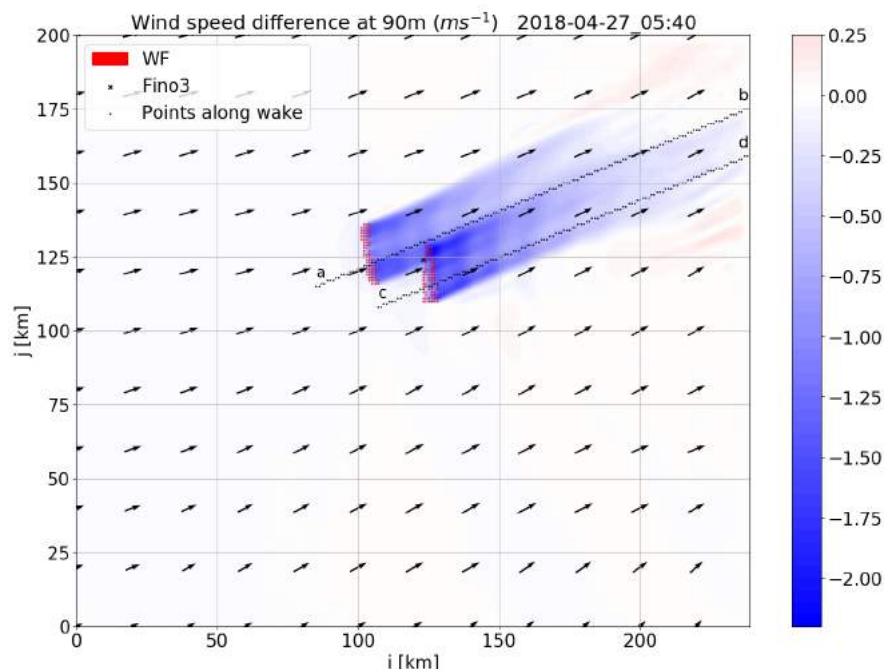


Figure A.14: Case 5: WRF-Fitch modelled wind speed difference at 90 m - with and without wind farms.

Figure A.13 shows the horizontal wind speed field at 90 m across the domain, and wakes are visible along the downstream direction from the wind farm.

The wind speed field and wake field in Figures A.13 and A.14 for Case 5 with the WRF-Fitch scheme respectively, are very similar when compared to the simulations from WRF-EWP. Differences in the values of wind speed deficits are quite large though. In the WRF-EWP scheme the maximum wind speed deficit is around -1.10 ms^{-1} , and nearly double this value in the WRF-Fitch simulation. One major difference however is the absence of gravity waves in this WRF-Fitch simulation result, which are present in the WRF-EWP simulation as seen in Figure A.6 in Chapter 5.2.1.

Figure A.15 presents for Case 5 the vertical profile of wind speed difference with and without wind farms, along the points identified in the wake region for WF1 (a) and WF2 (b).

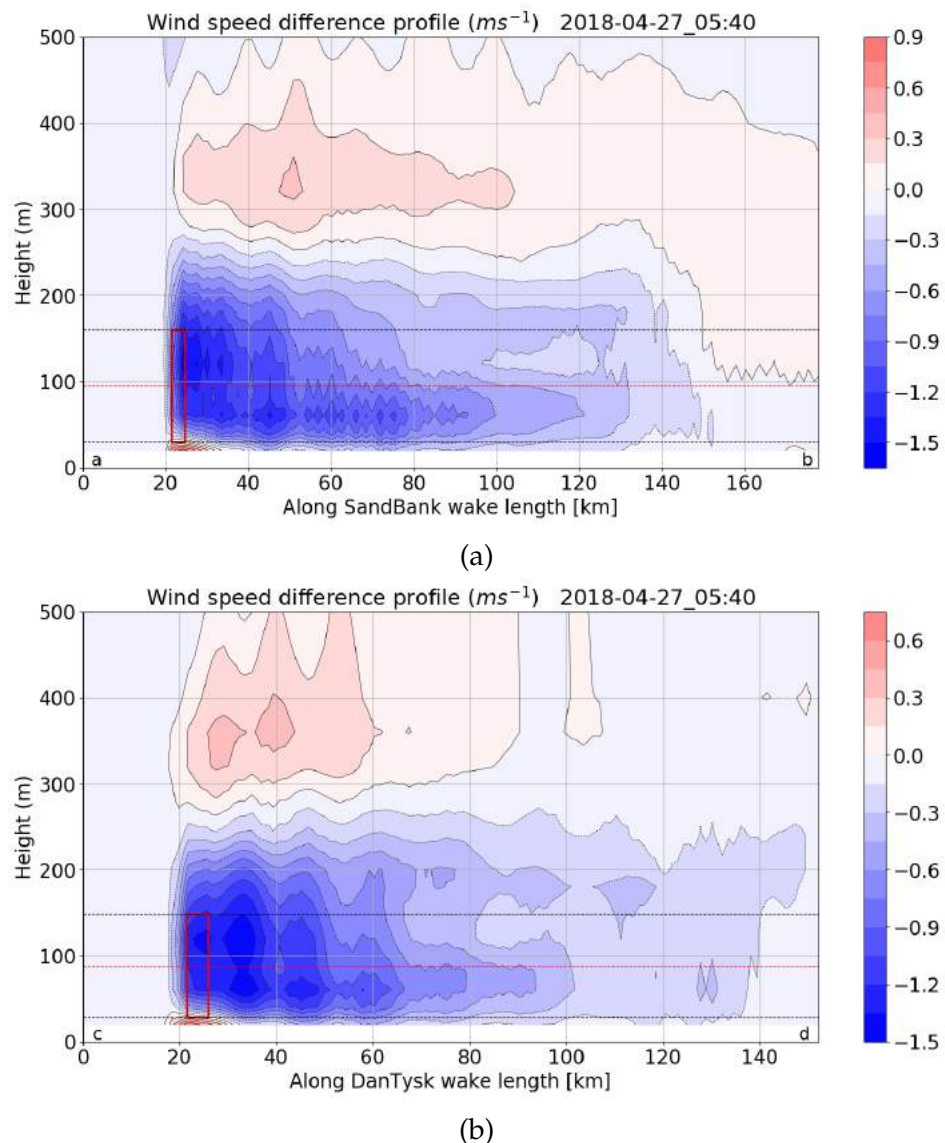


Figure A.15: Case 5: Profile of WRF-Fitch modelled wind speed difference with and without wind farms along wake length points of WF1 (a) and WF2 (b).

It can be seen, that the wind speed deficit is high in the region of or just downstream of the turbine rotors, with an increased wind speed below the rotor blades area for both WF1 (a) and WF2 (b). The extent of these wind speed deficit regions is similar to those observed in the WRF-EWP simulations, however the alternating wave-like patterns of increasing and decreasing wind speed differences as seen in the WRF-EWP simulations is absent in this WRF-Fitch simulation. This confirms the absence of gravity wakes in this simulation.

Similarly, Figure A.16 presents for Case 5 the vertical profile of TKE difference with and without wind farms, along the wake length for WF1 (a) and WF2 (b).

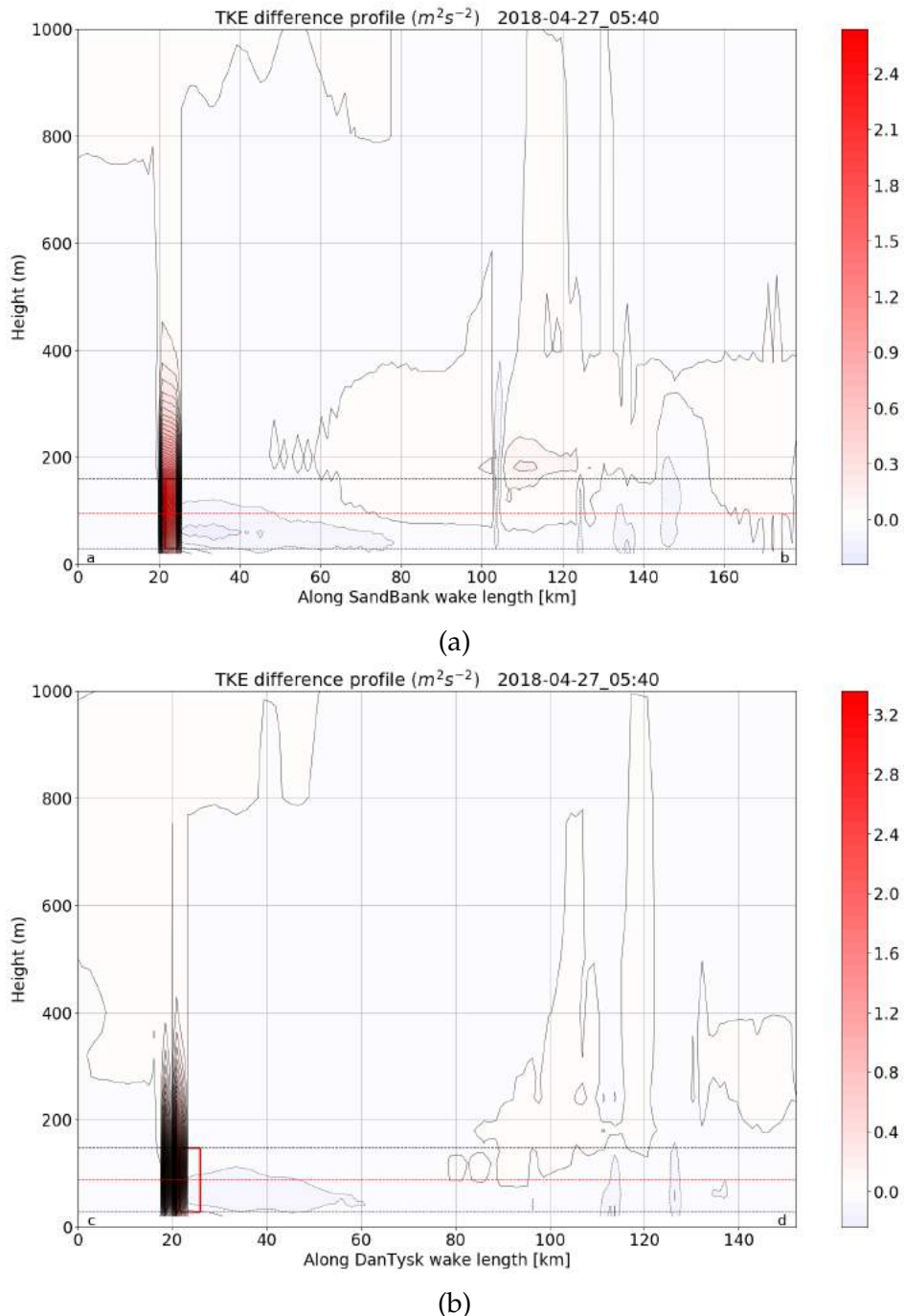


Figure A.16: Case 5: Profile of WRF-Fitch modelled TKE difference with and without wind farms along wake length points of WF1 (a) and WF2 (b).

It can be seen, in this case too there is a large increase in the TKE restricted to around the wind farm rotor area for both wind farms, with a decreasing magnitude in the vertical to a height of up to 400 m. In this case too, the magnitude of increase in TKE in and around the wind farm rotor region masks the minor TKE downstream.

Appendix B

Spatial Distribution of Temperature Difference

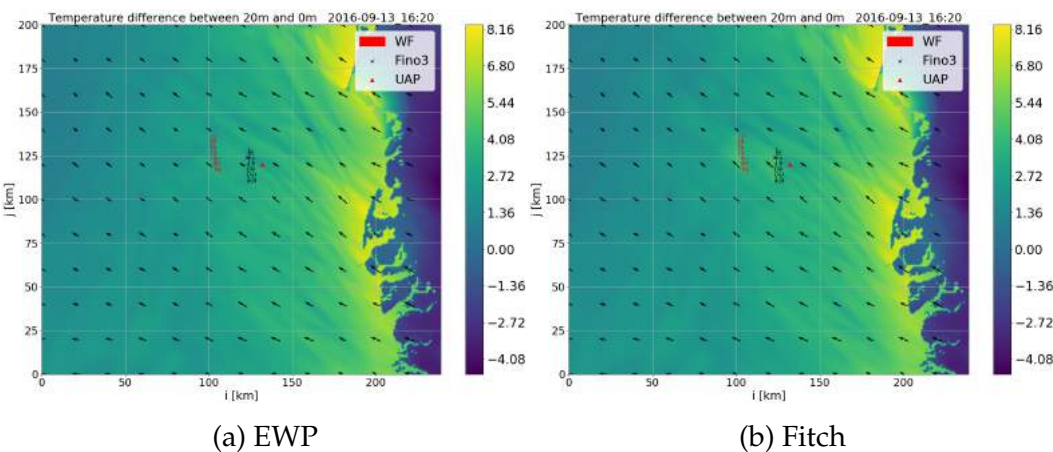


Figure B.1: Case 1 (2016-09-13 16:20): Temperature difference between 20 m height and sea surface.

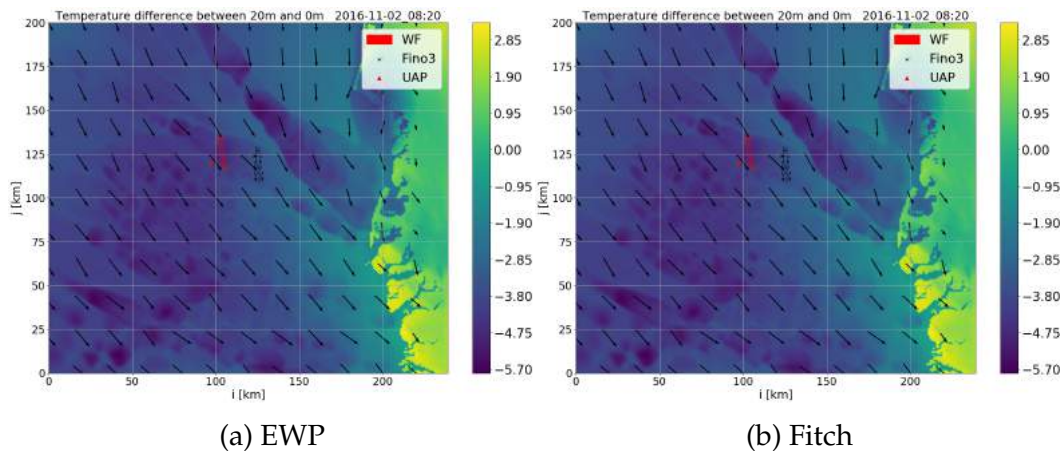


Figure B.2: Case 2 (2016-11-02 08:20): Temperature difference between 20 m height and sea surface.

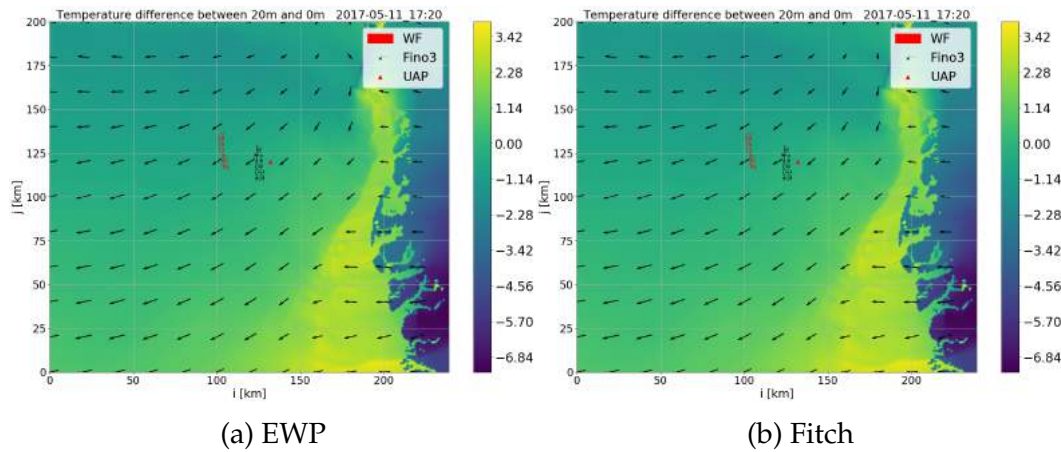


Figure B.3: Case 3 (2017-05-11 17:20): Temperature difference between 20 m height and sea surface.

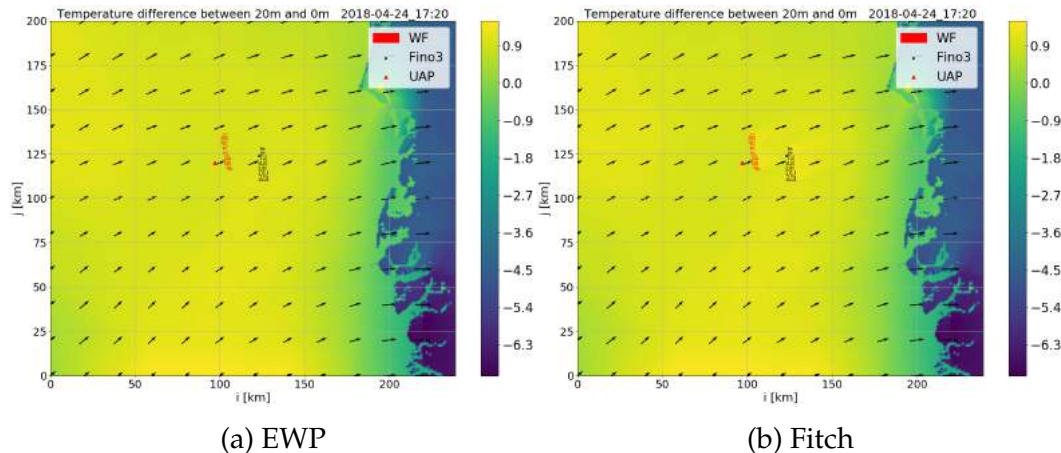


Figure B.4: Case 4 (2018-04-24 17:20): Temperature difference between 20 m height and sea surface.

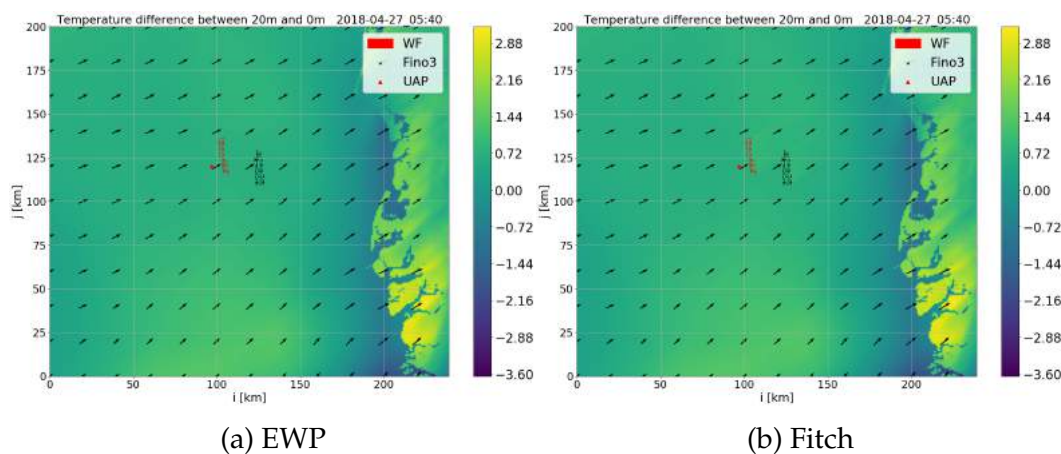


Figure B.5: Case 5 (2018-04-27 05:40): Temperature difference between 20 m height and sea surface.

References

- [1] Steve Sawyer, and Morten Dyrholm. *Global Wind Report - Annual Market Update 2017*. Global Wind Energy Council (GWEC), 2018.
- [2] Wind Europe work group. *Wind in power 2017*. Wind Europe, 2018.
- [3] Steve Sawyer, Sven Teske, and Morten Dyrholm. *The Global Wind Energy Outlook*. Global Wind Energy Council (GWEC), 2016.
- [4] Tuhfe Göçmen, Paul van der Laan, Pierre-Elouan Réthoré, Alfredo Peña Diaz, Gunner Chr. Larsen, and Søren Ott. "Wind turbine wake models developed at the technical university of Denmark: A review". In: *Renewable and Sustainable Energy Reviews* **60** (2016), pp. 752–769. URL: [doi:10.1016/j.rser.2016.01.113](https://doi.org/10.1016/j.rser.2016.01.113).
- [5] Alfredo Peña, Kurt Schaldemose Hansen, Søren Ott, and Maarten Paul van der Laan. "On wake modeling, wind-farm gradients, and AEP predictions at the Anholt wind farm". In: *Wind Energy Science* **3** (2018), pp. 191–202. URL: [doi:10.5194/wes-3-191-2018](https://doi.org/10.5194/wes-3-191-2018).
- [6] Barthelmie, R. J., Frandsen, S. T., Rathmann, O., Hansen, K. S., Politis, E., Prospathopoulos, J., Schepers, J.G., Rados, K., Cabezon, D., Schlez, W., Neubert, A., Heath, M. "Flow and wakes in large wind farms: Final report for UpWind WP8". In: *DTU Wind Energy Risoe-R, No.1765(EN)* (2011).
- [7] Baidya Roy, S., S. W. Pacala, and R. L. Walko. "Can large wind farms affect local meteorology?" In: *J. Geophys. Res.* **109** (2004), pp. 2156–2202. URL: [doi:10.1029/2004JD004763](https://doi.org/10.1029/2004JD004763).
- [8] Barrie, D. B., and Kirk-Davidoff, D. B. "Weather response to a large wind turbine array". In: *Atmos. Chem. Phys.* **10** (2010), pp. 769–775. URL: [doi:10.5194/acp-10-769-2010](https://doi.org/10.5194/acp-10-769-2010).
- [9] David W. Keith, Joseph F. DeCarolis, David C. Denkenberger, Donald H. Lenschow, Sergey L. Malyshev, Stephen Pacala, and Philip J. Rasch. "The influence of large-scale wind power on global climate". In: *Proc. Natl. Acad. Sci. USA* **101(46)** (2004), pp. 16115–16120. URL: [doi:10.1073/pnas.0406930101](https://doi.org/10.1073/pnas.0406930101).
- [10] Hasager, C. B., Rasmussen, L., Peña, A., Jensen, L. E., and Réthoré, P.-E. "Wind farm wake: the Horns Rev Photo Case". In: *Energies* **6** (2013), pp. 696–716. URL: [doi:10.3390/en6020696](https://doi.org/10.3390/en6020696).
- [11] P.J. H. Volker, J. Badger, A. N. Hahmann, and S. Ott. "The ExplicitWake Parametrisation V1.0: a wind farm parametrisation in the mesoscale model WRF". In: *Geosci. Model Dev.* **8** (2015), pp. 3715–3731. URL: [doi:10.5194/gmd-8-3715-2015](https://doi.org/10.5194/gmd-8-3715-2015).
- [12] Fitch, A. C., Lundquist, J. K., and Olson, J. B. "Mesoscale Influences of Wind Farms throughout a Diurnal Cycle". In: *Mon. Weather Rev.* **141** (2013), pp. 2173–2198. URL: [doi:10.1175/MWR-D-12-00185.1](https://doi.org/10.1175/MWR-D-12-00185.1).
- [13] Allaerts, D., Broucke, S.V., Lipzig, N.V., and Meyers, J. OR Dries Allaerts et al. "Annual impact of wind-farm gravity waves on the Belgian–Dutch offshore wind-farm cluster". In: *Journal of Physics: Conf. Series* **1037** (2018), p. 072006. URL: [doi:10.1088/1742-6596/1037/7/072006](https://doi.org/10.1088/1742-6596/1037/7/072006).

- [14] Allaerts, D., and Meyers, J. "Boundary-layer development and gravity waves in conventionally neutral wind farms". In: *J. Fluid Mech* **814** (2017), pp. 95–130. URL: [doi:10.1017/jfm.2017.11](https://doi.org/10.1017/jfm.2017.11).
- [15] Ollier, S.J., Watson, S.J., and Montavon, C. "Atmospheric gravity wave impacts on an offshore wind farm". In: *Journal of Physics: Conf. Series* **1037** 072050 (2018). URL: [doi%20:10.1088/1742-6596/1037/7/072050](https://doi.org/10.1088/1742-6596/1037/7/072050).
- [16] Merete B. Christiansen, and Charlotte B. Hasager. "Wake effects of large offshore wind farms identified from satellite SAR". In: *Remote Sensing of Environment* **98** (2005), pp. 251–268. URL: [doi:10.1016/j.rse.2005.07.009](https://doi.org/10.1016/j.rse.2005.07.009).
- [17] Charlotte Bay Hasager, Pauline Vincent, Jake Badger, Merete Badger, Alessandro Di Bella, Alfredo Peña , Romain Husson, and Patrick J. H. Volker. "Using Satellite SAR to Characterize the Wind Flow around Offshore Wind Farms". In: *Energies* **8** (2015), pp. 5413–5439. URL: [doi:10.3390/en8065413](https://doi.org/10.3390/en8065413).
- [18] Hasager, Charlotte Bay, Vincent, P., Husson, R., Mouche, Alexis, Badger, Merete, Pena Diaz, Alfredo, Volker, Patrick, Badger, Jake, Di Bella, Alessandro, Palomares, A., Cantero, E., and Correia, P.M.F. "Comparing satellite SAR and wind farm wake models". In: *Journal of Physics: Conference Series (Online)* **625** (2015), p. 0123035. URL: [doi:10.1088/1742-6596/625/1/0123035](https://doi.org/10.1088/1742-6596/625/1/0123035).
- [19] Jensen, N. O. *A note on wind generator interaction*. Tech. Rep. Risø-M No. 2411(EN). Risø National Laboratory: Roskilde, Denmark, 1983.
- [20] Nygaard, N.G. "First in situ evidence of wakes in the far field behind offshore wind farms". In: *Journal of Physics: Conference Series* **524**, 012162 (2014). URL: [doi:10.1088/1742-6596/524/1/012162](https://doi.org/10.1088/1742-6596/524/1/012162).
- [21] Mortensen, N.G.; Heathfield, D.N.; Myllerup, L.; Landberg, L.; Rathmann, O. *Getting Started with WAsP 9*. Tech. Rep. Risø-I-2571(EN). Risø National Laboratory: Roskilde, Denmark, 2018.
- [22] Abkar, M., and Agel, F.P. "The effect of atmospheric stability on wind-turbine wakes: A large-eddy simulation study". In: *Journal of Physics: Conference Series* **524** (2014), p. 012138. URL: [doi:10.1088/1742-6596/524/1/012138](https://doi.org/10.1088/1742-6596/524/1/012138).
- [23] Skamarock, W.C.; Klemp, J.B.; Dudhia, J.; Gill, D.O.; Barker, D.M.; Duda. M.; Huang, X.Y.; Wang, W.; Powers, J.G. *A Description of the Advanced Research WRF Version 3*. Tech. Rep. 2008. URL: [doi:10.5065/D68S4MVH](https://doi.org/10.5065/D68S4MVH).
- [24] Hahmann, Andrea N., Pena Diaz, Alfredo, and Hansen, Jens Carsten. "WRF Mesoscale Pre-Run for the Wind Atlas of Mexico". In: *DTU Wind Energy E* **0126** (2016). URL: [http://orbit.dtu.dk/en/publications/wrf-mesoscale-prerun-for-the-wind-atlas-of-mexico\(a7e97099-86bd-4c9e-9dbb-12cd2712ec1d\).html](http://orbit.dtu.dk/en/publications/wrf-mesoscale-prerun-for-the-wind-atlas-of-mexico(a7e97099-86bd-4c9e-9dbb-12cd2712ec1d).html).
- [25] Frandsen, Sten Tronæs; Chacón, L.; Crespo, A.; Enevoldsen, P.; Gómez-Elvira, R.; Hernández, J.; Højstrup, J.; Manuel, F.; Thomsen, K. "Measurements on and modelling of offshore wind farms". In: *Forskningscenter Risoe Risoe-R* **No. 903**(EN) (1996).
- [26] Hasager, C. B., Furevik, B.R., Pryor, S.C., Barthelmie, R.J. "Offshore wind resources quantified from satellite SAR: methodology and technical aspects". In: *Proceedings* (2002), pp. 778–782.
- [27] Hansen, Kurt Schaldemose; Barthelmie, Rebecca J.; Jensen, Leo E.; Sommer, Anders. "The impact of turbulence intensity and atmospheric stability on power deficits due to wind turbine wakes at Horns Rev wind farm". In: *Wind Energy* **15**(1) (2012), pp. 183–196. URL: [doi:10.1002/we.512](https://doi.org/10.1002/we.512).

- [28] Wagner, R., Courtney, M.S., Larsen T.J. *Simulation of shear and turbulence impact on wind turbine performance*. Tech. Rep. Risø-R-1722(EN). DTU Risø National Laboratory: Roskilde, Denmark, 2010.
- [29] Andreas Platis, Simon K. Siedersleben, Jens Bange, Astrid Lampert, Konrad Bärfuss, Rudolf Hankers, Beatriz Cañadillas, Richard Foreman, Johannes Schulz-Stellenfleth, Bughsin Djath, Thomas Neumann & Stefan Emeis. "First in situ evidence of wakes in the far field behind offshore wind farms". In: *Scientific Reports* **8:2163** (2018). URL: [doi:10.1038/s41598-018-20389-y](https://doi.org/10.1038/s41598-018-20389-y).
- [30] Hahmann, Andrea N., Pena Diaz, Alfredo, and Hansen, Jens Carsten. "Impact of atmospheric stability on X-band and C-band synthetic aperture radar imagery of offshore windpark wakes". In: *Journal of Renewable and Sustainable Energy* **10** (2018), p. 043301. URL: [doi:10.1063/1.5020437](https://doi.org/10.1063/1.5020437).
- [31] Lee, J.C.Y, and Lundquist, J.L. "Evaluation of the wind farm parameterization in the Weather Research and Forecasting model (version 3.8.1) with meteorological and turbine power data". In: *Geosci. Model Dev.* **10** (2017), pp. 4229–4244. URL: <https://doi.org/10.5194/gmd-10-4229-2017>.
- [32] J. K. Lundquist, K. K. DuVivier, D. Kaffine and J. M. Tomaszewski. "Costs and consequences of wind turbine wake effects arising from uncoordinated wind energy development". In: *Nature Energy* (2018). URL: <https://doi.org/10.1038/s41560-018-0281-2>.
- [33] Dagestad, K-F., Horstmann, J., Mouche, A., Perrie, W., Shen, H., Zhang, B., ... Vachon, P. "Wind retrieval from synthetic aperture radar - an overview." In: *Proceedings of SEASAR 2012 European Space Agency ESA - SP, No. 709* (2013).
- [34] Department of Wind Energy (DTU Wind Energy) Technical University of Denmark. *Wind fields from synthetic aperture radar*. 2007. URL: <https://satwinds.windenergy.dtu.dk/>.
- [35] Lard Landberg. *Meteorology for Wind Energy. An Introduction*. Wiley, 2016.
- [36] Barthelmie, R., and Jensen, L.E. "Evaluation of wind farm efficiency and wind turbine wakes at the Nysted offshore wind farm". In: *Wind Energy* **13** (2010), pp. 573–586. URL: [doi:10.1002/we.1632](https://doi.org/10.1002/we.1632).
- [37] Roy, S.B., and Traiteur, J.J. "Impacts of wind farms on surface air temperatures". In: *P. Natl. Acad. Sci. USA* **107** (2010), pp. 17899–17904. URL: <https://doi.org/10.1073/pnas.1000493107>.
- [38] Peña, A., and Hahmann, A.N. "Atmospheric stability and turbulence fluxes at Horns Rev—an intercomparison of sonic, bulk and WRF model data". In: *Wind Energy* **15** (2012), pp. 717–731. URL: [doi:10.1002/we.500](https://doi.org/10.1002/we.500).
- [39] Hsu, S.A. "The Relationship Between the Monin-Obukhov Stability Parameter and the Bulk Richardson Number at Sea". In: *Journal of Geophysical Research* **94** (1989), pp. 8053–8054. URL: <https://doi.org/10.1029/JC094iC06p08053>.
- [40] Larsén, X.G., Vincent, C., and Larsen, S. "Spectral structure of mesoscale winds over the water". In: *Q. J. R. Meteorol. Soc.* **139** (2013), pp. 685–700. URL: [doi:10.1002/qj.2003](https://doi.org/10.1002/qj.2003).
- [41] Fay, B., Schrodin, R., Jacobsen, I. and Engelbart, D. *Validation of mixing heights derived from the operational NWP models at the German Weather Service*. Tech. Rep. Risø-R-997 (EN). EURASAP Workshop Proceedings on the Determination of the H-Current Progress and Problems. (ed. S.E. Gryning), 1997, pp. 55–58.

- [42] Gryning, S.E., and Batchvarova, E. "Marine atmospheric boundary layer height estimated from NWP model output". In: *Int. J. Environ. Pollut.* **20** (2002), pp. 147–153. URL: [doi:10.1017/jfm.2017.11](https://doi.org/10.1017/jfm.2017.11).
- [43] Grachev, A.A., and Fairall, C.W. "Wake effects of large offshore wind farms identified from satellite SAR". In: *Journal of Applied Meteorology* **36(4)** (1997), pp. 406–415.
- [44] Pan, L.; Liu, Y.; Knievel, J.C.; Delle Monache, L.; Roux, G. "Evaluations of WRF Sensitivities in Surface Simulations with an Ensemble Prediction System". In: *Atmosphere* **9**, *106* (2018). URL: [doi:10.3390/atmos9030106](https://doi.org/10.3390/atmos9030106).
- [45] ARW Version 3 Modeling System User's Guide. Mesoscale & Microscale Meteorology Division, National Center for Atmospheric Research (NCAR), USA. January, 2017.
- [46] Larsén, X. G., Volker, P., Sørensen, P. E., Nissen, J., Du, J., Giebel, G., Hasager, C.B., Maule, P., Hahmann, A.N., Badger, J. *Large Scale Offshore Wake Impact on the Danish Power System (OffshoreWake)*. Abstract from EGU General Assembly: 2018, Vienna, Austria.
- [47] Vincent CL. *Mesoscale wind fluctuations over danish waters*. Risø-PhD; No 70(EN), PhD thesis. ISBN: 978-87-550-3864-6. 2010.
- [48] Larsén, X.G., Larsen, S.E., Petersen, E.L., Mikkelsen, T.K. "Turbulence Characteristics of Wind-Speed Fluctuations in the Presence of Open Cells: A Case Study". In: *Boundary-Layer Meteorology* (2019). URL: <https://doi.org/10.1007/s10546-019-00425-8>.